UNIVERSITY OF CALIFORNIA, SAN DIEGO

Development of an impedance method based wireless sensor node for monitoring of bolted joint preload

A thesis submitted in partial satisfaction of the
requirements for the degree Master of Science

in

Structural Engineering

by

David Dennis Lee Mascareñas

Committee in charge:

Professor Michael Todd, Chair
Professor Charles Farrar
Professor William Hodgkiss

2006

The thesis of David Dennis Lee Mascareñas is approved:

_____

_____

_____

Chair

University of California, San Diego

2006

Table of Contents

Signature Page……...iii

Table of Contents……...iv

List of Figures…….....viii

List of Tables……xi

Acknowledgements……...xii

Abstract……xiii

Chapter 1 Background and Literature Review 1

1.1 Introduction 1

1.2 Review of Bolted Joint Monitoring 2

1.3 Review of the Impedance Method 4

1.3.1 Overview 4

1.3.2 Piezoelectric materials 5

1.3.3 Impedance Method, Theory and operation 7

1.3.4 Applications 11

1.3.5 Drawbacks and current challenges 12

1.4 Review of Energy Considerations for wireless sensor nodes 15

1.4.1 Overview 15

1.4.2 Energy Harvesting 16

1.4.3 Low Power Circuit Design 19

1.4.4 RF Power Delivery 22

1.4.5 Sensor Network Paradigms 28
1.5 Review of SHM sensor node technology 30
Chapter 2 Piezoelectric (PZT) Enhanced Washer 32
2.1 Overview 32
2.2 Dynamic Behavior of PZT Enhanced Washers Under Varying Preload 35
2.2.1 Analytical Dynamic Behavior of the PZT enhanced washer 35
2.2.2 Isolation Washers 39
2.2.3 Experimental Setup and Results 41
2.2.4 Wafer-Based PZT enhanced washer 43
2.3 Generalized Baseline and Repeatability 45
2.4 Insensitivity to Host Dynamics 51
2.5 Effects of Bond Quality and its Characterization 53
2.6 Summary 58
Chapter 3 Impedance method-based wireless sensor node for SHM 60
3.1 Overview 60
3.2 AD5933 characteristics and operation 61
3.3 Comparison of Agilent 4294A Impedance Analyzer and AD5933 62
3.4 Sensor Node Layout and Components 65
3.4.1 Sensor node Layout and Operation 65
3.4.2 Microcontroller ATmega128L 68
3.4.3 Wireless Telemetry 70
3.4.4 Wireless Sensor Node Power Requirements 72

3.5 Experimental Results with the Sensor Node 74
3.5.1 PZT enhanced washer 76
3.5.2 Portal frame 83
3.5.3 Composite Wing Spar Assembly 89
3.6 Sensor Node Summary 94
Chapter 4 Wireless RF Power Delivery 96
4.1 Overview 96
4.2 RF power delivery components 98
4.2.1 RF power source 98
4.2.2 Horn Antennas 99
4.2.3 Rectification Circuit 101
4.2.4 Supercapacitors 102
4.3 Energy Transfer Performance 103
4.3.1 Analytical evaluation of energy transfer performance 103
4.3.2 Experimental Evaluation of RF power delivery performance 105
4.4 Summary of RF Wireless Power Delivery 110
Chapter 5 Conclusions and Future Work 112
5.1 Accomplishments 112
5.2 Contributions 113
5.3 Future Work 114
5.3.1 PZT Enhanced Washer 114
5.3.2 Wireless Sensor node 115

5.3.3 RF Wireless Power Delivery 116
5.4 Conclusions 117
Bibliography 119

List of Figures

Figure 1-1: Block diagram of the impedance method 7

Figure 2-1: Various forms of PZT enhanced washers 34

Figure 2-2: Ring actuator-type PZT enhanced washer in use 34

Figure 2-3: PZT enhanced nut in use 34

Figure 2-4: Bolted joint impedance dynamics 35

Figure 2-5: Analytical impedance magnitude progression. 38

Figure 2-6: Various isolation washers 39

Figure 2-7: PZT ring-type stack actuator 1000/25-15/5, real portion of impedance 42

Figure 2-8: PZT ring-type stack actuator 1000/25-15/25, real portion of impedance. 42

Figure 2-9: Aluminum-hex, PZT-enhanced washer 44

Figure 2-10: PZT aluminum-hex washer repeatability experiment 46

Figure 2-11: Repeatability between two PZT hex washers. 47

Figure 2-12: Cylindrical steel and aluminum PZT enhanced washers 48

Figure 2-13: Real portion of the impedance for the aluminum and steel washers 50

Figure 2-14: Real portion of the impedance measurements 53

Figure 2-15: Aluminum-hex PZT washer 54

Figure 2-16: Real portion of the impedance measurements. 55

Figure 2-17: Imaginary portion of admittance values. 57

Figure 3-1: Agilent 4294A impedance analyzer, $41K 62

Figure 3-2:, AD5933 development board, $150 63

Figure 3-3: Block diagram of proposed sensor node.....65

Figure 3-4: Prototype Impedance-based wireless sensor node.....68

Figure 3-5: ATmega128L microcontroller.....69

Figure 3-6: Xbee radio for wireless telemetry.....71

Figure 3-7: 25.4-mm, aluminum-hex PZT enhanced washer.....76

Figure 3-8: 25.4-mm aluminum hex PZT enhanced washer.....77

Figure 3-9: 19-mm, steel PZT enhanced washer.....79

Figure 3-10: AD5933 real register values.. 80

Figure 3-11: AD5933 real register minimum values.....81

Figure 3-12: Portal frame structure 84

Figure 3-13: Portal frame conductance measurements. 85

Figure 3-14: Composite wing spar assembly 90

Figure 3-15: Damage progression in composite wing spar assembly. 90

Figure 3-16: Agilent 4294A admittance measurements.....91

Figure 3-17: AD5933 admittance for the composite wing spar assembly. 91

Figure 3-18: Agilent 4294A admittance for the composite wing spar assembly 92

Figure 3-19: AD5933 admittance for the composite wing spar assembly 93

Figure 4-1: RF power delivery test setup 97

Figure 4-2: X-band source, 25 dB amplifier, and transmitter horn Antenna 100

Figure 4-3: Voltage 8X multiplier Circuit Schematic 101

Figure 4-4: 8X Voltage Rectifier.....102

Figure 4-5: Aerogel .1 F supercapacitor rated for 5V 103

Figure 4-6: Voltage and energy storage across .1 F supercapacitor 106

Figure 4-7: Discharge characteristics of the .1 F capacitor, during the range test. ... 109

Figure 4-8: Range test software summary of Xbee radio performance 110

List of Tables

Table 2-1: PZT stack parameter comparison……...41

Table 3-1: Impedance measurement solution comparison……...63

Table 3-2: Sensor node voltage and current requirements……...72

Table 3-3: Sensor node power requirements……72

Acknowledgements

There are a number of people I would like to thank that helped to make this thesis possible. First off I would like to thank Charles Farrar for inviting me to Los Alamos National Labs (LANL) in the summer of 2003 for the Dynamic Summer School. He has been nothing but supportive of my work since that time whether it meant writing letters of recommendation, providing research opportunities, or helping me find a place to go to graduate school. Next, Gyuhae Park who has been my mentor at Los Alamos both during the Dynamic Summer School at LANL and for the work that followed concerning the bolted joint preload monitoring problem. He has been a good friend and has introduced me to many aspects of the structural health monitoring field. I am also thankful to my advisor Mike Todd for bringing me into his research group at UCSD. He provided me with some interesting challenges, my most favorite of which was building a 20 ft high testing frame for fiber optic shape reconstruction research. William Hodgkiss also deserves recognition for serving on my committee and teaching an excellent digital signal processing sequence of classes. The GEM Consortium provided my fellowship and I am thankful for their financial support.

A number of different people at Los Alamos played a role in the completion of this research. First off, I am very grateful to Steve Ball from Motorola/Snurkle Engineering for willing to spend time discussing the fine points of embedded systems with me. Steve's unbridled enthusiasm for digital electronics picked up my day on more than one occasion and his advice was greatly appreciated. The RF power delivery experiments could not have been completed without the help of Roger Bract. Roger provided the X-band radar equipment and guidance on how I might implement the AC-DC conversion. Roger's passion for microwave radiation was greatly valued, and I hope to implement more of his suggestion in my future research. Kathie Womack and Debbie Colson deserve a special acknowledgement because they have always been very helpful whenever I needed to navigate the administrative aspects of doing research at Los Alamos. I am grateful for their help. If I ever needed to order equipment Debbie Carlisle always made time to ensure it arrived when it was needed. I want to thank John Sandoval for his quick response and good advice concerning electrical safety issues. I also want to acknowledge Alan Bramlett for always being available to set up computers as I needed them and providing support. Lastly I want to thank Kyle Nekimken for helping me perform testing and for his assistance building the prototype sensor nodes.

Most importantly I want to thank my family and friends. My parents David and Marie have always tried their best for me and have always listened to my problems. My brother Stephen also deserves recognition for his service with the Marines in Iraq during the time period of this research. I also want to thank my brothers and sisters John, Mary, Matthew and Christina. I am thankful for my roommate in Los Alamos, Warren Lybarger, who has also always been willing to listen to my troubles. A special acknowledgement must also go out to Ronald Terry for his help navigating the jungle of California. I wish him luck in his future endeavors.

ABSTRACT OF THE THESIS

Development of an impedance method based wireless sensor node for monitoring of bolted joint preload

by

David Dennis Lee Mascareñas

Master of Science in Structural Engineering

University of California, San Diego, 2006

Professor Michael D. Todd, Chair

The impedance method, based on detecting changes in the coupled electrical and mechanical impedance characteristics of a piezoelectric device bonded to a structure, has been studied extensively for a wide range of structural health monitoring applications. In this work a recently developed impedance measurement chip is incorporated into a prototype active sensor node designed for monitoring the preload of bolted joints. The sensor node also incorporates the recently developed

piezoelectric material-based PZT enhanced washer, a microcontroller, and wireless telemetry capabilities. It is shown that this low cost sensor node is capable of making near real-time evaluations of bolted joint preload. In addition, the integration of this wireless sensor node with rectenna (rectifying antenna) technology has been investigated in order to allow operation without a conventional power supply such as a battery. A rectenna is constructed from a pair of X band horn antennas, and microwave energy is wirelessly transported between horn antennas in order to charge an ultra-capacitor to the 3.3V necessary for typical complimentary metal-oxide semiconductor (CMOS) logic operation. It is demonstrated that the stored energy can successfully run the sensor node telemetry, which is by far the largest power consumer in the sensor node. By utilizing embedded computing methods, recently developed impedance measurement integrated circuits, and the PZT enhanced washer, this newly designed impedance sensing node is a major contribution toward practical implementation of the impedance method This node comprises an important component of a wireless sensor network that could be deployed on large-scale structures where self-monitoring of numerous bolted connections is of critical importance.

Chapter 1 Background and Literature Review

1.1 Introduction

Bolted joints are among the most prevalent forms of fastening used today. Many mission critical structures rely on a large number of bolted joint connections in order to ensure safe and reliable operation. Because of the widespread use of bolted joints, they are also often the subject of mechanical failures. Recently, Stork Materials Testing and Inspection carried out a survey on the faster failures they had investigated, and found that 77 percent of all failures were caused by fatigue, overload, hydrogen embrittlement and stress corrosion cracking (Menendez, 2003). Despite these common environmental and operational influences, there has been no technology driver for the automation of bolted joint preload monitoring until recently. The next generation naval destroyer is projected to make widespread use of structural hybrid composite bolted joints. On a conventional naval vessel, the maintenance crew would be responsible for ensuring the integrity of these bolted joint connections, but the plans for the destroyer also call for a 70% reduction in crew size (Nichols, 2004). A time based maintenance schedule is no longer practical because the navy wants to maximize the number of war fighters on the ship, and minimizes time and personnel resources spent on maintenance. A condition based monitoring approach must be adopted in order to realize the navy's goals.

This thesis presents an active-sensing wireless sensor node that can determine when a bolted joint connection has lost preload. The sensor node is based off the impedance method for Structural Health Monitoring (SHM). To date the impedance method has not been utilized outside a laboratory setting. This work takes advantage of a recently developed impedance measurement chip, as well as novel piezoceramic (PZT) based sensors, in order to build a wireless sensor node from off the self components, suitable for field deployment. In addition, this thesis investigates the use of rectenna (rectifying antenna) technology for wirelessly transferring microwave energy to the sensor node in order to allow operation independent of a conventional battery power supply.

1.2 Review of Bolted Joint Monitoring

It has been estimated that 70% of all mechanical failures are caused by fastener failures (Simmons, 1986). The pervasive nature of bolted joint connections has led to a number of studies into monitoring the integrity of bolted joint connections. Nichols (2003, 2004) utilized chaotic excitations and a phase space method to assess the condition of a bolted joint in a composite beam. Abe (2003) used PZT active sensors in conjunction with a bolted joint model for impedance-based bolted joint monitoring. Impedance measurements during service conditions were compared with the model at various levels of bolt preload. The measurements that best matched with a given preload level in the model were used to determine the preload level in the actual joint.

In addition, the impedance method has also been used to monitor bolted joints in civil pipeline structures by Park (2001). Yang (2003) used lamb wave propagation to bolt loosening in a space thermal protection panel. The attenuation of the lamb waves was used as an indicator of the amount of damping present in the panel joint as well as the current state of the joint. Okugawa (2004) proposed a new method of bolt-loosening detection by adopting a smart washer in conjunction with a sub-space state space identification algorithm. The smart washer is a cantilevered plate equipped with a piezoelectric sensor/actuator. The changes in the resonant frequencies of the washer were used to correlate the preload in joints.

Much work has also been done to address the problem of maintaining and returning preload to a bolted joint. Gaul (1997) produced a semi-active joint by utilizing piezoceramic stack actuators. The actuator was used to control the preload in the bolted joints as well as to suppress vibration in structures based on friction control. Park (2003) used a combination of shape memory alloys and piezoelectric sensors to both detect and repair the self-loosening damage in bolted joint structures. The piezoelectric sensor was used to measure the impedance of the structure. Once the loosening mode was identified, it was possible to restore the preload using the shape memory alloy actuator inserted between the bolt and nut.

Unfortunately, these methods have all had various limitations that make them unsuitable for field implementation. Until very recently, piezoelectric active sensing measurements required bulky, expensive data acquisition systems or impedance analyzers. Once a measurement is made there currently does not exist any good

algorithm to determine whether or not damage is present, where the damage is located, or what the magnitude of the damage is. One example of an algorithm applied to piezoelectric active sensing measurements is the cross correlation between a baseline measurement, and an operational measurement. For any appreciable number of data points this type of algorithms can quickly become memory intensive to the point where it is not realizable with the data storage available on a low cost, low speed microcontroller. Other problems associated with piezoelectric active sensing include allocating memory for a baseline measurement at every point on the structure, sensor diagnostics, and PZT-to-structure bond quality.

1.3 Review of the Impedance Method

1.3.1 Overview

The impedance method was first introduced by Liang (1994) at the Center for Intelligent Materials and Structures (CIMMS), Virginia Tech. Extensive research into the use of the impedance method for SHM continues today at a number of different locations around the world. This review of the impedance method will explore the properties of the piezoelectric materials that are used in the impedance method, the theory of operation behind the impedance method, structural health monitoring applications of the impedance method, and finally current limitations that need to be overcome before the impedance method is suitable for wide scale deployment on structures.

1.3.2 Piezoelectric materials

The sensors used for impedance method SHM are based on piezoelectric materials. Piezoelectric materials are materials that produce an electrical charge when mechanically strained. This phenomenon is known as the direct piezoelectric effect. The inverse piezoelectric effect occurs when the piezoelectric element produces a strain in response to an applied electric field. The piezoelectric effect was first discovered in 1880 by Jacques and Pierre Curie in the crystals of tourmaline, quartz, topaz, cane sugar, and Rochelle salt. Since the original discovery of the piezoelectric effect, a number of materials have been found to possess these properties including rubber, wool, silk, and even bone. Today a number of man-made piezoelectric materials exist for commercial use, including the ceramics Barium Titanate, Strontium Titanate, Lead Zirconate Titanate (PZT), and even the polymer Polyvinylidene Fluoride (PVDF).

In this investigation the ceramic material, Lead Zirconate Titanate (PZT), was used extensively as both an actuator and a sensor. The manufacture of PZT generally begins by ball milling the Lead Zirconate Titanate into a fine powder. The powder is mixed with an organic binder, formed into the desired shape, and then pressed. The pressed mixture is fired at around 750 C in order to remove the binder, and the remaining material is sintered at approximately 1350 C until the ceramic has a dense crystalline structure. The ceramic is formed to the finished shape by lapping, polishing, and cutting. Electrodes can be applied by either sputtering, (Kaufman 1982), or screen printing. In order to impart piezoelectric properties to the ceramic,

the final shape is placed in an oil or silicone bath which is heated to a temperature slightly below the Curie temperature of the PZT. The ceramic is maintained at this temperature while a strong electric field, generally on the order of several kV/mm, is applied across the ceramic. The application of the electric field is generally referred to as a poling treatment.

In order to understand the effects of the poling treatment, it is necessary to first understand the behavior of the perovskite crystals that make up the PZT ceramic. At temperatures above the Curie point, each crystal has a simple cubic symmetry with no dipole moment. At temperatures below the Curie point, each crystal now has a tetragonal or rhombohedral symmetry, and a dipole moment is present. Furthermore, crystals that are near each other tend to form regions with the same dipole alignment called domains. Each domain will have a net dipole moment, but the domains tend to be randomly dispersed throughout the material so the element has no net dipole moment. The poling treatment is used to cause the domains most aligned with the electric field to expand thus causing the element to lengthen in the direction of the field. When the field is removed, the majority of the dipoles are locked into a pattern of near alignment, thus resulting in a net polarization across the element. The net polarization is the cause of the piezoelectric effect in PZT.

1.3.3 Impedance Method, Theory and operation

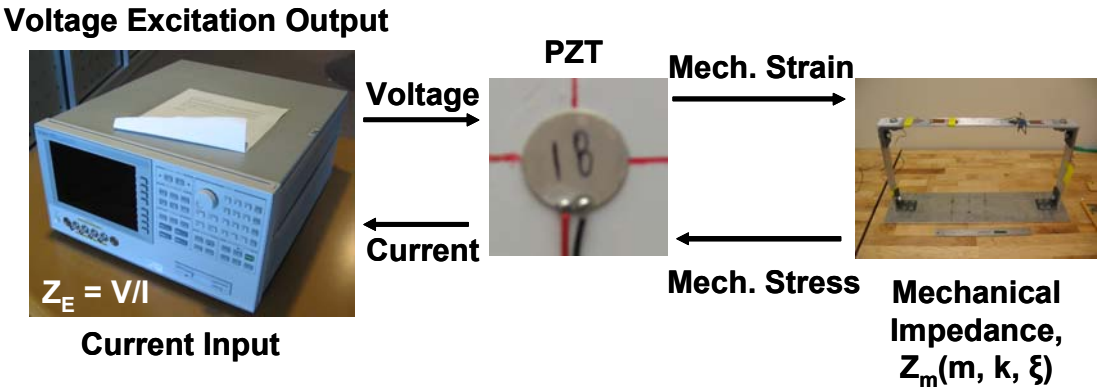

Figure 1-1: Block diagram of the impedance method

Impedance-based SHM is concerned with measuring the dynamics of a host structure by bonding a piezoelectric patch to a structure, thus coupling the electrical impedance of the patch with the mechanical impedance of the structure. The mechanical impedance is defined as:

$$Z_{mechanical} = \frac{Force}{Velocity} \qquad \textbf{Equation 1-1}$$

The operation of the impedance method as it is applied to structural health monitoring can be summarized as follows, see Figure 1-1:. First an impedance analyzer applies a sinusoidal excitation voltage to a PZT element which is bonded to a structure of interest. The electrical excitation causes a corresponding mechanical excitation in the PZT wafer, which is then coupled into the structure through the bond layer. The structural dynamics are excited based on the mechanical impedance of the structure, and a corresponding strain is placed on the PZT sensor. The structural strain causes a current output in the PZT sensor. The ratio between the applied voltage

excitation and current output from the patch is the electrical impedance measured by the impedance analyzer. Essentially the impedance analyzer measures the frequency response function of the structure over the bandwidth of excitation. As the structure is damaged, the mass, stiffness and damping properties will change. In the case of crack development, the stiffness of the structure will generally decrease. Any change in the mass, stiffness, or damping properties will lead to a change in the mechanical impedance, as well as the structural frequency response function measured by the impedance analyzer. Changes in the impedance measurement from the undamaged case can be used to detect whether or not damage has been introduced into the structure.

The theory behind the impedance method for structural health monitoring was first developed by Liang (1994). Liang considered the case where a PZT bar element was driving a spring-mass-damper system with a mechanical impedance Z(ω). The electrical impedance of the patch itself is given by $Z_a(\omega)$. The relation between mechanical impedance and electrical admittance is shown in Equation 1-2.

$$Y(\omega) = \frac{I}{V} = i\omega a\left(\varepsilon_{33}^{\ T} - \frac{Z(\omega)}{Z(\omega) - Z_a(\omega)} d_{3x}^2 Y_{xx}^E \right) \qquad \textbf{Equation 1-2}$$

Where "V" is the excitation voltage, "I" is the current output from the PZT, "a" is a geometric constant, $d_{3x,}^2$ is the piezoelectric coupling constant, Y_{xx}^E is the Young's modulus, and $\varepsilon_{33}^{\ T}$ is the dielectric constant of the PZT at the zero stress state. This equation shows that the electrical admittance is directly coupled to the mechanical impedance of the structure. Since admittance is simply the inverse of the impedance,

the host structure dynamics can be monitored by simply measuring the electrical impedance. Now it is important to note that the impedance of the PZT sensor is purely capacitive, so the imaginary portion of the impedance measurement will include both structural impedance information, as well as sensor impedance information. The real portion of the impedance measurement will only include structural impedance information. Therefore it is a common practice to only consider the real portion of the impedance measurement for SHM applications. The imaginary portion of the impedance measurement will be sensitive to changes in the PZT sensor capacitance caused by temperature changes. These variations are unwanted effects and can be ignored by simply considering the real portion of the impedance in SHM applications.

In order for an interrogation signal to be sensitive to small cracks and damage, it is necessary that the wavelength of any excitation be smaller than the characteristic wavelength of the damage to be detected (Stokes and Cloud, 1993). To facilitate the detection of small structural changes, a high frequency excitation must be used, so the impedance method is generally carried out between 10 – 400 kHz. This frequency range corresponds to wavelengths in aluminum between 16 mm to 63 cm. Generally only a subset of this total bandwidth is used for any given SHM application, but so far only trial and error approaches have been utilized to determine which bandwidth is appropriate for any given structure. It has been suggested by Sun (1995) that a frequency band with a high modal density should be selected because it will see a greater amount of structural information. This work will present a new method of

determining which frequency range of an impedance measurement should be used for structural health monitoring.

The high frequency range used for the impedance method has a number of advantages as outlined by Park (2003). First, it makes the effective sensing area small. The advantage is that it is easier to localize damage. Secondly, the localized damage area makes the PZT sensor less dependant on boundary conditions. Boundary conditions in real world structures are notoriously hard to characterize analytically, and tend to exhibit poor repeatability between structures. Lastly, the high frequencies make the sensor operation independent of any typical environmental or operational vibrations. Generally environmental mechanical vibrations do not extend into the tens to hundreds of kHz range, so they will have little effect on the operation of the impedance-based SHM system. Park (2000) investigated the effects of various operational conditions on the impedance method including external vibrations and temperature changes. Furthermore, when using a swept sine excitation, the impedance measurement equipment can be designed to filter out any excitation that does not occur at the current frequency point of interest.

Work has also gone into the practical aspects of the impedance method. Raju (1998) studied the effects of multiplexing, lead length, excitation voltage level, and ambient conditions. He found that lead lengths less than 30 m had no adverse effects on the impedance method. In addition he also found that the signal to noise ratio of impedance measurements could be improved by increasing the excitation voltage.

1.3.4 Applications

The impedance method has been applied to a wide range of problems since its first inception in 1994. After the initial development by Liang, Sun, Rogers (1994), Sun (1995) attempted to perform experimental modal measurements via piezoelectric impedance sensing. Sun (1995) also used the impedance method to test truss structures by employing a statistical algorithm to assess damage condition. In addition Sun (1995) studied the effect of different frequency ranges and excitation levels. Chaudhry (1995) used the impedance method to perform SHM on a Piper Model 601P airplane. In this work damage was introduced both locally and at a distance from the sensors. It was seen that the impedance method was extremely sensitive to local damage, and insensitive to distant damage. Abrasive wear and tooth bending fatigue in precision gears were successfully detected with the impedance method by Lalande (1996). The resin molding transfer process was monitored by Wang (1998) for composite manufacturing settings. In this work it was possible to correlate electro-mechanical response characteristics with both the area of a PZT wafer that was wetted with resin, as well as with the extent to which the resin had cured. A built-in-bridge structure has been investigated by both Ayres (1998), and Park (2000). The impedance method demonstrated its ability to detect damage on the bridge in spite of operational variations such as changing mass loading, and temperature fluctuations.

Damage in fiber reinforced plastic (FRP) composite materials has been studied extensively. Pohl (2001) studied the ability of the impedance method to detect low velocity impact damage in FRP plates. A method for detecting composite patch

disbond using the impedance method in conjunction with hybrid genetic algorithms was proposed by Xu and Liu (2002). Bois (2004) used PZT sensors with the impedance method to determine whether a composite laminated structure had suffered delamination damage. In future work they plan to monitor the delamination of the trailing edge of a helicopter blade.

1.3.5 Drawbacks and current challenges

Despite the many advantages of the impedance method, there are a number of hurdles that need to be overcome before it will be suitable for widespread use as a structural health monitoring solution. Many of these hurdles have been addressed in this research project.

First, the equipment used to measure impedance tends to be bulky, expensive and not suitable for deployment in typical environmental conditions. For example, the conventional Agilent 4294A impedance analyzer costs $41,000, measures 42.5cm X 22cm X 50cm, and weighs 25 kg. In addition it is not built to be used outside a lab, and it certainly is not meant to be incorporated in a wireless sensor node. A few researchers have addressed this equipment issue. Peairs (2004) proposed using a conventional spectrum analyzer in conjunction with a signal generator and a current measuring circuit to build an improvised impedance analyzer. Impedance measurements were made on bolted joint pipeline structures, and a C-channel composite beam. Peairs showed that his setup could make measurements that were

very similar in shape to the measurements made with a 4294A impedance analyzer. Further work using the improvised impedance method, were preformed by Grisso (2004), who proposed the use of the MEMS Augmented Structural Sensor patch, (MASSpatch). The MASSpatch was an attempt to build a wireless sensor node capable of performing impedance based structural health monitoring. An additional goal was to design the MASSpatch so it could be powered by energy harvested from ambient vibrations, and operate independently of a conventional battery source. Unfortunately the MASSpatch had a maximum frequency of about 8 kHz, which is at the very low end of the impedance method's normal bandwidth of operation. Clearly there is still a need for further work into designing low-cost wireless, impedance method based sensor nodes.

The number of data points associated with the impedance method can also be a problem in cases where size and power requirements are a primary concern. With conventional Static Random Access Memory (SRAM) and flash memory technology, it is trivial to store data, but many applications require sensor nodes that are as absolutely small as possible, and require as little power as possible. Adding additional memory leads to increases in both size and power requirements. It is preferable to only require the memory capabilities of the microcontroller, but many low power microcontrollers such as the one used in this work have 4 kilobytes (kB) or less of SRAM data storage. 4 kB of SRAM gets used very quickly when hundreds of data points, each consisting of 2B or more need to be saved. Further demands on data storage are introduced when calculations need to be performed on all the data points,

and feature extraction data must be saved. Most current research into the impedance method for SHM have required algorithms with heavy data storage burdens, such as the cross correlation. The main reason these computationally burdensome algorithms are used, is that the manner in which impedance measurements change as damage develops is not well understood. It would be preferable to find features in the impedance measurements that display changes with damage, and that do not require computationally burdensome algorithms to quantify. In this work a new paradigm for designing impedance sensors for ease of feature extraction is presented.

An additional problem with the impedance method is that work needs to continue on sensor diagnostics. It is possible that a measurement might be made with a damaged PZT patch. The damage in the PZT might give a false positive indicating structural damage has occurred when none is present. Work on sensor diagnostics has been performed by Park (2006). In Park's work the slope of the imaginary portion of the admittance of the PZT patch was used to determine both the bonding condition, as well as the structural health of the PZT patch itself. Park found that breakage in the sensor lead to a downward shift in the slope of the imaginary portion of the admittance measurement. A disbond of the PZT led to an upward shift in slope of the imaginary portion of the admittance. This work will include the application of Park's method for measuring the bond quality of PZT patches.

The purpose of this thesis is to explore methods to alleviate some of the challenges associated with making the impedance method a viable SHM solution. Extensive research has been performed to eliminate the need for large amounts of data

storage, making the equipment more appropriate in terms of size and cost for sensor network applications, and implementing sensor diagnostics in the sensor node.

1.4 Review of Energy Considerations for wireless sensor nodes

1.4.1 Overview

A major concern for all wireless sensor networks is the available energy supply. The conventional power supply for wireless sensor nodes is generally some form of battery. As sensor networks become more widespread, and involve more active elements, the battery power supply quickly becomes unsuitable from both an operational and maintenance standpoint. Limited power supply generally means the sensor node duty cycle must be decreased, and the maintenance budget must reflect costs associated with battery changes. The ideal solution would be to design sensor nodes with a power supply that does not need replacement over the entire projected lifetime of the sensor network. A number of different approaches have been studied in an attempt to obtain this ideal. Energy harvesting from sources such as the sun, and ambient vibrations have been studied in detail. The design of low power circuitry is constantly evolving to ease power requirements. Wireless RF power delivery systems have been studied extensively over the last fifty years. Lastly, various researchers have proposed new paradigms for distributing energy throughout a sensor network.

1.4.2 Energy Harvesting

A wide range of energy harvesting technologies which tap into energy sources such as solar energy, thermal energy, and ambient vibration energy, have been investigated. Current research work into these sources, excluding solar, has resulted in power supplies ranging from about 1mW maximum down to the tens and hundreds of microwatts range. Roundy (2002) characterized the power density of a number different power supplies suitable for sensor nodes. Roundy compares solar, vibration, temperature gradient, batteries and fuel cells over a one year lifetime and a ten year lifetime. Roundy's results show that solar with an energy density of 15,000 $\mu W/cm^3$ has a significantly higher power density than all the other energy schemes proposed. Piezoelectric based vibration power harvesting has an energy density of 250 $\mu W/cm^3$, and a 10 °C temperature gradient based energy harvester has a density of 15 $\mu W/cm^3$. These numbers can be compared to lithium batteries (45 $\mu W/cm^3$), hydrocarbon fuel (333 $\mu W/cm^3$), and methanol fuel cells (280 $\mu W/cm^3$). Solar cell technology is relatively mature so it will not be considered here. The following will be a review of vibration and thermoelectric power harvesting research.

One of the first known uses of vibrational power harvesting was in 1770 when Abraham-Louis Perrelet built the first known self-winding pedometer watch (Paradiso 2005). Self-winding watches gained wide use in the 1930's when a suitable watch cover was built to seal dirt out of the mechanism. Contemporary vibration power harvesting research has gone in three main directions, electromagnetic systems, electrostatic systems, and piezoelectric systems.

Electromagnetic systems rely on Faraday's law of induction. Generally a moving magnet is used to induce a current in a coil. A design scheme for building electromagnetic micro-generators is outlined by Amirtharajah (1998). Amirtharajah proposed the use of a magnetic inertial proof mass attached to a spring, which would move through a conductive coil. Calculations showed that the system should be able to output 400 μW of power. Amirtharajah's energy harvesting system successfully operated a finite impulse response (FIR) filter for 23 ms. Williams (2001) utilized micromachining techniques to build a mm size device which could output .3 μW at a few millivolts potential with an excitation frequency of 4 MHz. One example of a commercial device utilizing an electromagnetic harvesting system is the Forever Flashlight. This flashlight contains a sliding magnet in the handle which moves through a coil when shaken, in order to induce current in the coil. The shaking energy is then used to light up a low power LED.

Electrostatic based power generation is based on the idea of converting mechanical vibrations to electrical energy using a variable capacitor (Meninger, 2001). There are two available cycles for electrostatic energy conversion, the charge constrained conversion cycle, and the voltage constrained conversion cycle. One drawback to electrostatic energy generation is that the capacitors used in the system must first be charged to some initial voltage the value of which depends on the cycle that is used. The energy available in the voltage constrained cycle is greater than the energy available in the charge constrained cycle by a factor of V_{start}/V_{max}. The tradeoff is that the charge constrained cycle only requires a single charge source to

begin operation, and the voltage of the source can be significantly lower than the V_{max}. A very good overview of the electrostatic energy conversion can be found in Meninger (2001). In this work a micro-electro-mechanical system (MEMS) variable capacitor is used to harvest energy from a well established harmonic in an engine's vibration spectrum. When the electrostatic generator is subject to closed loop control for robust operation, it is anticipated that 5.6 μW of power will be available from the system.

Piezoelectric acoustic energy harvesting is based on the inverse piezoelectric effect. By introducing a strain across a PZT patch, an electrical charge is produced, which can be used to energize a capacitor. Hausler and Stein (1984) used the PVDF to build a piezoelectric generator for harvesting the vibrations caused by the breathing of a dog. They were able to get 17 μW of power out of the generator. Umeda (1996) designed a piezoelectric generator utilizing a piezoelectric vibrator and a steel ball. A model of the piezoelectric generator was built and the calculated output voltages were found to agree with the measured output voltages. The generator was found to have a maximum efficiency of 52%. Goldfarb and Jones (1999) investigated the use of a PZT stack for electrical energy generation. In their investigation they found that the majority of the produced energy was simply reflected back to the excitation source that caused it. In addition they found that at frequencies above 100 Hz, the stack system had very low efficiency, and the highest efficiency was obtained at 5 Hz. Gonzales (2001) investigated the use of the piezoelectric effect to supply power to wearable electronic devices. In this work the sources of mechanical energy in the human body are summarized. Sodano (2002) preformed an investigation into the

ability of a vibrating piezoelectric plate to recharge a battery. When the plate was vibrated at its resonant frequency, 2 mW of power were produced by the PZT. Sodano found that he could fully charge a battery from the fully discharged state using his PZT generator. Roundy (2003) designed a 1.9 GHz RF transmit beacon that could realize a 2.6% duty cycle entirely powered by a cantilever beam style piezoelectric generator. The piezoelectric beam generator could output 180 μW of power to a capacitive load at 2.25 m/s^2 of vibration.

1.4.3 Low Power Circuit Design

Research into energy harvesting has shown that in order to build a sensor node that requires only ambient energy for power will demand sensor node technology that utilizes very low power levels. Sensor nodes must run off power supplies on the order of tens to hundreds of μWs, and sub 1 V potentials. A large amount of research has gone into developing complementary metal-oxide semiconductor (CMOS) technology to fulfill these needs. The typical wireless active sensor node will contain certain building blocks necessary for operation. Examples include analog to digital converters, A/D, digital to analog converters, D/A, various forms of filters, Fast Fourier Transform (FFT) hardware, DC-DC converters, voltage references, telemetry hardware, and Very Large Scale Integration (VLSI) components such as microcontrollers. Each of these components uses energy in the sensor node, and is a candidate for power usage minimization research.

A short history of low power electronics and minimum bounds of power usage is given in Meindl (1997). Calhoun (2005) gives an overview of design considerations for ultra-low energy wireless micro-sensor nodes, which are meant to be powered by ambient mechanical vibrations harvested by piezoelectric generators. Calhoun discusses a number of methods to decrease the power usage of wireless micro sensor nodes including dynamic voltage scaling, energy scalable architectures, the use of multi-threshold CMOS, reducing start-up time, and stand-by voltage scaling. Furthermore an energy aware FFT algorithm is presented. Calhoun also points out that energy efficient wireless transmitters for short range communications typically use continuous phase modulation to reduce power supply. Continuous phase modulation removes the need for analog mixers and digital-to-analog converters found in conventional homodyne and heterodyne transmitters. Corbishley (2004) presents a method of implementing an ultra-low power analog directional gain system for hearing aids. In this work signals from two microphones a short distance apart are used to provide stereophonic hearing. Essentially an analog adaptive beamformer is built to filter out noise. An analog cross-correlation function is implemented by using continuous time first order low pass filters. The complete analog beamformer operates at .9 V while comsuming only 5 μW of power. Another example of hearing aid technology pushing the limits of low-power design is given by van Dijk (1998). In this work a low power audio delay line for directional hearing aids is presented. The delay line operates at 1.8 V and consumes 1.1 μA of current, which was within their design goals. Cho (1994) presents an overview of design considerations for low

power A/D converters with sampling rates greater than 1 MHz. Cho illustrates his approach using results from an experimental 20 mega sample per second (MSPS), A/D converter with a power consumption of 35 mW. Yamagishi (1998) presented a low power Direct Digital Synthesis (DDS) frequency synthesizer chip for wireless data transmission. This chip operated from a 2 V supply and consumed 160 mW at 2 GHz. These numbers are not particularly impressive today, but to display how the technology has evolved, Otis (2003) utilized MEMS technology to build a 1.9 GHz oscillator that only consumed 300 μW from a 1V supply. Camploo (2003) presented a method of performing efficient charge recovery for driving piezoelectric actuators with Quasi-Square waves. Camploo was studying biomimetric locomotion for small insect-like robots, so he only concerned himself with low frequency applications at 150 Hz and voltage levels of 3-10 V. Without any attempt at component optimization he was able to recovery 56% of his piezoelectric actuation energy. Despite the low frequency emphasis, this work might have application in a PZT-based active sensor node, and is worth further consideration.

Considerable research has also gone into adaptive power supplies. Wei (1999) presented a fully digital adaptive power supply regulator with an efficiency of greater than 90%. Wei (2001) continued his adaptive power supply work and went on to build an energy efficient parallel I/O interface which could operate between .2-.8 Gb/s. Kim (2002) extended Wei's work by building a serial I/O link based on the adaptive power supply. The serial link could operate at 650 Mb/s - 5Gb/s over a supply range of .9 - 2.5 V. Dancy (2000) presented a high efficiency multiple output DC-DC

converter for low voltage systems. The DC-DC converter was specifically designed to delivery tens of milliwatts for low power systems such as cell phones and PDAs. The DC-DC converter was based on a pulse width modulator, and it had a power dissipation of 100 μW.

1.4.4 RF Power Delivery

The energy harvesting schemes discussed thus far are generally only able to produce on the order of tens of μWs of power (Calhoun, 2005). At this low power level, it is not practical for devices that must maintain a high duty cycle, so it is necessary to turn to other possible sources of power. One possible solution is wireless RF power delivery. By delivering power wirelessly through RF energy it is not necessary to worry about installing expensive hard-wiring, or batteries that might need to be replaced.

An early history of RF power delivery is given by Brown (1984) and will be briefly summarized here. The first pioneer in wireless power delivery was Heinrich Hertz. Hertz demonstrated electromagnetic wave propagation in free space with a spark gap to both generate, and detect high frequency power. Hertz then took the next step and tried to focus the electromagnetic waves with parabolic reflectors. The next major pioneer in wireless power delivery was Nikola Tesla. Tesla made his first attempt to transmit power without wires at Colorado Springs, Colorado in 1899. The Tesla coil was resonated at 150 kHz, and was powered by 300 kW. It is unclear how

much power was radiated into space, and if any was collected at a distant point. Tesla also tried to build a Tesla coil in Suffolk County, Long Island, which was expected to have a copper electrode 100 ft. in diameter. Unfortunately Tesla ran out of money shortly before the completion of his facility, which was eventually torn down during the First World War. Research on RF power delivery did not take any major steps forward until after World War Two, which had brought about the development of the velocity modulated beam tube, and the microwave cavity magnetron. Despite the advances of World War II in antennas and radar, there still did not exist a device to change microwave energy into DC energy. The first successful demonstration of a microwave power delivery system was carried out under the Direction of William Brown in May of 1963. Air Force and Department of Defense Officials met at Raytheon to witness the generation of microwave power that was then transmitted via horn illuminated ellipsoid reflectors over a distance of 20 ft. Of the 400 W which were generated, 100 W of DC power was received. The microwave energy was converted to DC with a closely spaced thermionic diode rectifier. Unfortunately the thermionic diode rectifier was an unreliable device. Luckily, Brown discovered the work of Roscoe George who had been carrying out experiments on dense arrays of microwave semiconductor diodes. Another problem with the microwave transmission system was the low collection efficiency and directivity of the horn receiver. In order to solve this problem Brown attached his full wave rectifiers to half wave dipoles and put a reflecting plane behind them. The idea was to make the aperture of the receiver highly non-directive. The new microwave energy receiver became known as the

rectenna. In order to demonstrate the microwave to DC conversion performance of the rectenna, Brown completed the first microwave powered helicopter flight on July 1, 1964. The first flight was only able to achieve a few inches of altitude, but it was entirely powered by microwave energy. Shortly thereafter in November of 1964, Brown successfully flew his helicopter for ten hours in both rain and windy conditions at an altitude of 50 ft. Brown and his collaborators went on to build a beam riding helicopter, but funds for the work dried up between 1965 and 1970. During this period Brown continued work on the rectenna with his own money at a home work shop in his spare time. Renewed interest in the development of the rectenna began in 1968 when Dr. Peter Glaser proposed the solar-powered satellite (SPS) concept. SPS consisted of a satellite in geosynchronous orbit which would capture the sun's energy, convert it to microwaves, and beam it back to earth. NASA eventually funded RF power delivery research once again. Demonstrations during this project included the delivery of 30 kW over a 1 mile distance in the 1973-1974 time period. Another interesting development during the SPS project, was the discovery that microwave oven magnetrons were suitable for delivering power to rectenna arrays. It was originally believed that microwave oven magnetrons were very noisy, but when Raytheon began testing the signal to noise ratio of the magnetrons they found that they needed special test equipment to properly measure the quiet signals. Eventually the SPS program ended in 1980. Support for rectenna research then came from interest in microwave powered aircraft, prompted by NASA in 1976. The first thin film etched rectenna was developed in response to Wallops Flight facility's interest to wirelessly

power balloons. It was realized that the rectenna would need a different physical form to be deployable on aerospace structures. One application of the thin film etched rectenna was a microwave powered airplane. Wallop's also made a conceptual design of a ground-based phased array with a tracking control system to deliver power to moving aerospace structures outfitted with rectennas.

More contemporary examples of RF power delivery include passive RFID tags used for replacing bar codes, research into microwave powered surface tension control applications for solar reflectors and space based telescopes.

Both passive and active RFID technology has received considerable attention in the last few years as a means of inventory control, and to a lesser extent as a sensor node remote powering method. The current investigation is solely concerned with delivering power to sensor nodes, so only passive RFID technology will be considered here. Commercial passive RFID technology is available at 125 kHz, Finkenzeller (2003), and 900 MHz, Atmel(2005). Research has also gone into developing passive RFID tags at 2.4 GHz, Heikkinen (2001), and in the ultra high frequency (UHF) band, Seemann (2005). These RFID tags typically run on tens of μW of power, and transmit data using load modulation techniques. Typical read distances for passive RFID tags are on the order of meters.

Extensive rectenna research has been directed toward controlling the shapes of solar sails, membrane structures, and Gossamer spacecrafts (Choi, 2002). Lightweight flexible structures such as solar collectors, space antennas, and large aperture space telescopes generally require some form of surface tension control to ensure the

structure performs its intended function (Song, 2003). Maintaining a focal point at a certain location is one example. Thin layer composite unimorph ferroectric driver and sensor (THUNDER) actuators have been considered for such shape control applications, but conventional arrays of THUNDER actuators require a large wire network, which adds weight and decreases the performance of the membrane structure under control. Microwave driven rectenna arrays have been considered as an alternative power source to alleviate the wiring problem. Epp (2000) studied the use of a dual-polarized rectenna to facilitate achieving the high voltages (200-300 V) associated with actuator applications. Epp was able to use dual polarization to achieve an output voltage of 50 V, which represents a doubling of the voltage available in the single polarization case. Choi (2000) utilized a power allocation and distribution (PAD) circuit for networking power to the appropriate actuators. Choi (2002) was able to increase the output voltage of the rectenna to 70 V, and in 2003 he successfully achieved output voltages between 200-300 V with an 18 W, X band power source, at a distance of 1.8m. It is clear that rectenna technology is slowly becoming more suitable for surface compensation control problems. It should also be noted that the RF energy delivery system has only focused on the powering of larger devices such as actuators or helicopters. The applications to low power electronics, such as the wireless sensor node applications presented in this thesis, has not been substantially investigated. .

Rectennas have also been investigated for RF power harvesting applications. Slavova (2003), designed and simulated a wideband rectenna for recycling RF energy

between 4.5 to 8 GHz. Slavova's design utilized an input filter to prevent DC currents and higher harmonics from flowing back to the antenna. Hagerty (2004), studied the rectification of broad-band, statistically time-varying, low-power density, microwave radiation. Hagerty designed and built a rectenna made up of an array of 90° sequentially rotated, right and left hand equiangular spirals for dual polarization. The rectenna was expected to generally be operated in microwave power densities of 10^{-5} to 10^{-1} mW/cm^2, over a frequency range of 2 to 18 GHz. Efficiencies on the order of 20% averaged over time, frequency and polarization were reported in the case of arbitrarily polarized low incident power density, microwave radiation.

One invariant of RF power delivery that has on and off received interest for the last couple of decades, is laser energy transmission. Laser energy transmission is similar to harvesting solar energy with photovoltaic cells, except that it can be made much more efficient. Conventional sun light is a broad band excitation source, while photovotaic cells typically have a very narrow-band frequency response. The result is that around 80% of the solar energy is lost, Shatchtman and Bushman (2003). Lasers output a monochromatic illumination, so if the receiving photovoltaic cell is tuned to the wavelength of the laser output, energy conversion can be made more efficient. Yugami (1997) reports efficiencies between 45 to 65 %, except in the case of falling snow interfering with the laser path. Wireless energy transfers in space, and from the earth to space have been proposed by Walker (1994). Young (1991) proposed the use of laser energy beaming for powering a lunar rover. Contemporary research on laser energy beaming has been performed by Fork (2001). Fork predicts that the

infrastructure needed for solar power delivery from space will be available in the next 40 years.

1.4.5 Sensor Network Paradigms

In recent years a number of new sensor network paradigms have been presented in an attempt to solve the problem of low energy availability for large scale sensor networks with long service lives.

Dove (2006) presented the use of relay based hardware, used in conjunction with wireless telemetry to implement a hierarchal wireless sensor network. In the hierarchal sensor network, several active sensors are connected to relay-based hardware, or "black boxes," which serves as both multiplexers and signal routers. Multiple black boxes are then connected to a decentralized data control and processing station. The processing station contains data acquisition boards, processors, and wireless telemetry to relay the data back to a centralized monitoring station which outputs information to the user. The black box was specifically designed to accommodate piezoelectric active sensing approaches for SHM. Furthermore, normal commercialized multiplexers tend to be strictly passive in nature, while the black box both routes and multiplexes signals. Multiple black boxes can easily be daisy chained together to form larger sensor networks, thus making the hierarchal sensor network scalable.

Kansal (2003) presented a new method for task scheduling among environmentally powered sensor nodes, based on the spatio-temporal characteristics of the environmentally available power. Kansal argues that energy availability is typically not homogenous throughout the spatial and temporal distribution of a sensor network. Therefore, it is naive to expect every sensor node to be able to perform the same number of operations at all times. Instead tasks should be distributed throughout the network based on the energy availability of the individual nodes. Kansal reports 200% improvements in sensor network lifetimes by using his environmental energy awareness methodology. Rahimi (2003) took a slightly different approach to the non-homogenous nature of energy distribution throughout a sensor network. Rahimi proposes allowing a small percentage of the sensor nodes to be mobile, in order that they might be able to move in search of energy-rich areas of the environment. The mobile nodes could then collect energy and deliver it to immobile nodes in energy-poor areas of the environment. Rahimi showed that an unmodified sensor network which would partition in half a day could be made sustainable with the addition of 40% mobile nodes.

Todd (2005) proposed the use of mobile nodes to wirelessly deliver all the power necessary to sensor nodes as needed. Furthermore, sensor node data would be wirelessly transmitted to the mobile node which would also serve as a centralized data repository. The mobile node in this case would require a battery power supply, but in a typical sensor network there would be a minimal number of mobile nodes in order to keep maintenance costs at a minimum. One advantage of this form of sensor network

paradigm is that nodes do not need to be within hopping protocol distance. Furthermore, redundant components such as memory and computing can be eliminated from the sensor network. In addition the sensors do not need to be powered except during a read cycle. The sensor node developed in this thesis was designed to operate within the framework described by Todd.

1.5 Review of SHM sensor node technology

As embedded computing technologies evolve, new possibilities open up in wireless sensor networking. Sensor nodes are operating at lower power levels, and realizing higher frequency measurements than ever before. Gordon (2004) attempted to develop a sensor node for the wireless retrieval of the vital signs of a mouse via RFID. Conventional needle-based methods for measuring the vital signs of a mouse tend to have a measurable effect on the heart rate, respiration rate, blood pressure, etc of the mouse, so it would be preferable to utilize less traumatic methods. An evaluation board prototype of the system was built and tested using off the shelf RFID technology. Microstrain has done considerable work on using inductive coupling methods for powering sensor nodes that cannot use batteries. One of their accomplishments is the integration of piezoelectric sensors, wireless telemetry, and a titanium knee replacement for the *in vivo* measurement of the forces on the human knee (Townsend, 1999). The telemetry and sensors are hermetically sealed inside the knee implant, so it is necessary to power the sensor node with magnetic near field

coupling at 1.5 kHz. By measuring the forces inside the knee it will be possible to validate knee implant models, as well as to better design knee therapy treatments. Lynch (2004) developed a wireless active sensing node for structural health monitoring, which was demonstrated on an aluminum plate structure. The sensor node software detects damage in a structure by calculating an autoregressive with exogenous inputs (ARX) time series model of the structural dynamics, and comparing the transfer function poles with the poles measured in an undamaged structure. Liu (2005) developed a wireless sensor node for high frequency applications. The sensor node features a field programmable gate array (FPGA) for co-control, modular design, and ultrasonic sensing abilities. It is shown that the sensor node can successfully measure 100 kHz sinusoidal signals.

Considerable work has been performed into developing wireless sensor nodes, but there is still more work to be done. Active sensor nodes have been successfully built and implemented, and passive sensor nodes which run off inductively delivered power have been implemented. The next step is to build an active sensor node that can run off power supplied by either ambient energy, or wirelessly delivered power. The work of this thesis takes a step in the direction of such a sensor node.

Chapter 2 Piezoelectric (PZT) Enhanced Washer

2.1 Overview

As stated in the previous chapter, the impedance method is very effective in detecting and locating structural damage. However, one of the major obstacles encountered with the impedance method is that the measurements generally do not contain any distinguishable features that are simple to calculate analytically. The dynamics of a structure are generally difficult to simulate in the tens to hundreds of kHz range, where both standing and guided wave behavior is supported, and the effects of damage on the structure in this frequency range are even more difficult to predict. In general, no attempt is made to predict the effects of damage on an impedance measurement as damage progresses, so the actual effects of a loss in structural integrity are not known until after the structure has failed. The lack of *a priori* knowledge of the structural response forces the development of complicated damage detection algorithms in an unsupervised learning mode. These damage detection algorithms typically require the storage of a large number of frequency points for a baseline measurement, as well as each operational measurement. An additional problem with deploying these algorithms is that every PZT sensor on a typical structure will require its own baseline measurement. Each sensor on the structure is measuring different dynamics, so every sensor's baseline measurement will be unique (although in principle, there may be significant correlation among

sensor pairs). The memory required for saving baseline data for every sensor quickly accumulates in a wireless sensor node, which must rely on power supplied by portable energy sources. Furthermore, if multiple nominally similar structures are outfitted with the same array of PZT sensors, baseline measurements between similar sensors on different structures will display different baseline measurements. Impedance measurements are notorious for lacking repeatability on structures with any level of complexity due to factors such as adhesive bond variations, fastener preload dissimilarities, and manufacturing inconsistencies. The lack of repeatability eliminates the possibility of obtaining data from one damaged structure, and directly relating it to damage in another nominally similar structure. In order for the impedance method to gain more widespread acceptance, it will be necessary for these problems to be resolved. It should be mentioned that most active-sensing SHM techniques that use piezoelectric materials possess the same problems.

The ideal solution to the problems mentioned above would be to implement PZT sensors with features that changed in a very distinct and predictable/repeatable manner as damage is introduced. Every sensor should exhibit similar changes with damage and have a high degree of repeatability. In other words, local structural dynamics should not be able to interfere with the operation of the sensor. In this thesis, the first attempt to try and attain these goals for the bolted joint preload monitoring problem is proposed and experimentally verified.

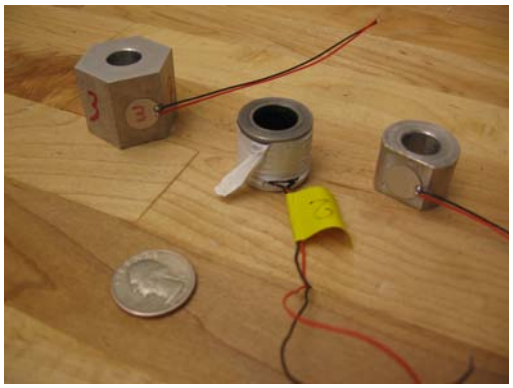

Figure 2-1: Various forms of PZT enhanced washers

A new family of PZT enhance washers were developed as shown in Figure 2-1. The current PZT enhanced washers can be divided into two general classes. One class of PZT washer is made up of a ring-type PZT stack actuator, Figure 2-2. The PZT stack is employed on a bolted joint in a manner similar to a conventional washer.

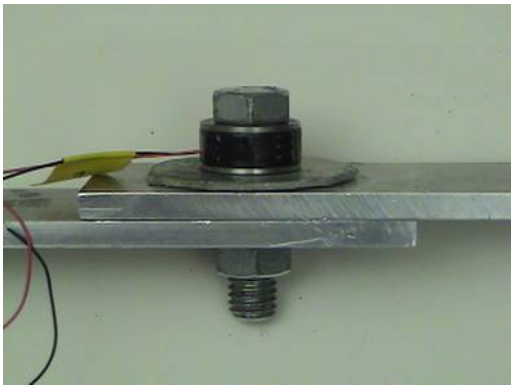

Figure 2-2: Ring actuator-type PZT enhanced washer in use

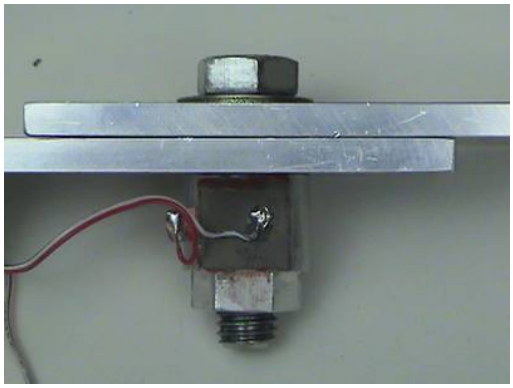

Figure 2-3: PZT enhanced nut in use

The next class of PZT enhanced washer, is composed of a piece of bar stock with a hole drilled through its axis, and a flat milled on one side to accommodate the attachment of a PZT patch, Figure 2-3. This chapter will present the design of the PZT enhanced washer, the dynamic behavior of the PZT washers, and will show that they provide a generalized baseline for every bolted joint under consideration. Furthermore, the PZT enhanced washer has dynamic characteristics that are very simple to characterize and quantify. These dynamic characteristics have been shown to be repeatable and insensitive to host dynamics.

2.2 Dynamic Behavior of PZT Enhanced Washers Under Varying Preload

2.2.1 Analytical Dynamic Behavior of the PZT enhanced washer

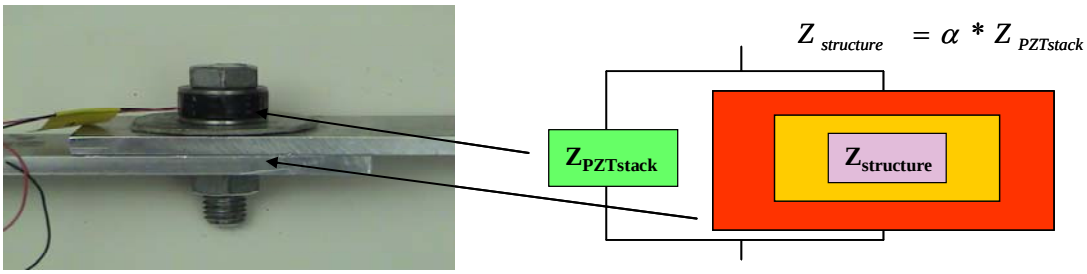

Figure 2-4: Bolted joint impedance dynamics

The general dynamic behavior of the PZT enhanced washer can be described by the simple model shown in Figure 2-4. The net impedance of the system under investigation can be broken down into two main parts; the impedance of the PZT

enhanced washer and the impedance of the bolted joint structure. The increase in the preload can be defined as an increase in the impedance of the structure. Assume the structural impedance can take the form:

$$Z_{structure} = \alpha * Z_{PZTstack} \quad \textbf{Equation 2-1}$$

Where Z indicates the ratio of force divided by velocity (structural impedance), and α is the preload parameter. The force-velocity relationship for the system can be written as:

$$F = (Z_{structure} + Z_{PZTstack}) * \dot{X} \quad \textbf{Equation 2-2}$$

Where F is the force and $\dot{X}$ is the velocity. Combining Equation 2-1 and Equation 2-2, and assuming a harmonic forcing function, the relation can be rewritten:

$$F = j\omega * (1+\alpha) * Z_{PZTstack} * X \quad \textbf{Equation 2-3}$$

Where $j = \sqrt{-1}$, and ω is the circular frequency of the forcing function. Equation 2-3 can be rearranged to form:

$$\frac{X}{F} = \frac{1}{(1+\alpha) * j\omega * Z_{PZTstack}} \quad \textbf{Equation 2-4}$$

Equation 2-4 is equivalent to the net displacement vs. force frequency response function H_{net}:

$$H_{net} = \frac{1}{(1+\alpha) * j\omega * Z_{PZTstack}} \quad \textbf{Equation 2-5}$$

For the case that the PZT stack is free of the structure, $\alpha = 0$ and the remaining expression is:

$$H_{net}(\alpha = 0) = \frac{1}{j\omega * Z_{PZTstack}} = H$$ **Equation 2-6**

So for the general tightened case we have:

$$H_{net} = \frac{H}{(1+\alpha)}$$ **Equation 2-7**

As the value of the preload increases, α increases, and the value of the structural impedance also increases. Eventually the structural impedance increases so much that it totally overwhelms the mechanical impedance of the PZT enhanced washer, and the dynamics of the total system are dominated by the structural impedance. Equation 2-7 shows that the result of a large structural impedance is a low magnitude value for the net frequency response function. The electro-mechanical impedance measurement that is obtained from the PZT patch correlates with the frequency response function, so it is reasonable to see a decrease in the electro-mechanical response, if the torque is increased..

The theory behind the PZT enhanced washer can be illustrated very clearly by assuming the impedance of the PZT stack can be represented by the impedance of a single degree of freedom (SDOF) oscillator .

$$Z_{SDOF} = \frac{j\omega * m * C + k * m}{C + \frac{k}{j\omega} + j\omega * m}$$ **Equation 2-8**

This SDOF model is a reasonable approximation to the actual dynamic response of the PZT stack, because the stacks generally have a single dominant peak in the 10 – 100 kHz range. In addition, the assumption that the structure dynamics is proportional to the PZT stack dynamics is reasonable for preliminary modeling purposes. The resulting H_{net} as would be measured by the impedance analyzer has been plotted in Figure 2-5 for increasing preload parameter values of α. From this simulation we see that the resonant peak of the single DOF system decreases as the preload parameter increases. Furthermore, the height of the resonant peak changes much more dramatically at lower "α" values than at the higher "α" values. From this simulation, it seems reasonable to expect that the bolt preload can easily be identified by tracking the magnitude of the resonance of the PZT stack. In addition, the PZT stack can be applied to any bolt on any structure, and similar dynamic behavior can be expected. By employing sensors with a similar dynamic response regardless of the structure to which it is applied, significant memory savings can be achieved because only one baseline measurement needs to be saved for all the sensors. Furthermore, only very simple algorithms are required to quantify the resonant peak characteristics.

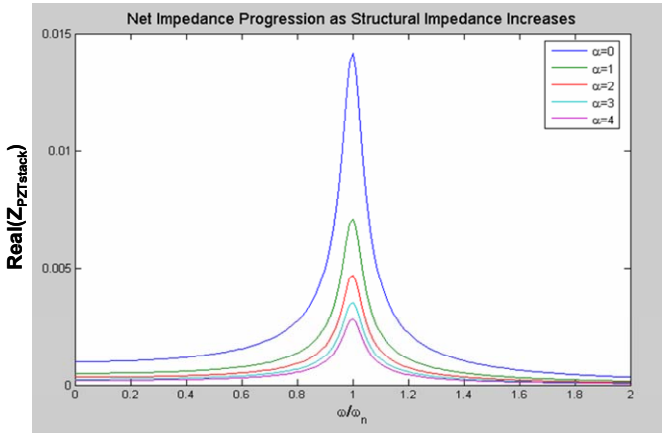

Figure 2-5: Analytical impedance magnitude progression as bolt preload parameter increases.

2.2.2 Isolation Washers

In initial lap joint experiments, the PZT stack was placed underneath the bolt head in a manner similar to a conventional washer. Torque would then be applied with a torque wrench to a predetermined level, and an impedance measurement was made in a frequency band that contained the first resonant peak of the PZT stack. It was quickly discovered that placing the PZT stack directly in contact with the structure led to the transmission of lap joint dynamics into the measurement of the PZT stack dynamics. In order to build a sensor with a generalized baseline measurement, it would be necessary to isolate the stack dynamics from the structural dynamics, so the isolation washer was developed. The isolation washer would be placed between the lap joint and the PZT stack in order to damp out any structural dynamics that might corrupt the PZT stack impedance measurement. Four different versions of the isolation washer are shown in Figure 2-6.

Figure 2-6: Various isolation washers, from left to right, rubber washer, fender washer with epoxy coating, fender washer with JB weld epoxy coating, conventional ½" washer with epoxy coating.

The initial isolation washer is shown at the far left of Figure 2-6. This washer is simply a piece of rubber with a clearance hole for the bolt to slide through. This washer was very effective at damping out structural vibrations, but it was determined that this form of washer may not be suitable for a wide range of environments. Furthermore, the compliant nature of the rubber was deemed unacceptable for some bolted joint applications. The rubber has both poor load transfer characteristics, as well as unacceptably low resilience to environmental conditions. The goal called for a material that would facilitate energy dissipation, while having a reasonable amount of stiffness. Stiffness and energy dissipation properties are generally mutually exclusive characteristics of a material, so there was no obvious first choice. A number of polymer washers were investigated, but they did not have the required damping characteristics. Eventually the epoxy washer, as represented by the three washers on the right of Figure 2-6, was developed to achieve an acceptable tradeoff between stiffness and damping. The epoxy washer is simply a conventional washer with an epoxy coating on one side to provide structural damping. The epoxy washer displayed damping characteristics that were comparable to the rubber washer, while still maintaining a stiffness value that was deemed reasonable for preliminary research.

2.2.3 Experimental Setup and Results

Once the structural isolation problem was solved, measurements on the PZT stack with varying preload levels could resume. In order to verify that the aforementioned model corresponds to actual impedance measurement, the dynamics of the PZT stack type washer was considered first. Two different PZT stacks were evaluated and the characteristics of these stacks are shown in Table 2-1.

Table 2-1: PZT stack parameter comparison

Stack	Max Stroke (micrometers)	Stiffness (N/micrometer)	Length (mm)	Resonant Freq (kHz)
HPSt 1000/25-15/5	12 to 7	1200	9	50
HPSt 1000/25-15/25	35 to 25	400	27	25

The dominant feature that was considered in this investigation was the first resonant peak. The goal was to correlate the frequency and magnitude of the resonant peak with the preload level experienced by the bolt. The theory outlined above suggests that the resonant peak of the PZT washer should decrease in magnitude as increasing torque is applied to the bolt.

In these experiments, a lap joint made from two aluminum beams 6.4 mm thick and 50.8 mm wide was constructed. The joint was held together with a ½-13, grade 5 bolt, and the PZT stack and an isolation washer was placed under the head of the threaded fastener. An example of the test setup is shown in Figure 2-4. The bolt was totally loosened between each measurement and then tightened to the specified preload level. Impedance measurements were made with an Agilent 4294A

impedance analyzer and the real portion of these measurements were considered for study due to its insensitivity to temperature effects. Figure 2-7 and Figure 2-8 show the result of applying various torque levels to the two PZT ring actuators described in Table 2-1.

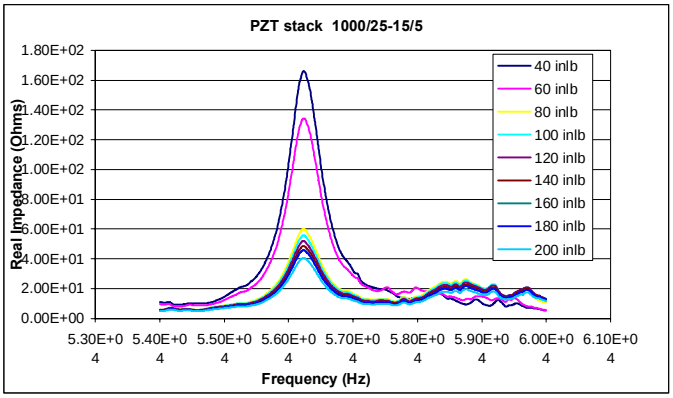

Figure 2-7: PZT ring-type stack actuator 1000/25-15/5, real portion of impedance

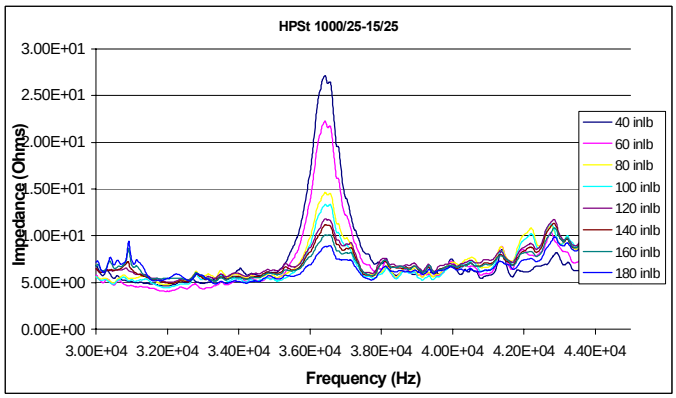

Figure 2-8: PZT ring-type stack actuator 1000/25-15/25, real portion of impedance

From these two plots it is possible to see that the real portion of the resonant peak decreases in magnitude as the torque level increases. This result is in accordance with the theory outlined above. Another interesting aspect of these measurements is that the change in the peak is most pronounced between 60 and 80 in*lb for both PZT

stacks. The theory supports this form of behavior. Figure 2-5 shows a theoretical simulation of the impedance measurement associated with a one degree-of-freedom, spring-mass system, with an increasing preload parameter "α". The height of this peak changes much more dramatically at lower "α" values than at the higher "α" values. The measurement of the PZT stacks also show small changes in the height of the peak when the preload level is high.

The study of the dynamic characteristics of the PZT stack with changing preload shows that changes at low preload levels will be easier to distinguish than changes at higher preload levels. The fact that the measurements display smaller changes in the impedance peak value at high preload levels than at low preload levels confirms this observation.

2.2.4 Wafer-Based PZT enhanced washer

Next the dynamics of the wafer–based PZT enhanced washer need to be considered. The wafer based PZT enhanced washers were originally developed in an effort to reduce the cost from the originally implemented PZT stack version. The PZT wafer is oriented on the washer in such a way that the preload on the washer will have the most effect on the dynamics of the PZT wafer. The current theory associated with the dynamic behavior of the wafer-based PZT enhanced nut is identical to the theory associated with the PZT stack. It is expected that as preload is applied to the washer, the response measured by the impedance analyzer should decrease.

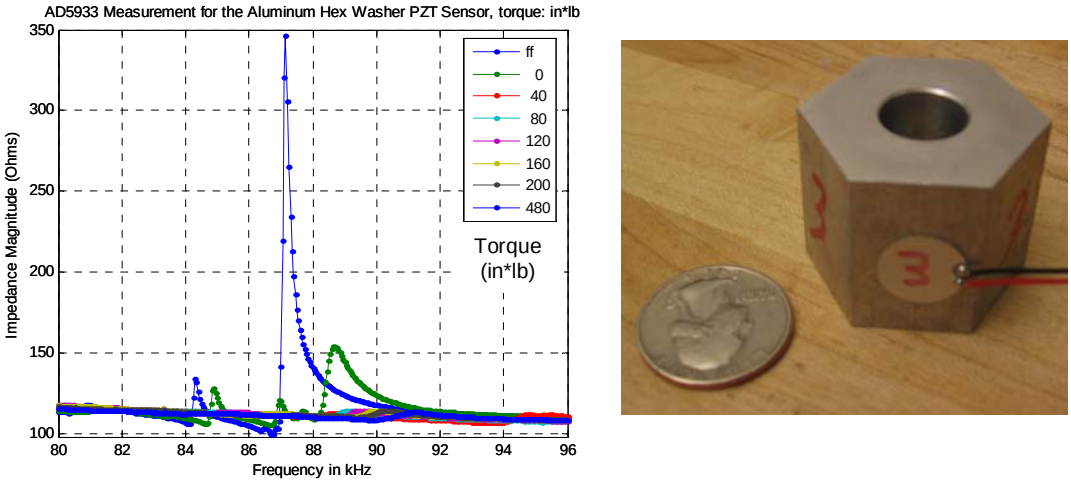

Figure 2-9: Aluminum-hex, PZT-enhanced washer and corresponding impedance measurement. Impedance values have been scaled by data acquisition and are shown for comparison purposes only

Figure 2-9, shows an impedance magnitude measurement taken from an aluminum-hex PZT enhanced washer. A very distinct resonant peak was measured between 86 and 90 kHz, so special attention was paid to this bandwidth in order to determine whether or not this peak would change in a manner suitable for SHM of bolted joints. Future measurements discussed in this thesis will show the behavior that is measured with this washer is similar to observations associated with all wafer-based PZT enhanced washers of a similar height, regardless of cross section, or material choice between steel or aluminum. In the free-free condition the washer displays a very sharp resonant peak. As preload is applied to the washer, the peak shifts to a slightly higher frequency, and if more preload is added, the dominant peak is totally suppressed. The extreme nature of the peak change makes quantifying the value of the preload level almost impossible with this configuration. It is, however, very simple to tell whether or not the bolt has come totally loose.

2.3 Generalized Baseline and Repeatability

This section will explain why the PZT enhanced washer is a suitable candidate for a generalized baseline sensor. The repeatability of the sensor will be explored, along with the sensitivity of the sensor to host-structure dynamics. The quality of the bond between the washer and PZT patch will also be quantified using the method pioneered by Park (2006). Work on the PZT ring-type stack actuator has been put on hold for the time being because of the cost differential between the PZT stack, and the wafer-based PZT enhanced washer.

In order for the PZT enhanced washer to be a suitable candidate for a generalized baseline sensor, it must demonstrate a given level of repeatability, which will mainly depend on the sensitivity of the feature extraction method and the damage detection algorithm. In the case of the PZT enhanced washer the feature under consideration is the magnitude and frequency of the resonant peak as measured by the real portion of the impedance method. It will be necessary to characterize the repeatability of this feature in order to evaluate the suitability of the PZT enhanced nut as a generalized baseline sensor.

In order to characterize the repeatability of the PZT enhanced washer, an experiment was set up as shown in Figure 2-10.

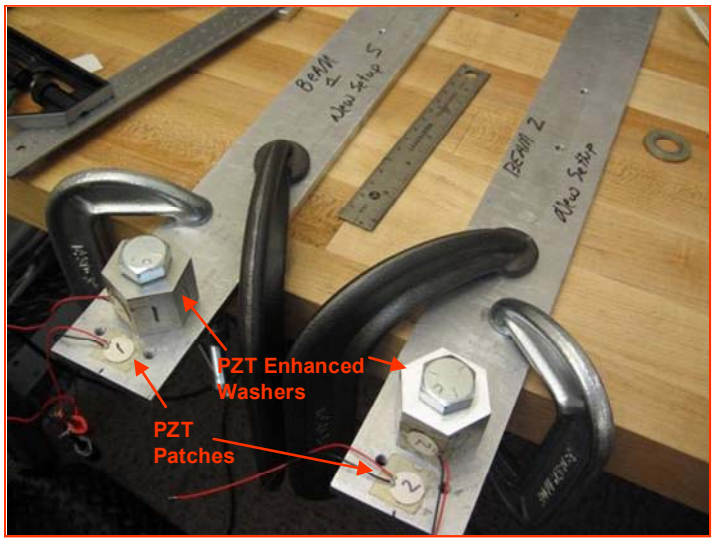

Figure 2-10: PZT aluminum-hex washer repeatability experiment

Two nominally similar aluminum hex washers were fabricated measuring 31.75 mm across the flats and 25.4 mm high. A 12.7 mm hole is drilled thru the center of each washer for a ½-13 bolt. The bolts were placed on nominally identical aluminum beams which were overhanging from a wooden workbench. The bolts were tightened to predetermined torque levels and impedance measurements were taken. Between each measurement the bolts were loosened, and the same torque wrench setting was used for both washers. Impedance measurements were made using the low-cost impedance method (Peairs 2004) and a National Instruments NI PXI-1042Q data acquisition system. Band-limited white noise was used as an excitation signal. The resulting real portion of the impedance measurements from 80 to 95 kHz can be found in Figure 2-11.

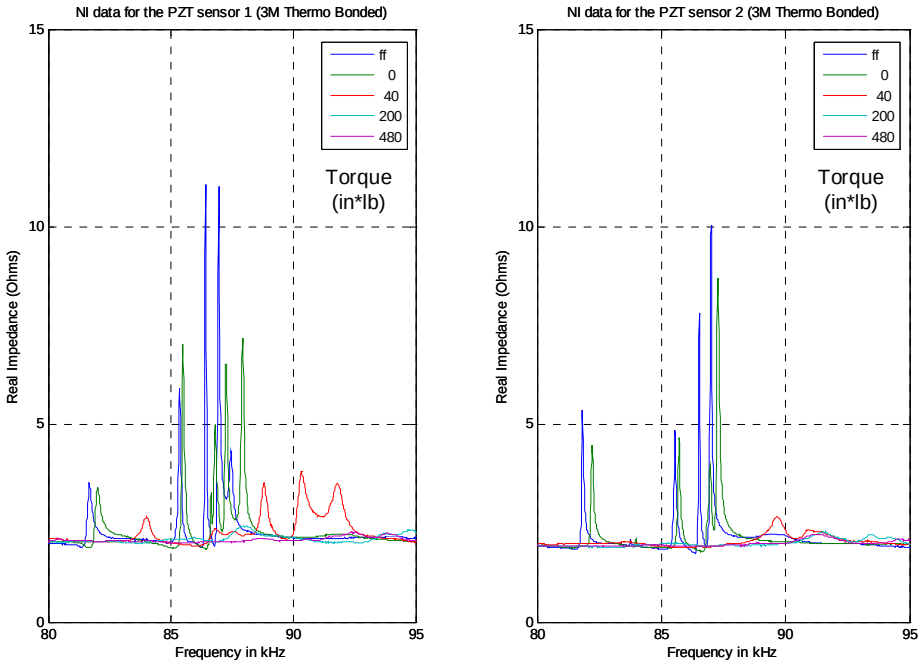

Figure 2-11: Repeatability between two PZT hex washers.

The impedance measurements from the two washers have differences, but the main peaks are present in both measurements. Perhaps more importantly, the majority of the response has died out after 40 in*lb of toque has been applied to the bolt. A number of different algorithms should be able to produce acceptable damage detection results using these dynamic measurements. Simply measuring the peak value over this bandwidth would be an effective measure of whether or not the bolt has come loose. Other possibilities include the sum of squared magnitudes, first moment, or even the sum of squared differences from a baseline measurement. One primary observation is that it appears that it is not necessary to use more complicated, memory intensive measures such as the cross correlation, to determine whether or not a bolt has come loose.

The next experiment that was performed consisted of measuring the response of two PZT enhanced washers with nominally similar geometry. The difference between the two washers is that one is constructed from steel, and the other is constructed from aluminum as shown in

Figure 2-12.

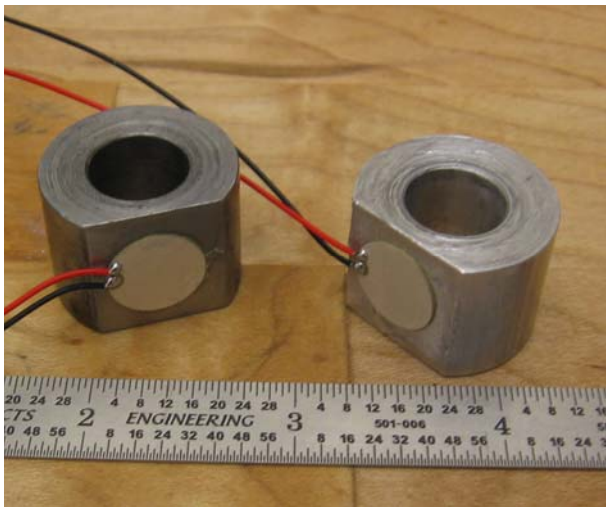

Figure 2-12: Cylindrical steel and aluminum PZT enhanced washers

These two washers both measure 19 mm high, and are made from 25.4 mm bar stock. A 12.7 mm hole has been drilled down the axis of each piece of bar stock for the insertion of a ½-13 bolt. A 3 mm deep flat has been milled on the side of each washer to facilitate the attachment of a PZT wafer sensor. The two sensors were then placed on beams similar to those used in the first repeatability test, and the same procedure and equipment was used to measure the real portion of the impedance over a bandwidth of 30 to 100 kHz. The resulting measurements are shown in Figure 2-13. A first observation of these plots show that two of the most prominent peaks in both plots occur at nearly the same frequency. There is one peak at around 38 kHz that is

common to both plots, and there is another common peak in both measurements between 80 and 95 kHz. The fact that the dynamics of the two washers are so similar should come as little surprise. Aluminum and steel have similar stiffness to weight ratios, so both washers will have the same stiffness and mass distributions, which in turn has the largest effect on the resonant frequencies. There are some additional peaks that occur in both measurements that are not necessarily common to both plots, but in both cases they are generally small relative to the dominant peaks. In addition we see that the impedance values in the steel case are higher than the values in the aluminum case. The lower impedance values in the aluminum case can be attributed to the impedance match between the aluminum beam and the aluminum washer. Energy is able to transfer away from the aluminum washer more easily than the steel washer. From these observations it is possible to conclude that if the same damage detection algorithm will be used on PZT enhanced washers composed of different materials with similar geometries, it would be wise to make the algorithm insensitive to impedance magnitudes. The algorithm should be more sensitive to the shape of the impedance measurement.

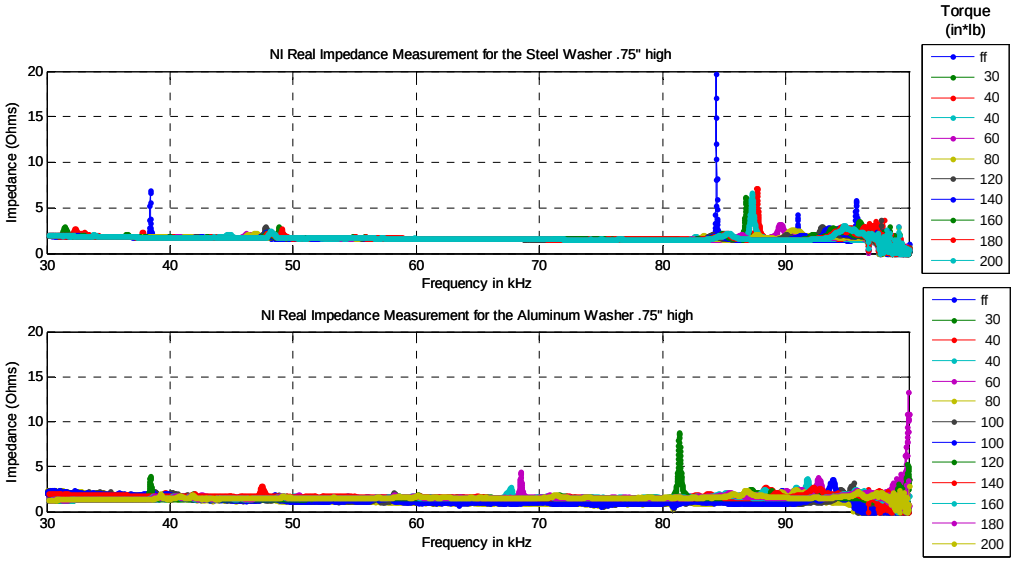

Figure 2-13: Real portion of the impedance for the aluminum and steel washers

One last observation of these measurements is that the dominant peak occurring between 80 and 90 kHz seems to be very similar to the dominant peak of the aluminum hex washers shown in Figure 2-11. The only difference is that the dominant peak is in the 85 to 90 kHz range. A ten kHz frequency range is a very reasonable bandwidth for operational measurements. If a 6-mm difference in height only has about a 5 kHz effect on the resonant peak, small differences in PZT enhanced washers caused by manufacturing tolerances should have a marginal effect on the sensor's operation.

The PZT enhanced washers have consistently displayed a resonant peak in the 80 to 90 kHz band which is sensitive to changes in bolt preload. There are, however, some differences between sensors such as additional peaks, and the magnitudes of the measurements. Further work should be done to better understand the causes of these

differences so PZT enhanced washers with better preload resolution performance can be designed and manufactured.

2.4 Insensitivity to Host Dynamics

On a typical structure outfitted with an array of piezoelectric sensors, every sensor will have a different baseline measurement simply because every sensor is measuring different dynamics. It is true that throughout a structure, the dynamic responses will be linearly correlated, but the complex nature of most structures, along with the high frequency nature of impedance measurements, makes finding the correlation difficult using analytical or numerical methods. Standard practice calls for making a baseline measurement for every sensor. In order for a generalized baseline sensor to work properly, it is imperative that the host structure dynamics have a minimal effect on the standardized baseline and the sensor's response to structural damage. In order to test the sensitivity of the PZT enhanced washer to local structural dynamics, a test was set up with the overhanging aluminum beams, and the PZT hex washers used in the repeatability study. In this test however, additional PZT patches were bonded to the beam structures in order to get a better measurement of the structural dynamics. The sensors on the aluminum beams can be seen in Figure 2-10. The same loosening and tightening procedure was followed as in other tests. The same National Instruments data acquisition system was used to measure the real portion of the impedance. The only difference was that at every tightness level, an

additional measurement of the beam mounted PZT patch was made in order to see if any resonances seen in the structure corresponded to resonant peaks in the PZT enhanced washer measurement. Figure 2-14 shows the real portion of the impedance measurements for both the aluminum beams and the PZT enhanced hex washers, over a frequency range of 30 to 95 kHz. The beam measurements over this frequency range show no significant dynamics in the beam, relative to the peaks in the PZT enhanced washers. The conclusion is that in this case the dynamics of the washers themselves are the main contributor to the impedance measurements. In beam 2 there is a beam resonances centered around 60 kHz. These beam dynamics do not seem to have any noticeable effect on the measurements for PZT washer 2. It is also important to note that the PZT washer dynamics do not seem to couple into the dynamics of the beams. The peaks associated with the washers are very pronounced, but there is no sign of them in either of the beam measurements. If reciprocity is assumed in this system, it can be concluded that since the high profile washer dynamics do not show in the beam measurements, then high profile beam dynamics will not show up in the washer measurements. The advantage here is that this form of PZT enhanced washer is insensitive to host structure dynamics. In addition, this PZT enhanced washer does not require an isolation washer as the PZT ring-type stack actuator did.

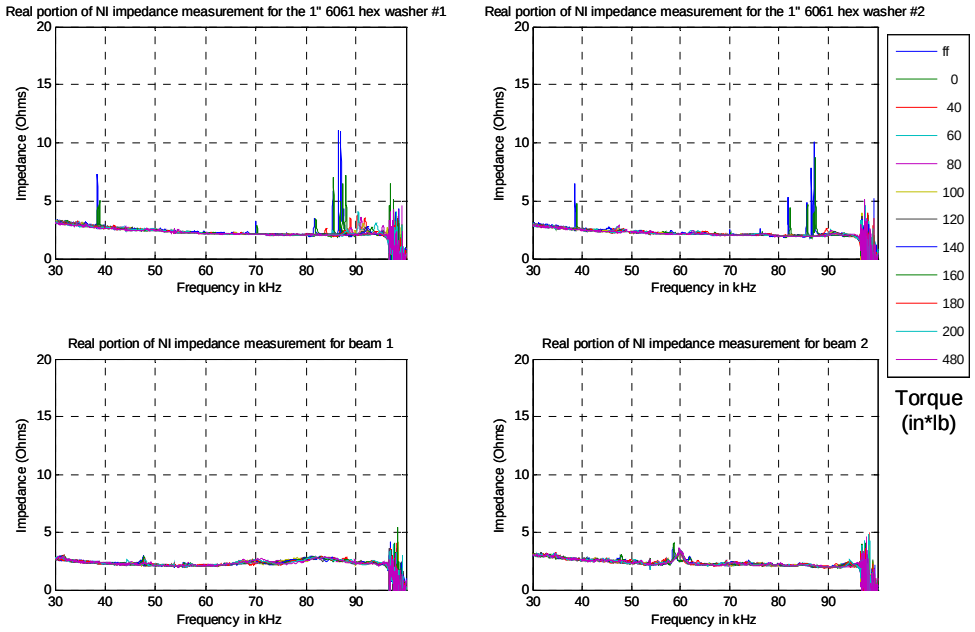

Figure 2-14: Real portion of the impedance measurements for the aluminum-hex washers and aluminum beams. Impedance values have been scaled by data acquisition and are shown for comparison purposes only.

The extended bandwidth used in this test allows another observation on repeatability as well. Both 25.4mm high hex washers display a resonant peak at around 38 kHz. This peak matches the peak seen in both 19 mm washers shown in Figure 2-13. Further advances in PZT enhanced washer technology could be obtained, if the mechanism that causes these similarities in resonant peaks for different geometries were better understood.

2.5 Effects of Bond Quality and its Characterization

The mechanical attachment between the PZT patch and the structure is usually obtained by using some form of polymer adhesive. Popular choices include epoxies,

thermo bond adhesives, and cyanoacrylate (superglue). Whenever a sensor is bonded using a polymer adhesive, the question of how the bond layer quality can be characterized and quantified always comes up. The generalized baseline sensor problem asks, "what is the effect of bond quality is on repeatability?" In order to test the repeatability of PZT enhanced washer measurements in the face of bond quality uncertainty, a single 25.4 mm high PZT aluminum hex washer was instrumented with four PZT patches. Two of the patches were applied with 3M thermo-bond, and the other two patches were bonded with conventional cyanoacrylate. The goal was to have every sensor measure the dynamics of as similar a structure as possible while characterizing the quality of the bond. Figure 2-15 shows a picture of the instrumented PZT aluminum hex washer. Two similar PZT sensors are bonded on the opposite faces, which are hidden from view. The "1h" designation indicates a 3M thermo-bonded sensor, and the "1sg" indicates a sensor attached with super-glue.

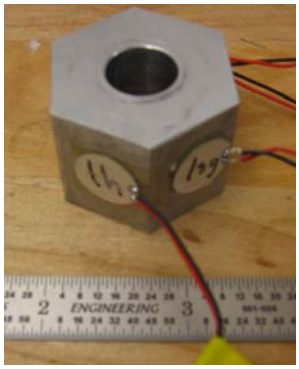

Figure 2-15: Aluminum-hex PZT washer with 2 super-glued sensors, and 2 themo-bonded sensors

The PZT enhanced washer was once again placed on the overhanging aluminum beams, and the same standard preload application was repeated on this

washer. At each preload level, a measurement was obtained from all four sensors with the National Instruments data acquisition system. The resulting real portion of the impedance measurements are shown in Figure 2-16.

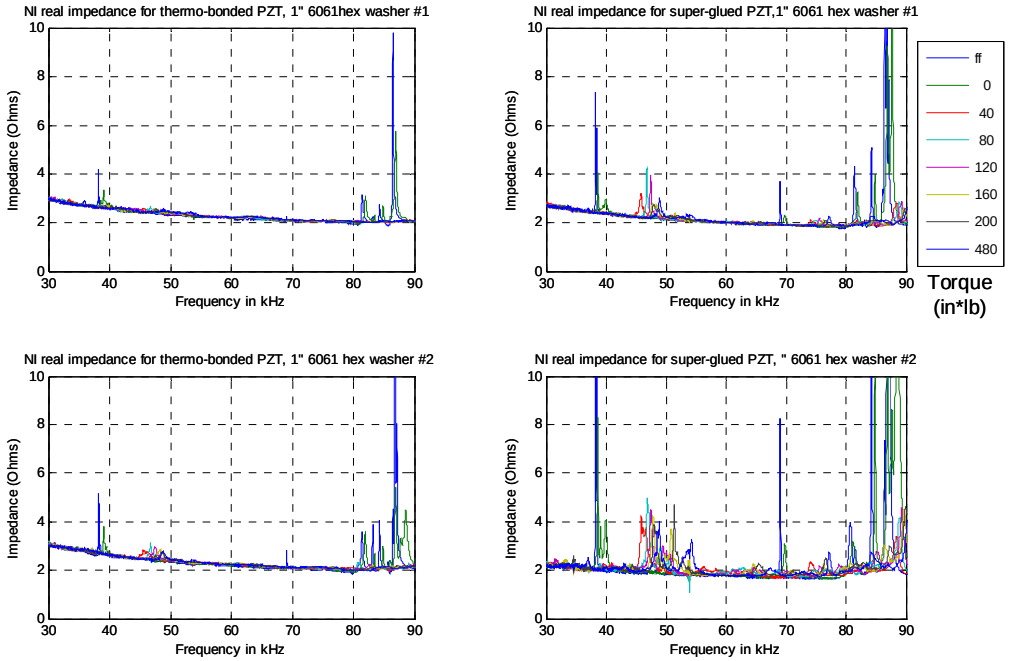

Figure 2-16: Real portion of the impedance measurements for various bonding conditions.

The plots in Figure 2-16, all use the same y axis so the main features of the impedance measurements could be compared. In both of the super-glued sensor cases, the dominant peaks are significantly larger than in either of the thermo-bonded cases. The peaks in the super glued cases actually extend out into the hundreds of Ohms range, on the scaled axes. The 3M thermo-bond is elastomeric in nature and lacks stiffness. Therefore the thermo-bond is less capable of transferring strain from the PZT patch to the structure, and *vice versa*. The loss of strain transfer is the cause of smaller impedance measurements with the 3M thermo-bond. The super-glue on the other

hand, has a higher stiffness than the thermo-bond, and is more capable of transferring strain from the patch to the structure. The higher stiffness of the super glue results in higher impedance measurements. Differences in measurement magnitude between the two thermo-bonded cases and the two super-glued cases can be attributed to variations in the bonding process. Clearly, simply using the same bond material does not lead to high repeatability in the magnitudes of the impedance measurements.

In order to gain higher repeatability, it will be necessary to employ some method of characterizing and quantifying the bond quality. The method pioneered by Park (2006) will be employed for this purpose. Park's method uses the imaginary portion of the admittance in order to ascertain how the capacitive nature of the PZT sensors is changing. Changes in the imaginary portion of the admittance can be used as a sensor diagnostic quantity, as well as an adhesive bond quality indicator. Admittance measurements of each of the four patches were made over a frequency range of 0 to 20 kHz as shown in Figure 2-17.

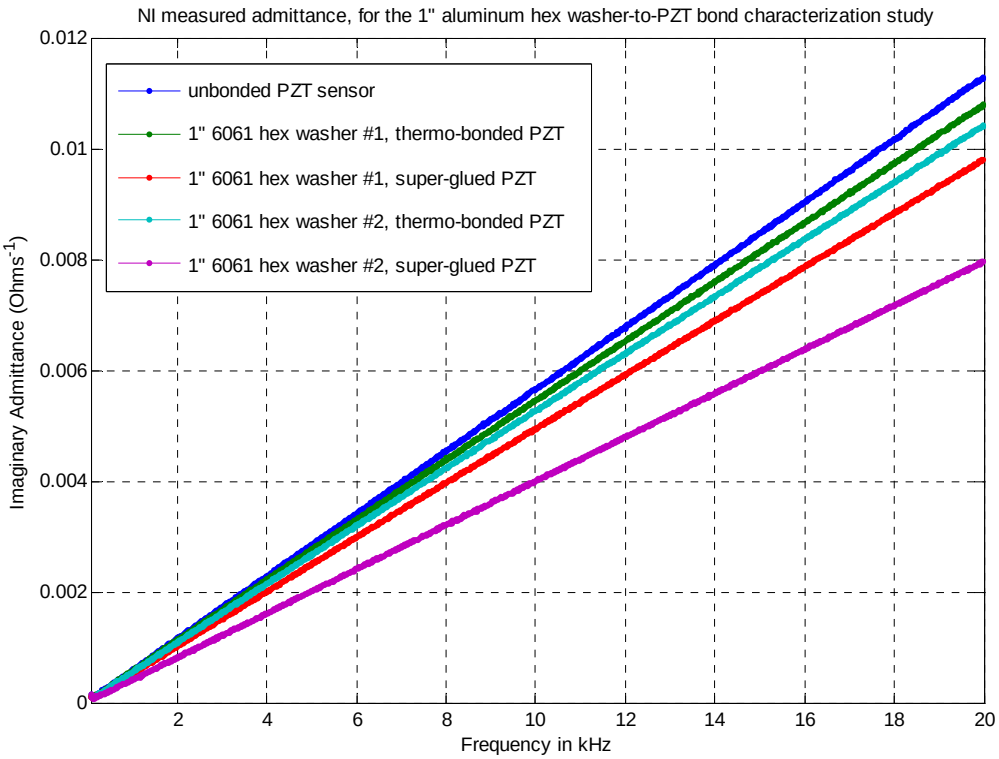

Figure 2-17: Imaginary portion of admittance values for the four bonding conditions. Admittance values have been scaled by data acquisition and are shown for comparison purposes only.

The plot also includes an admittance measurement of an un-bonded PZT patch. The imaginary portion of the admittance values show that as the PZT bond quality improves, the slope of the imaginary portion of the admittance decreases. The second super-glued sensor did have the largest response values in Figure 2-16, followed by the first super-glued sensor and the second thermo-bonded sensor. The first thermo-bonded sensor had the lowest response, and thus it has the second highest slope in the imaginary portion of the admittance measurement. The highest slope is achieved by the un-bonded PZT sensor, as expected. In a manufacturing setting, the slope of the imaginary portion of the admittance measurement could be used to quantify the

quality of the bond. Once the bond quality is quantified, it is possible that it may be better monitored and controlled in order to improve repeatability.

2.6 Summary

A new bolted-joint monitoring device has been developed. The PZT enhanced washers possesses a generalized baseline, and also measures the effects of joint damage independent of host structural dynamics. A series of tests have been performed on the PZT enhanced washers in order to verify their feasibility for engineering applications. The PZT enhanced washers have been demonstrated to be repeatable and insensitive to host structure dynamics. Furthermore, a first step has been taken to quantify any variations in the sensors caused by bonding quality. Perhaps most important of all, these low-cost PZT enhanced washers have very distinct peaks that change in easily quantified ways as the preload in the bolt is decreased. Algorithms that simply identify a maximum magnitude could be used to determine whether or not a bolt has come loose. Complicated, memory- and energy-intensive algorithms are no longer needed to quantify changes in the integrity of a structure.

The current state of the PZT washer is such that false-positives indicating a bolt has come loose are extremely unlikely due to the radical change in the resonant peak magnitude as preload is initially applied to the joint. The performance of the PZT washer in conjunction with the sensor node will be further discussed in chapter 3. The

washer displays a very prominent peak when the bolt has come loose. As preload is progressively applied to the bolt, the peak is quickly repressed. The whole impedance measurement over 80 to 90 kHz is very flat under any appreciable amount of preload. These sensor characteristics make the current PZT enhanced washer impractical for quantifying the amount of preload on the bolt. Future versions of the PZT enhanced washer will involve designing the structure of the washer so an easily distinguishable feature changes in a more smooth fashion over a larger range of preload values. In addition, further investigation will be focused on developing more advanced modeling techniques for predicting the dynamic response of more generalized geometries of PZT enhanced washers. Despite the shortcoming of the PZT enhanced washer, it is considerably easier to apply to the autonomously-monitored bolted-joint problem than the majority of solutions that have been presented in the literature.

Chapter 3 Impedance method-based wireless sensor node for SHM

3.1 Overview

A large amount of research has been focused on utilizing the impedance method for structural health monitoring. The vast majority of this research however has required the use of expensive and bulky impedance analyzers that are not suitable for field deployment. Furthermore, the impedance analyzers used for the measurements typically contain a large number of additional features that are not utilized for structural health monitoring. Recently, Analog Devices developed a single chip solution for acquiring impedance measurements over the 10 to 100 kHz frequency range. This frequency bandwidth corresponds to the bandwidth most commonly used for impedance-based structural health monitoring. Furthermore, the impedance chips are low cost, consume low amounts of power (on the order of mW), and include the ability to make temperature measurements, which can be helpful when performing sensor diagnostics.

The advent of the single chip solution for impedance measurements has opened the door for the application of impedance-based SHM for large-scale wireless sensor networks. This chapter will be concerned with the design, fabrication, and testing of a prototype impedance-based SHM wireless sensor node. The sensor node layout will be presented. The sensor node components will be explained, and the power requirements of the sensor node will be tabulated. Furthermore, the sensor node has been tested on several different structural health monitoring problems. The results of

these tests will be disclosed. The development of the impedance-based wireless sensor node is a significant step forward in moving the impedance method from the lab to actual field use.

3.2 AD5933 characteristics and operation

Analog Devices, Inc has recently developed two new single chip impedance measurement devices. The chips under consideration are the AD5933 and the AD5934. These two chips are nearly identical in operation, power requirements, and features. The only difference between the two chips is that the AD5933 has a 1 mega sample per second (MSPS) sampling rate, and the AD5934 has a 250 kSPS sampling rate. The higher sampling rate of the AD5933 leads to a slightly higher cost of $6.95 per chip vs. $4.35 for an AD5934. The cost difference has been deemed be negligible for this application considering the higher performance that can be achieved with the AD5933. The remainder of the work in this thesis has been performed with the AD5933. An evaluation board for the AD5933/AD5934 can be purchased from Analog Devices for $150.00. The board comes with software that controls the parameters of the chip via a USB interface.

The general operation of the chip can be outlined as follows. A 24-bit direct digital synthesis (DDS) core produces a digitized sine wave of the desired interrogation frequency. The excitation signal is then passed through a programmable gain stage and output into the device of interest. The current output from the device

caused by the excitation signal is then passed through a current-to-voltage amplifier, which features a user-selectable feedback resistor in order to vary the amplifier gain. The amplifier feedback resistor must be sized appropriately in order to ensure that the signal remains in the linear range of the analog-to-digital converter (ADC). The output from the current to voltage amplifier is then sent through a low-pass anti-aliasing filter and sent to a 12-bit, 1-MSPS ADC. A Hanning window is applied to the digital data, and a 1024 point discrete Fourier transform (DFT) is performed at the frequency point of interest. The resulting real and imaginary values of the DFT are passed to a microcontroller in twos complement format. This procedure is repeated for every point in the desired frequency sweep.

3.3 Comparison of Agilent 4294A Impedance Analyzer and AD5933

In order to illustrate the magnitude of the contribution for which the AD5933 is responsible, a comparison was made between a conventional Agilent 4294A impedance analyzer, Figure 3-1, and the AD5933, as outlined by the red square in Figure 3-2.

Figure 3-1: Agilent 4294A impedance analyzer, $41K

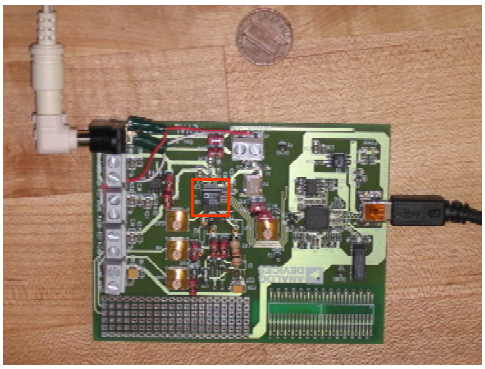

Figure 3-2: AD5933 development board, $150

The performance characteristics of these two impedance measurement systems have been tabulated in Table 3-1 for ease of comparison.

Table 3-1: Impedance measurement solution comparison

	Agilent 4294A	AD5933	Unit
Cost	41000	eval board: 150, chip: 6.95	$
Dimensions	500 X 225 X 425	eval board: 100 X 75 X 15	mm
Frequency Range	40 Hz to 110 MHz	~10 kHz to 100 kHz	
max points/sweep	801	512	points
ADC Sampling Rate	(at least) 220	1	MSPS
ADC resolution	not available	12	bit
Power Supply Voltage	120 AC	3.3 DC	V

From Table 3-1 it is apparent that the performance of the Agilent 4294A is superior to the performance of the AD5933, except in the areas of cost and size, and power supply. It should be noted however that many of the superior features of the Agilent 4294A are not utilized in SHM applications. For example, most SHM impedance measurements are made between 10 kHz and 200 kHz, so the majority of the Agilent 4294A bandwidth is not used in SHM applications. In contrast, the entire frequency

range of the AD5933 is usable for SHM applications. SHM applications typically require a large array of sensor nodes distributed across a structure. Wide scale deployment requires that the sensor nodes be low cost, as well as small and lightweight. The Agilent 4294A does not satisfy either requirement, but the AD5933--at $6.65 with a chip footprint of 6 mm X 5 mm, addresses both cost and size and constraints. Furthermore, sensor nodes are often applied to a structure after the design and construction phases are complete. Adding the hard-wired 120 V AC connections required for an Agilent 4294A based sensor node, after construction is complete, is often prohibitively expensive. In contrast, a sensor node utilizing the AD5933 could be powered by conventional batteries since the normal operation current draw is only 10 mA. Clearly, the AD5933 provides the means for building impedance based sensor nodes. Recently, Researchers from Virginia Tech have developed a snap-on impedance measurement device, referred to as the MASSPatch, (Grisso 2004). Although precise energy comparisons have not been made, the power requirements of the AD5933-based impedance measurement solution are significantly lower than those of the MASSpatch, which requires 900 mA at 5 VDC.

3.4 Sensor Node Layout and Components

3.4.1 Sensor node Layout and Operation

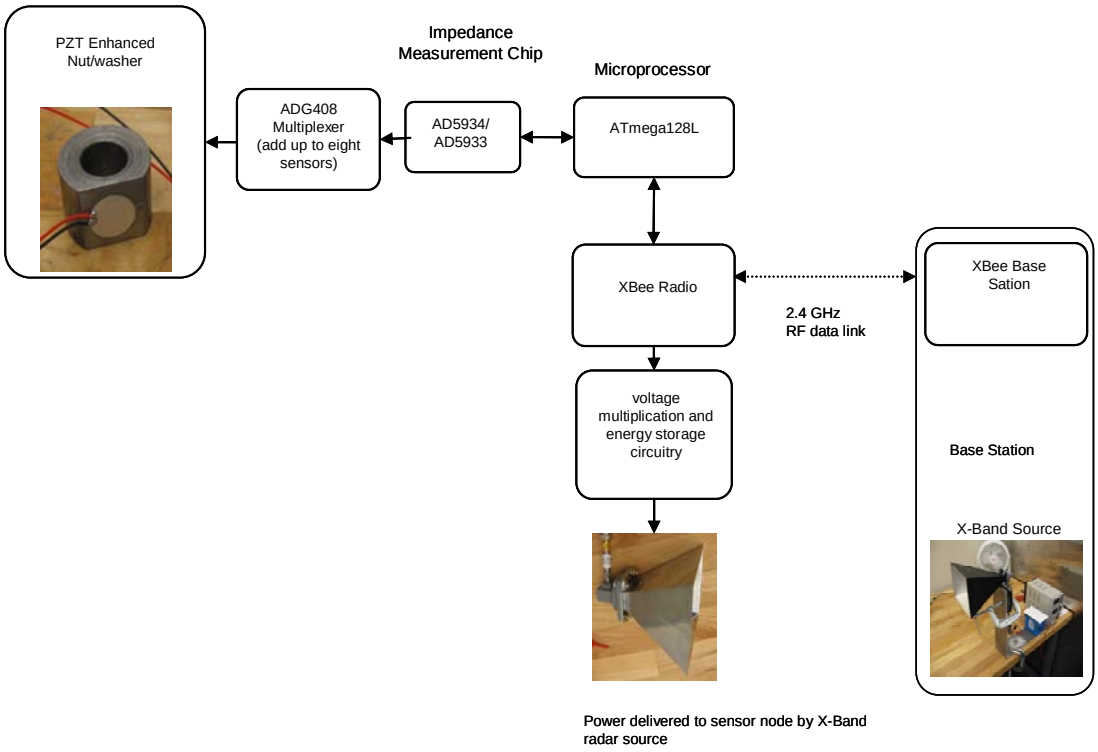

Figure 3-3: Block diagram of proposed sensor node

A block diagram of the proposed impedance-based wireless sensor node developed for bolted joint monitoring is presented in Figure 3-3. The bolted joint preload sensor node utilizes the PZT enhanced washer, The AD5933 impedance measurement chip, an ATmega128L microcontroller, and a 2.4 GHz Xbee radio for wireless data telemetry. In addition, the sensor node includes an X-band rectenna for supplying the required power for the electronic devices. The design consideration for the various components will be considered in this chapter. The X-band rectenna will be further discussed in Chapter 4.

The operation of the sensor node is as follows. First the microcontroller sends an initialization signal, commanding the sensor node to perform a frequency sweep. In this investigation, the initialize sweep command was usually sent to the microcontroller manually using a dip switch. Once the "initiate sweep" command has been received, the microcontroller programs the appropriate frequency sweep parameters into the AD5933 registers using a two-wire interface (TWI). The sweep parameters include start frequency, delta frequency increment, number of frequency points, and settling time between frequency points. Once the registers have been programmed, the microcontroller sends the "start sweep" command over the TWI and the AD5933 excites the PZT active-sensors with the initial frequency value. The current output from the device under test is converted into a voltage value, which is then run through the ADC. A Hanning window is applied to the digital data and the DFT is calculated. The real and imaginary portions of the DFT are then recorded by the microcontroller. The microcontroller sends a command to the AD5933 to move to the next frequency point. Once the data from all the frequency points have been recorded, the microcontroller implements a damage detection algorithm (based on measured changes in impedance peaks) in order to determine whether or not the bolt is loose. The "loose" or "tight" message is then sent via Universal Asynchronous Receiver/Transmitter (UART) from the microcontroller to the Xbee radio. The Xbee radio transmits the current bolt state to another Xbee radio connected to a PC. The data from the sensor node can then be retrieved using serial port emulator software.

It is important to note that the operation of this particular form of sensor node is very flexible. The microcontroller can be easily programmed to perform a number of different operations with the data. For example, in cases where energy concerns may not be as important as data storage, the Xbee radio can be used to transmit the entire data record. In the case of some of the experiments in this investigation, wireless power delivery was not as important, so the data records were sent from the UART on the microcontroller, to a MAX232 level converting chip, and then to the RS-232 port on the PC. The data could then be displayed using either a serial port emulator, or even be retrieved directly by Matlab. Furthermore, the AD5933 has a temperature measurement feature that can be used to track the thermal environment of the sensor node.

The current incarnation of the sensor node prototype is shown in Figure 3-4. All of the integrated circuits used in the sensor node only come in surface mount packages, so development boards were used to ease the initial prototyping stage. As a result, the sensor node appears to be rather large. In reality, the individual components used to actually make up the sensor node should be able to fit on a single printed circuit board (PCB) roughly the size of a credit card. Very few of the IO pins on the microcontroller are actually used, so signal lines between chips should not be a major consumer of board space. Furthermore, a self-imposed design constraint on this sensor node was that all of the components needed to operate from the same 3.3 voltage supply in order to allow low voltage operation, and to minimize the number of voltage references needed. The most immediate future work on the wireless sensor

node will be concerned with moving all components onto a single PCB, which should be relatively trivial.

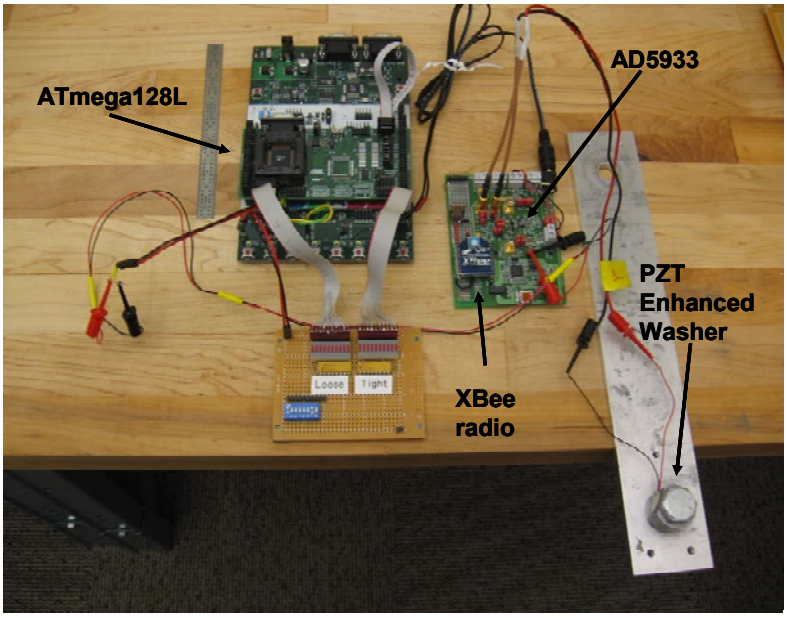

Figure 3-4: Prototype Impedance-based wireless sensor node

The PZT enhanced washer and the AD5933 have already been described in detail above. The remainder of this section will briefly summarize some of the main characteristics of the remaining sensor node components.

3.4.2 Microcontroller ATmega128L

The microcontroller's role in the sensor node is to control the operation of the impedance measurement chip, implement SHM algorithms on the impedance data, and to send damage condition information to the wireless telemetry. The ATmega128L, Figure 3-5, was selected as the microcontroller for the impedance based wireless sensor node for a number of reasons. The ATmega128L belongs to the Atmel AVR

family of 8 bit microcontrollers. The AVR microcontrollers were designed to operate at low power levels, and the instruction set is designed to allow the optimization of C code. There are a large number of different microcontrollers in the AVR family with different peripheral features and memory capabilities. The large and diverse nature of the AVR family makes them ideal for scalable applications. AVR microcontrollers feature devices such as UARTs, two wire interfaces, analog-to-digital converters (ADC), a variety of sleep modes, and some recently released AVR microcontrollers have provisions to utilize USB connections. In addition, open-source C compilers are available for AVR microcontrollers. The microcontroller in this investigation was programmed using the WinAVR open source C compiler. Numerous development boards exits for the AVR family in order to make learning how to use AVR microcontrollers easier. Furthermore, the AVR microcontrollers have a large hobbyist following. AVRfreaks.net is a very comprehensive website for AVR enthusiasts and engineers. Current AVR developments as well as a number of AVR tools are constantly updated and available for use. The AVR family was primarily selected for use as the microcontroller because of its scalability for future sensor node applications.

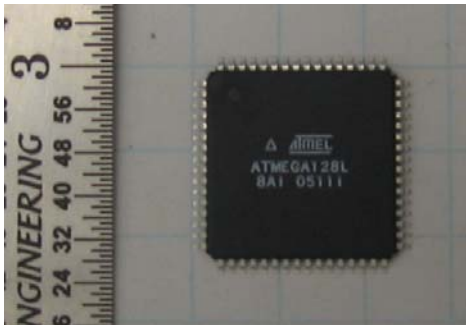

Figure 3-5: ATmega128L microcontroller

The ATmega128L is the low voltage (3.3 V) version of one of the more large microcontrollers in the AVR family. It features 128 KB of flash memory, and 4 KB of static random access memory (SRAM). In addition the ATmega128L contains dual UARTs and a TWI which are both essential for communicating with the Xbee radio and the AD5933. The UART also allows communication with the RS-232 port on a PC. Another helpful feature of the ATmega128L is that it includes an 8 MHz internal oscillator. The internal oscillator eliminates the need for an external oscillator, which would increase the size of the sensor node PCB. All measurements performed in this investigation were executed using the internal 8 MHZ oscillator. The 128 KB of flash has so far proven to be more than ample for this sensor node application. The 4 KB of SRAM is sufficient for the bolted joint preload problem utilizing the PZT enhanced washer. Most other SHM applications that require the use of memory intensive algorithms would probably call for additional memory. The possibility of adding additional SRAM, or even a USB mass storage device, is currently being explored for more general SHM applications. The ATmega128L sells for around $16.00.

3.4.3 Wireless Telemetry

Wireless telemetry was added to the sensor node in order to allow SHM data to be transmitted without the need for a costly hard-wired connection. The wireless telemetry selected for the wireless sensor node was the 2.4 GHz Xbee radio from

Maxstream, Figure 3-6**.** The Xbee radio sells for $19.00 and it comes in a variety of antenna configurations. The radio can operate from a 3.3 V supply, and consumes between 45 and 50 mA for receive and transmit (Rx/Tx) operations. Typical range for the radio is 90 m line-of-sight, and 30 m in a typical office setting. The ease of use of the Xbee radio was the main driver for its integration into the wireless sensor node. The only requirements beside the power and ground lines are the connections to the UART Rx/Tx pins. Furthermore, the radio Rx/Tx lines can be directly connected to CMOS logic levels. No level converter chip is needed as in conventional microcontroller UART-to-PC connections. The microcontroller UART can be directly connected to the radio, and the Xbee can communicate with a base station enabled PC, in a manner similar to a wired RS-232 serial connection. Transmitted data can be acquired by the PC using serial port emulation software. Since the original sensor node development, wireless telemetry radios with slightly lower current consumption have been discovered, whose use in future wireless sensor nodes is being considered.

Figure 3-6: Xbee radio for wireless telemetry

3.4.4 Wireless Sensor Node Power Requirements

The low energy availability in wireless sensor nodes mandates that the power requirements of the individual components be carefully considered. Table 3-2, shows the voltage and current requirements of the various sensor node components during both normal operation and power down mode.

Table 3-2: Sensor node voltage and current requirements

	Voltage Range (V)	Nominal Voltage (V)	Normal Current (mA)	Power-Down Current (µA)
AD5933	2.7 - 5.5	3.3	10	0.7
XBee	2.8 - 3.4	3.3	45	10
ATmega128L, 8 MHZ CLK	2.7 - 5.5	3.3	9.5	5
		Total Current	64.5	15.7

The data from Table 3-2 is used to generate the sensor node power requirements shown in Table 3-3.

Table 3-3: Sensor node power requirements

	Normal Power (mW)	Power-Down Power (µW)
AD5933	33	2.31
XBee	148.5	33
ATmega128L, 8 MHZ CLK	31.35	16.5
Total Power	212.85	51.81

The power requirements table shows that the Xbee radio is by far the greatest single power consumer in the sensor node, accounting for nearly 70% of the total power. It is important to remember however, that the radio will have a very small duty cycle. In the case of the bolted joint SHM problem, the radio only needs to transmit a couple of bytes of data to indicate either the "loose" or "tight" condition. In reality, the current consumption of the sensor node during normal operation is around 19.5 amps, and the power consumption is 64.35 mW. The power-down mode current and power consumption figures are also vitally important, especially in sensor nodes that utilize energy harvested from ambient energy. The energy harvesting device must supply more than the power-down power consumption in order to ensure a positive energy flow into the energy storage device, (Calhoun 2005). Because power harvesting solutions typically only supply on the order of tens of μW, (Calhoun 2005), the standby power requirements require careful consideration. The power-down requirements of the wireless sensor node are rather high at 51 μW relative to the power supplied by typical ambient mechanical vibration harvesting schemes. A large percentage of the power provided by the energy harvesting solution would be consumed just to keep the sensor node in power-down mode. This preliminary power analysis shows that ambient mechanical vibration energy harvesting may not be a suitable power solution for this sensor node. For this reason alternative power supply schemes, such as RF wireless energy transmission as discussed in chapter 4, are being explored.

3.5 Experimental Results with the Sensor Node

Once the impedance-based sensor node was designed and fabricated, tests could begin in order to determine its performance as a SHM sensor node. A number of structures were tested with the proposed sensor node, including the PZT enhanced washer, a portal frame structure, and a composite wing spar. In these tests, impedance measurements taken with conventional data acquisition systems were compared with measurements obtained with the sensor node.

It is important to note that the typical impedance values of the PZT sensors lie about 100 Ohms below the minimum rated impedance measurable with the AD5933. This problem has been discussed with the engineers at Analog Devices who designed the AD5933, and they indicated that the shapes of the impedance measurements would be correct, but the impedance values given to the measurements would not be correct, even if the conventional calibration procedure outlined in the data sheet were followed. These statements have been found to be more or less the case. In any event, the errors associated with the impedance values have little impact on the sensor node performance for SHM applications. Generally the algorithms used for the impedance method are only concerned with impedance measurement shape changes. For SHM purposes, the relative values of the measurements are adequate to determine the structural integrity of a bolted joint. Furthermore, the calculations required to perform the calibration procedure call for a large amount of microcontroller memory that could be used for more important purposes such as data storage. All impedance

measurements taken with either the AD5933 or the National Instruments NI PXI-1042Q data acquisition system utilize scaled values that are shown for comparison purposes only. Measurements taken with the 4294A impedance analyzer do reflect actual impedance values. For the immediate future, there is no push to improve the calibration procedure for the AD5933 at lower impedance values because of the microcontroller memory limitations for such operations. Furthermore, the procedures are for the most part unnecessary at this time, and they would consume precious wireless sensor node energy. Discussions with the engineers at Analog Devices have indicated, however, that future versions of the impedance measurement chips may have the capability to measure impedance values in the ranges normally encountered for SHM.

In all of these tests, the data measured from the sensor node is transmitted to the PC via a standard RS-232 serial cable. In normal operation sending kilobytes of data over a wireless link would generally be avoided for power consumption reasons. For these preliminary tests it was deemed unimportant to send the data wirelessly because the main concern was to evaluate the AD5933 as an impedance measurement sensor.

3.5.1 PZT enhanced washer

The first structure tested with the AD5933 impedance measurement chip was the 25.4 mm high aluminum hex PZT enhanced washer with a superglue bond as shown in Figure 3-7.

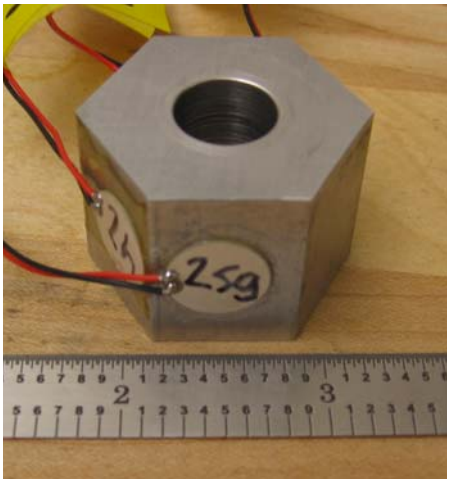

Figure 3-7: 25.4-mm, aluminum-hex PZT enhanced washer. Sensor used is indicated as "2sg"

The PZT enhanced washer was tightened to progressively higher torque values, and impedance measurements were made with both a National Instruments NI PXI-1042 data acquisition system and the AD5933 impedance measurement chip. Impedance measurements were made over the 80 to 95 kHz frequency range, where the most dominant peak resided. The resulting measurements are shown in Figure 3-8.

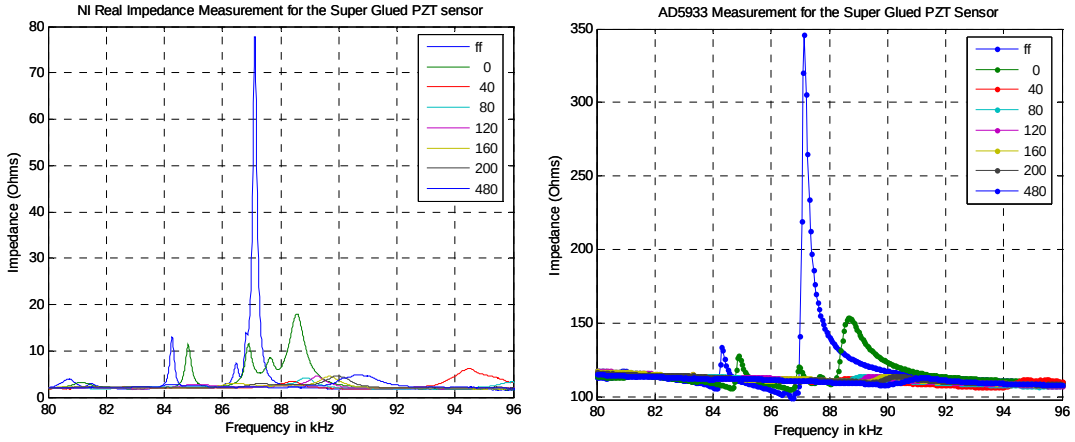

Figure 3-8: 25.4-mm aluminum hex PZT enhanced washer measurements. Impedance values have been scaled by data acquisition and are shown for comparison purposes only.

Both impedance measurements show the dominant peak very clearly in the washer's free-free condition. Furthermore, the smaller peak slightly above 84 kHz is also captured by each impedance measurement. In addition, as the preload is increased, the peak dies away in a similar manner for both impedance measurement solutions. Clearly the main dynamic behavior of the dominant peak is captured in both measurements. Furthermore, a simple peak picking algorithm would be able to determine whether or not the peak has been repressed, in order to make the decision of whether or not the bolt has come loose.

At this point, it is important to note that the AD5933 does not directly give out real and imaginary values proportional to the real and imaginary values of the impedance. In reality, by looking over the operation of the impedance chip, it is possible to see that it is actually giving out real and imaginary DFT values corresponding to the current output from the device. For this reason, it is necessary to

use the following formula to calculate the impedance measurement at any given frequency point.

$$\left|\mathrm{Im}\, pedance\right| = \frac{1}{GF * \sqrt{\mathrm{Re}\, alregister^2 + \mathrm{Im}\, aginaryregister^2}} \qquad \textbf{Equation 3-1}$$

The "GF" variable is referred to as the "Gain Factor," which is simply a calibration factor. A conventional PC has no problem performing this calculation for 512 points, but a microcontroller with only a couple kilobytes of SRAM can quickly exceed the memory capacity with such calculations. Furthermore, the square root operation requires the use of high memory, (8 byte), double precision floating-point values. A simple calculation shows that storing 512 points of 8 byte data consumes all 4096 bytes of SRAM available in the ATmega128L. The damage detection algorithm still needs to be executed, so either very creative memory allocation schemes will need to be implemented, or fewer points will need to be measured. The sensor node used in this investigation makes use of both approaches. Two bytes are necessary to store each real and imaginary data point. The first thought that comes to mind, is that maybe it is not necessary to store both the real and imaginary data points. What if only the real data were saved? The next realization is that it is probably not necessary to invert or square the real data points. It is proposed, that the real register output from the AD5933 may be sufficient to determine whether or not the bolt has come loose.

In order to test this hypothesis, an experiment was set up using the 19mm steel PZT enhanced washer, Figure 3-9.

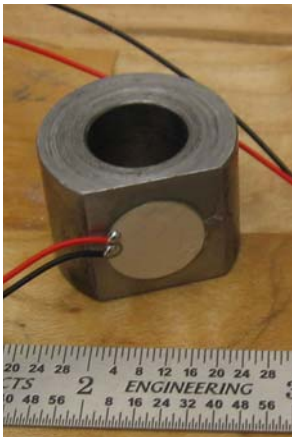

Figure 3-9: 19-mm, steel PZT enhanced washer

The bolt was tightened to increasing levels of toque. At each torque level, 5, 512 point measurements were taken with the AD5933 over the frequency range of 84 to 86.5 kHz. The resulting real register measurements are shown in Figure 3-10. In this plot, dips are clearly present in the real register values. These dips correlate with the peaks in the impedance measurements. In addition, these dips display dynamics behavior with varying torque very similar to the behavior of the peaks in the impedance measurements. At very low torque levels, the dips are very pronounced. As the toque levels increase very slightly (less than 40 in*lb) the dips shift to slightly higher frequencies (due to load-induced stiffening). At torque levels above 40 in*lbs the dip in the measurement disappears completely. A simple minimum value detection algorithm would be able to determine whether or not the dip has been repressed. In the case the dip had not been repressed, the damage detection algorithm would be able to indicate the bolt had come loose. Figure 3-11 shows the results of running a minimum value detector on the real register values.

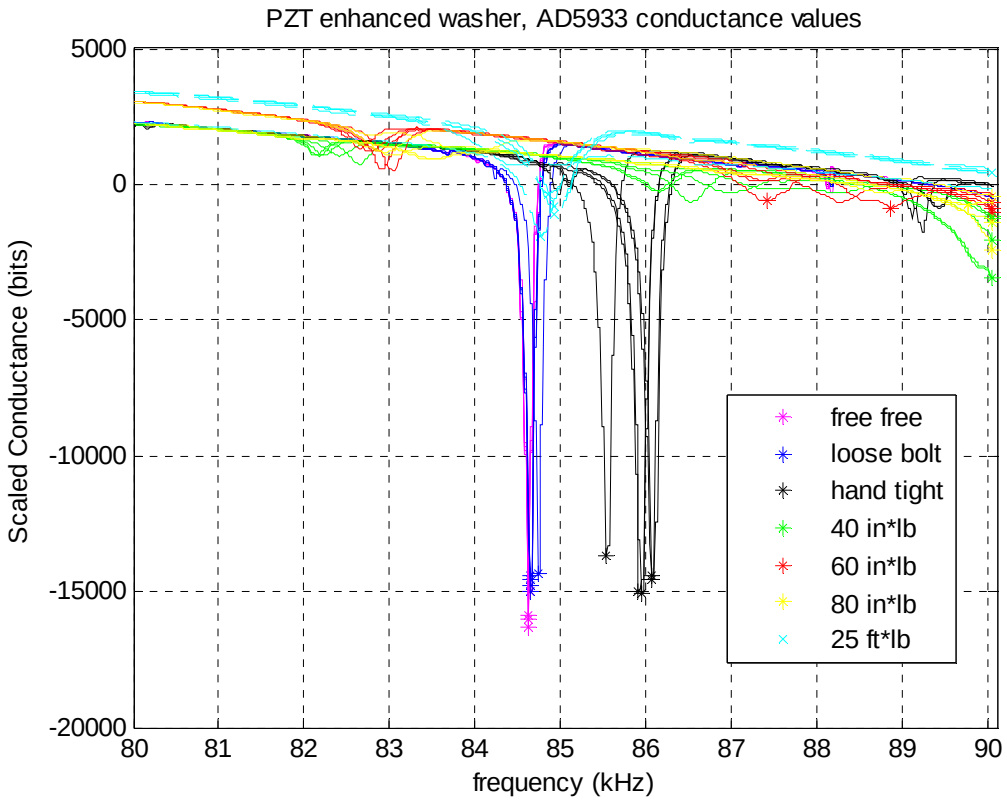

Figure 3-10: AD5933 real register values. Conductance values have been scaled by data acquisition and are shown for comparison purposes only.

The minimum value damage detection algorithm obtains values of between about -14000 to -16000 for the free-free case, in the hand tight case range. As soon as 40 in-lb of torque or more is applied to the bolted joint, the damage detection index quickly jumps to the 2000 to -2000 range. Clearly the easy-to-implement, low memory, minimum value detector shows very pronounced changes between very low torque levels, and appreciable torque levels. Setting a threshold anywhere between -4000 and -12000 would be sufficient for determining whether or not the bolt has come loose. The distinct changes in the minimum value damage index make the possibility of false-positives and false negatives very remote. In practice, an algorithm very

similar to the real register minimum value detector has been implemented using this washer and the sensor node. The algorithm deployed in the sensor node is given as:

$$DamageIndex = \min\left(\mathrm{Re}\,alregister^2 + \mathrm{Im}\,agregister^2\right) \qquad \textbf{Equation 3-2}$$

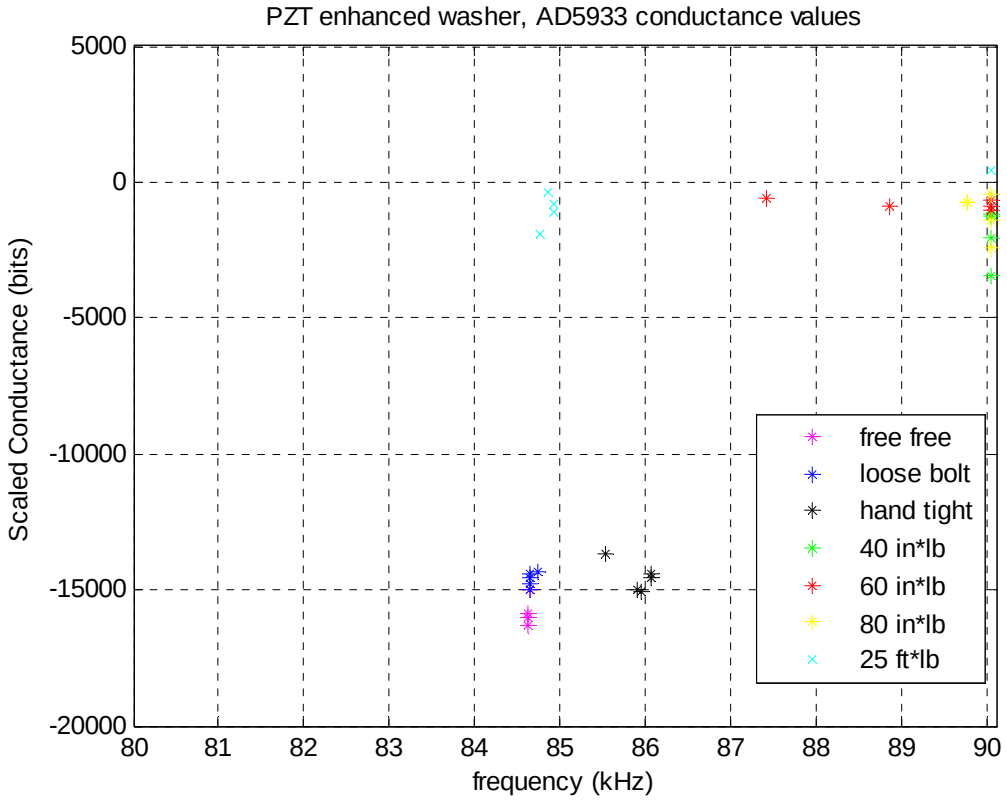

Figure 3-11: AD5933 real register minimum values. Values have been scaled by data acquisition and are shown for comparison purposes only.

The magnitude squared of the real and imaginary registers was used in order to avoid complications involved with negative and positive values. The sensor node programmed with this algorithm was deployed at the International Modal Analysis Conference on February 21 through 22, 2006 in the UCSD/LANL Engineering Institute technology demonstration booth. Throughout the duration of the exhibition,

the operation of the wireless sensor node was demonstrated to numerous conference attendees, and not a single false-positive or false-negative was reported. It must be admitted, that even though the sensor node performed very well during the conference, right before the demonstration, it was discovered that occasionally the sensor node would indicate a tight condition when the bolt had actually come loose. The problem was quickly discovered to be that the radius under the head of the ½-13 bolt was slightly larger than the chamfer at the 12mm clearance hole in the washer. In some cases the bolt was effectively sticking to the washer, which was enough to make the peak in the measurement remain repressed. The problem was quickly solved by using a deburring tool to slightly increase the chamfer in the PZT enhanced washer. No failures have been reported since the chamfer adjustment. Despite the ease with which this problem was solved, new questions remain. Will the sensor node be unable to indicate whether or not a bolt has come loose in environments where the washer and bolt might develop some amount of corrosion and slightly fuse together? What effects can occur in environments where mud can build up on the top of the washer? Will the weight of the mud be enough to suppress the peak in the washer? These are valid concerns that will be addressed in more advanced PZT enhanced washer designs. The preliminary tests have indicated however, that a generalized baseline sensor coupled with the low cost wireless active sensor node is a realistic structural health monitoring solution.

3.5.2 Portal frame

Once the AD5933 had displayed its ability to distinguish loose from tight bolts with the PZT enhanced washer, the next step was to investigate the ability of the AD5933 to make impedance measurements on slightly more complicated structures. The first structure that was investigated was a portal frame structure as shown in Figure 3-12. The portal frame structure is composed of 3, 50-mm X 6-mm aluminum beams, held together by ½-13 bolts, and steel angle iron connections. The base is a 610-mm X 153-mm X 12-mm plate of aluminum. The upper aluminum beam measures 553-mm long, and the side aluminum beams are 310 mm high. A PZT patch measuring 23-mm X 18-mm, as indicated by "PZT" on the upper left side of the top beam in Figure 3-12, was used as a sensor.

The focus of the portal frame experiment is to determine the suitability of the impedance method to detect changes in the preload of bolts 1 through 4. Furthermore, the performance of the AD5933 as compared to the Agilent 4294A impedance analyzer is under study. For this reason, conductance measurements (real portion of the admittance), were used instead of impedance measurements, because the conductance requires fewer microcontroller calculations. First 10 baseline conductance measurements were taken from the PZT patch with both the AD5933, as well as the Agilent 4294A over the 50 to 54 kHz. In the baseline cases all of the ½-13 bolts were in the tightened condition. For the first damaged case, bolt 1 was completely loosened, and two measurements were taken with the AD5933 and 4294A each. After the measurements were complete, bolt 2 was also totally loosened and 2

measurements were taken with both impedance analyzers. A similar procedure was then carried out for bolts 3 and 4. The conductance measurements of the PZT patch for both the 4294A and the AD5933 are shown in Figure 3-13.

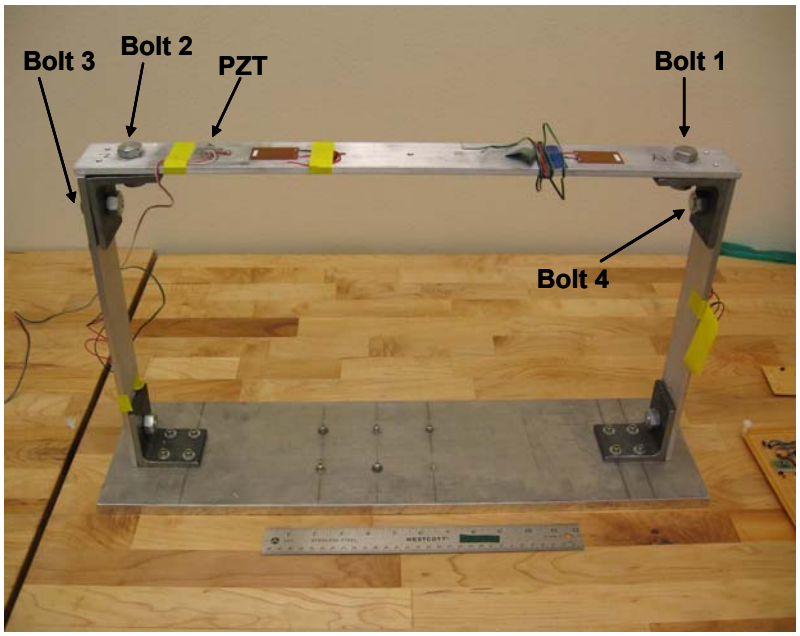

Figure 3-12: Portal frame structure

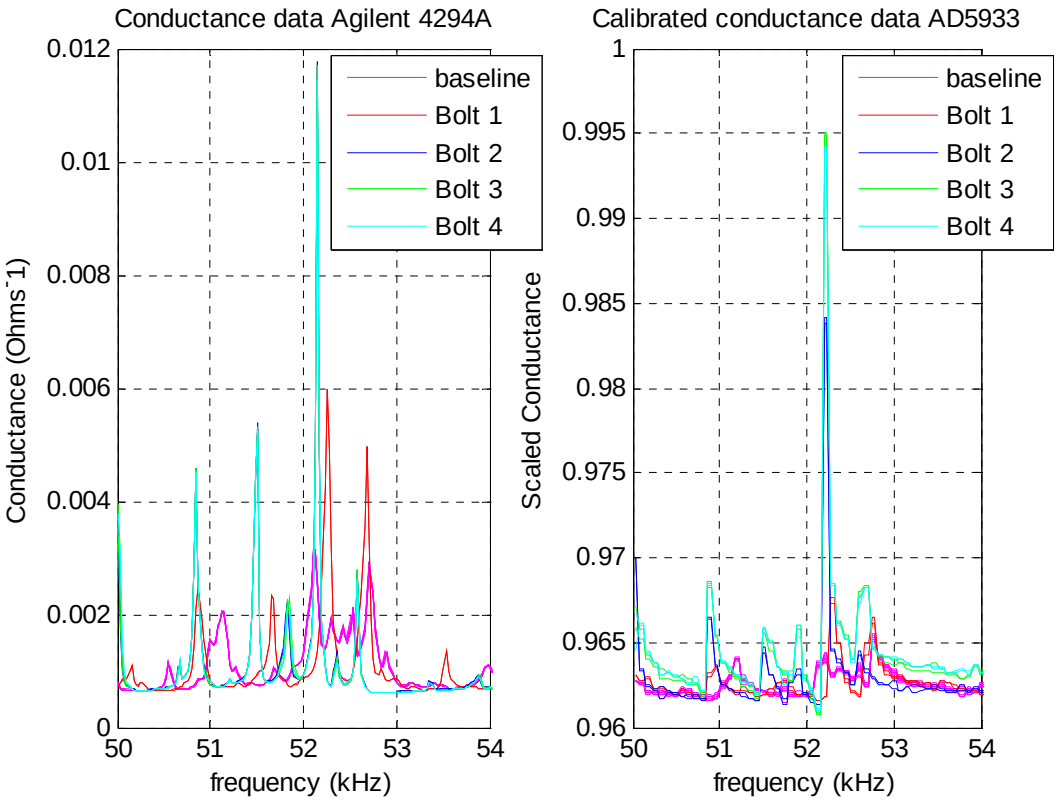

Figure 3-13: Portal frame conductance measurements. Magenta: baseline: all bolts tight, Red: bolt 1 loosened, Blue: bolt 2 loosened, Green: bolt 3 loosened, Cyan: bolt 4 loosened.

The conductance plots in Figure 3-13 display a number of noteworthy traits. First of all, the conductance measurements, at each damage case, for either impedance measurement device are very repeatable. All 10 of the baseline measurements basically lie on top of one another. In the cases where progressively more bolts lost preload, two measurements where taken with each impedance measurement device. The curves in Figure 3-13 at any given damage level show only small deviations from each other, and in most cases they are totally undistinguishable. Another interesting trend in these measurements is that the conductance peaks tend to increase in magnitude as the bolts in the structure lose preload. Basically what is occurring is that

as the bolts loose preload, the PZT are able to have a greater effect on the dynamics of the structure. Greater structural responses are possible for the same amount of source excitation. Furthermore, the conductance peak values also display a saturation point. The saturation point refers to the situation when the structure is basically responding as much as it can from the PZT patch excitation. The best indicator of the existence of a saturation point is the conductance measurement of the dominant peak slightly above 52 kHz. The conductance value of the peak around 52 kHz increases from the baseline measurement when the first bolt is loosened. The peak also increases in magnitude when the second bolt is loosened, as well as when the third bolt is loosened. The value and frequency of the peak near 52 kHz does not change when the fourth bolt is loosened. The peak magnitude and frequency are nearly identical. In fact, the conductance measurement over the 50 to 54 kHz bandwidth is nearly identical for the case where up to the third bolt is loosened, and the case where up to the fourth bolt is loosened. Essentially what is occurring here is that as far as the dynamics in the 50 to 54 kHz range are concerned, the top aluminum beam in the portal frame is as loose as it can possibly be when the third bolt is loosened. Alternatively, the PZT is essentially decoupled from any dynamics associated with the fourth bolt once the third bolt is loosened.

One very important observation associated with both sets of impedance measurements in Figure 3-13, is that in general as more bolts are loosened, and the damage level in the structure increases, the magnitude of the conductance measurements increase. This behavior is especially pronounced at the dominant peak

near 52 kHz. The increase in conductance measurement with increasing damage is important, because it indicates that it may be possible to use a very simple algorithm to compare changes from the baseline measurement in order to show which bolts have lost preload. One possible scenario in a bolted joint structure would be that every beam in the structure would have a single PZT patch. Conductance measurements could be taken periodically from each patch, and as preload is progressively lost in the bolts, certain conductance measurements would reach their saturation value before others. By analyzing which impedance measurements where at their saturation value, it would be possible to determine which bolted joints had come loose, and which beams had essentially become uncoupled from the structure.

The last characteristic of the conductance measurements that needs to be discussed is the comparison of the measurements associated with the AD5933, and the measurements taken with the Agilent 4294A. The first observation is that the relative magnitudes of the peaks in the two measurements are fairly different. For example, in the 4294A conductance measurement with 3 bolts loosened, the peak slightly below 51 kHz is about 1/3 the height of the dominant peak located slightly above 52 kHz. The corresponding peaks in the AD5933 measurement have a height ratio of 1/5. In general the conductance measurements of the less dominant peaks recorded with the AD5933, are smaller in relative magnitude than those measured with the AD5933. Despite the discrepancy in relative magnitude, the frequency values associated with the peaks are very similar. In addition, all of the peaks measured by the 4294A are also captured by the AD5933. Future work on designing algorithms for detecting

damage in bolted joint structures using PZT mounting schemes similar to those used in this experiment will require taking into account the behavior of the conductance measurements associated with the AD5933. In addition, it is possible that the discrepancies in the relative magnitudes of the peaks measured by the AD5933 may be associated with setting the various gains and registers in the AD5933 to inappropriate values. It is not entirely clear at this point whether the AD5933 is always being used in the manner intended by the designers. Future investigations and discussions with the designer of the AD5933 will be concerned with ensuring that user errors are not stifling the impedance measurement performance available from the AD5933.

Conductance measurements from a PZT patch have been recorded from a portal frame structure, with a progressively increasing number of loose bolts. The conductance measurements have shown that as more bolts loose preload, the magnitude of the peaks in the conductance measurement over 50 to 54 kHz increase in magnitude. The conductance measurements made with the Agilent 4294A impedance analyzer and the AD5933 both capture the same peaks. The relative magnitudes of the peaks are not the same however. The non-dominant peaks in the AD5933 measurements appear to be disproportionably small compared to the dominant peak. Damage detection algorithms will need to be designed to take into account this form of discrepancy. Future work will be concerned with trying to improve the quality of the AD5933 measurements in the case of structures with construction similar to that found in the portal frame structure. In any event, the measurements obtained with the

AD5933 do show promise for SHM applications given the cost and size differential between the AD5933 and the Agilent 4294A impedance analyzer.

3.5.3 Composite Wing Spar Assembly

In order to test the applicability of the sensor node to aerospace structures, a number of admittance measurements were made on a section of a simulated composite wing spar, Figure 3-14**.** The composite wing spar assembly is made up of a 330-mm X 330-mm X 1-mm carbon fiber composite wing skin with a [0/±45/90] lay-up. The wing skin is then bonded to a hollow square spar measuring 50 mm on each side with a wall thickness of 6 mm. Damage was introduced into this structure by manually applying a peeling load to the corner of the skin-to-spar surface nearest to the PZT sensor used for measurements. Photos of the four damage cases can be seen in Figure 3-15. Admittance measurements were made with both the Agilent 4294A impedance analyzer, and the AD5933 for comparison purposes. First ten baseline measurements of the undamaged case were made with both measurement devices. Next, disbond damage in the adhesive skin-to-spar joint damage was progressively introduced into the structure. At each damage level two measurements were made with each impedance measurement device. The resulting admittance magnitude measurements can be found in Figure 3-16 through Figure 3-19.

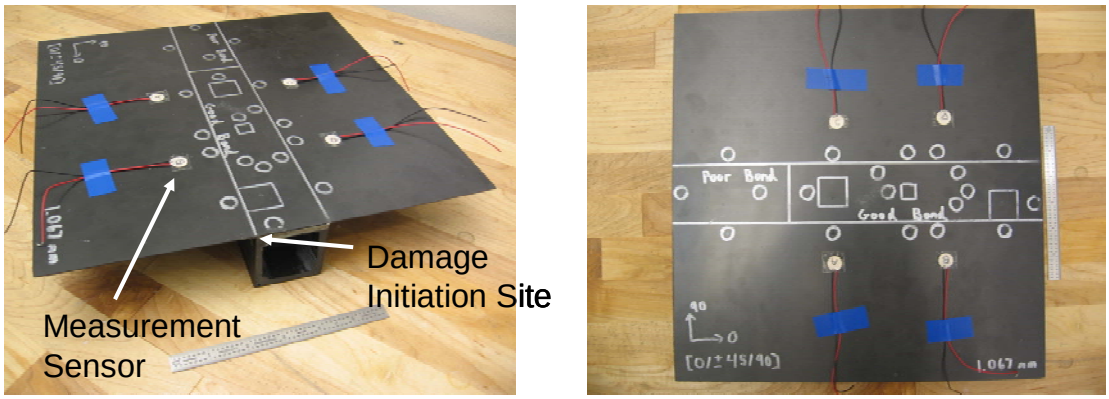

Figure 3-14: Composite wing spar assembly

Figure 3-15: Damage progression in composite wing spar assembly. Note the increasing disbond between the wing skin and the spar.

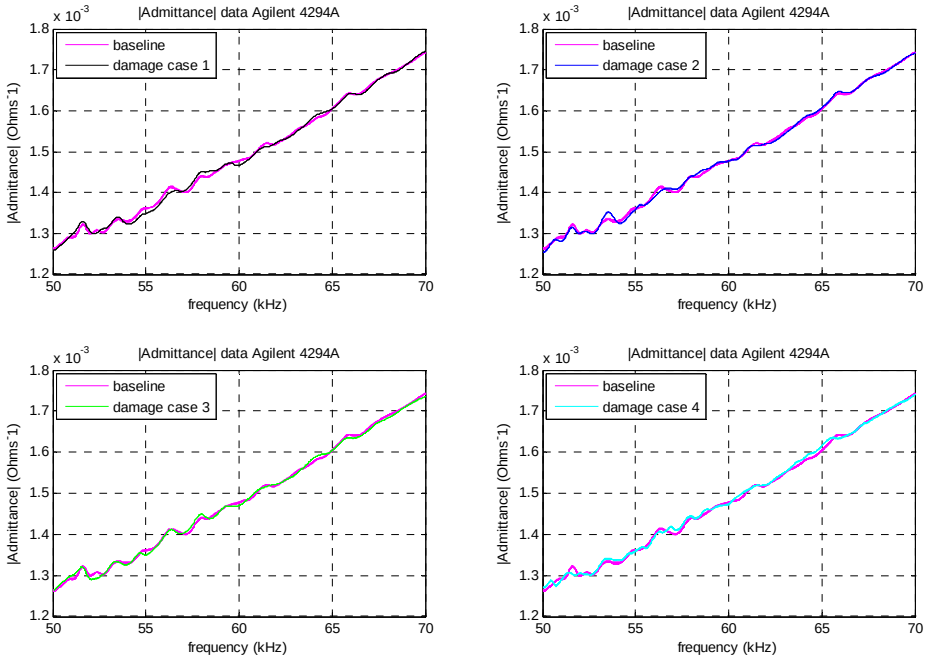

Figure 3-16: Agilent 4294A admittance measurements for the composite wing spar assembly.

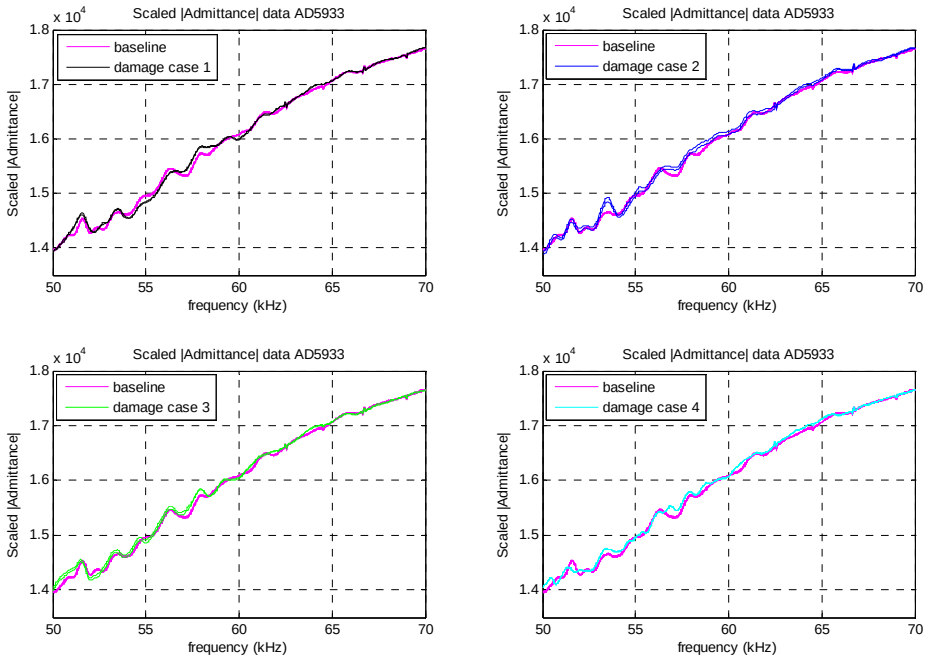

Figure 3-17: AD5933 admittance measurements for the composite wing spar assembly.

The magnitude of the admittance measurements between 50 and 70 KHz seem very similar in nature. The AD5933 seems to do a very good job of capturing all of the small peaks in the admittance magnitude measurement. Further insight can be obtained by zooming into the 50 to 60 kHz range as shown in Figure 3-18 and Figure 3-19.

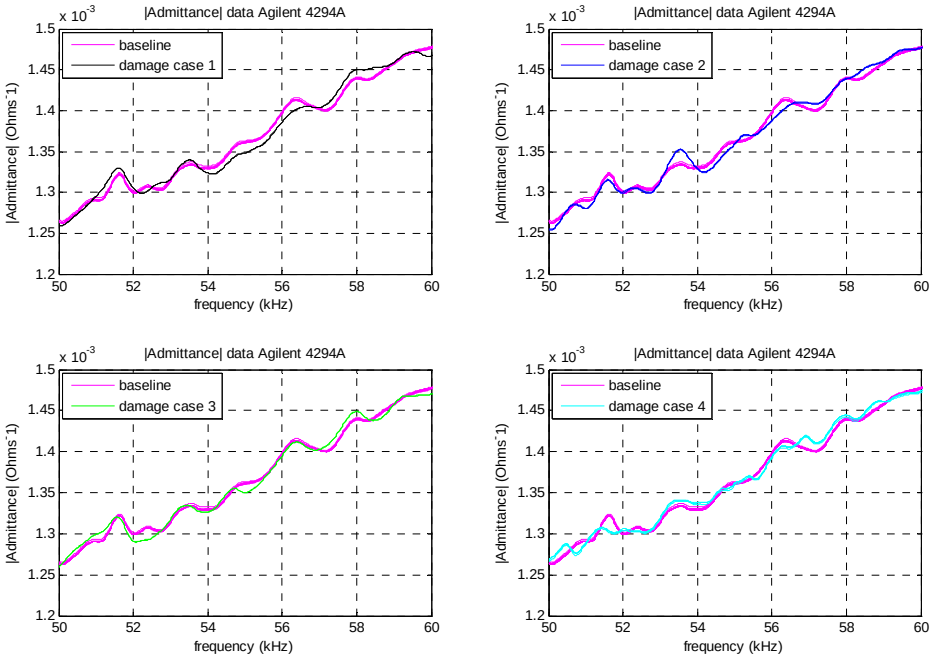

Figure 3-18: Agilent 4294A admittance measurements for the composite wing spar assembly

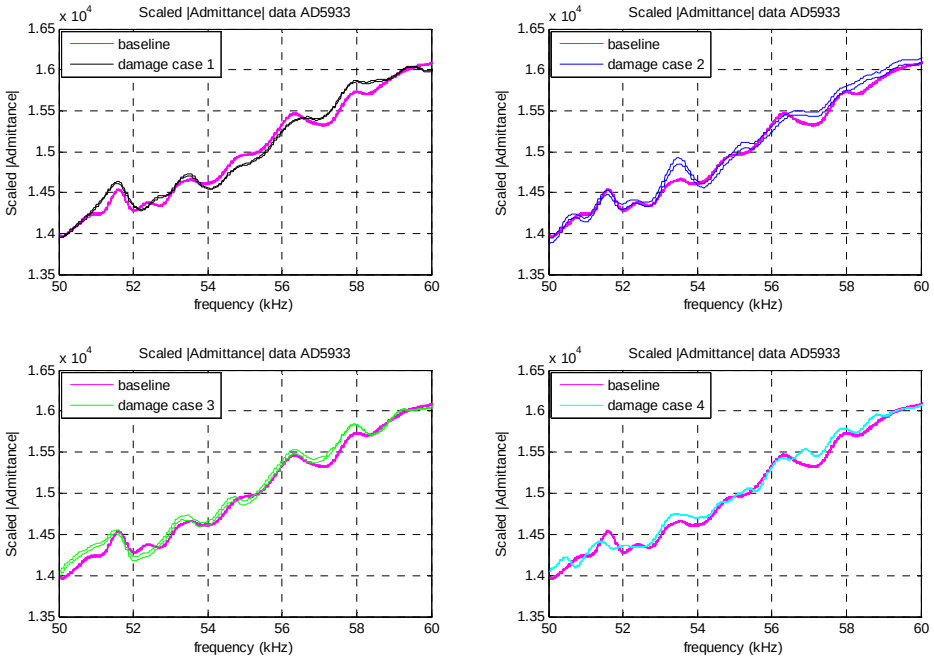

Figure 3-19: AD5933 admittance measurements for the composite wing spar assembly

The zoomed in admittance magnitude measurement shows more clearly how well the AD5933 captures the dynamics of the composite wing spar assembly. The results are fairly impressive considering that the AD5933 costs $6.95 while an Agilent 4294A costs $41,000. Furthermore, the AD5933 weighs significantly less, which will be a prime concern for weight-critical aerospace applications.

Now that low cost, low weight sensor nodes have been shown to be able to produce relatively faithful impedance measurements, the next step is to develop algorithms to quantify the amount of disbond damage in the composite wing spar assembly. It is very likely that these algorithms will require more memory than is currently available in the wireless sensor node. Future research will be directed toward investigating the integration of USB mass storage devices and additional

SRAM into the sensor node for accommodating the data storage requirements of these algorithms. On the plus side, if these sensor nodes are integrated into an aerospace structure, there is a higher likelihood that provisions can be made to provide a fairly constant source of power to the sensor node. The constant power source will alleviate many of the concerns associated with field-deployed wireless sensor nodes.

3.6 Sensor Node Summary

This chapter has been concerned with the design and fabrication of an active wireless sensor node based off recently developed impedance measurement technology. The sensor node utilizes the AD5933 impedance measurement chip, an Atmel ATmega128L microcontroller, and an Xbee 2.4 GHz radio from MaxStream. The power supply characteristics of the sensor node have been evaluated for both normal operation, and during power down mode. The energy requirement analysis has indicated that mechanical vibration-based power harvesting may not supply sufficient power for the operation of this sensor node, so alternate power supplies need to be evaluated.

The impedance based sensor node performance has been compared against an Agilent 4294A impedance analyzer. Both impedance measurement solutions were used to measure the dynamics of the PZT enhanced washer, a portal frame structure, and a composite wing spar assembly. The AD5933 has demonstrated the capability of making active dynamic measurements in the tens of kilohertz range that are

comparable in shape to those obtained with the Agilent 4294A impedance analyzer. The AD5933 has shown promise as an active sensor node for SHM applications.

Chapter 4 Wireless RF Power Delivery

4.1 Overview

This chapter describes the experimental investigation of wireless Radio Frequency (RF) energy transfer systems. The goal of this study is to develop SHM sensing systems that can be permanently embedded in the host structure and do not require an on-board power sources. With this approach, the required energy will be periodically delivered as needed to operate the sensor node, as opposed to being harvested from ambient vibrations. A feasibility study using X-band signals to wirelessly deliver electrical energy to operate a part of impedance sensing node is presented.

In order to show that the X-band rectifying-antenna or rectenna, concept is suitable for wireless sensor networks, it is necessary to evaluate two main criteria. First, will the rectenna supply ample power for the sensor node's required duty cycle, and "sleep mode" energy demands? Secondly, can the rectenna supply sufficient voltage for the operation of the sensor node electronics? In order for the rectenna to be successful, it must be able to charge a capacitor or a battery to a voltage of 3.3 volts, which is the maximum operating voltage of the 2.4 GHz radio telemetry that will be used in the sensor nodes. Rectenna performance will be evaluated based on how quickly the rectenna can supply the required voltage, and on how many receive/transmit (Rx/Tx) operations can be successfully completed. Both the power

and voltage requirements must be met in order for the rectenna to be a suitable substitute for conventional batteries in sensor node power supplies.

In order to investigate the feasibility of wireless power transfer for sensor node operations, a proof of concept experiment was set up to test the ability of wirelessly delivered energy to power a 2.4 GHz wireless telemetry system. The X-band at 10 GHz was chosen as the RF energy propagation frequency in order to facilitate the design of small antennas with high gain. A layout of the RF power delivery system is given in Figure 4-1.

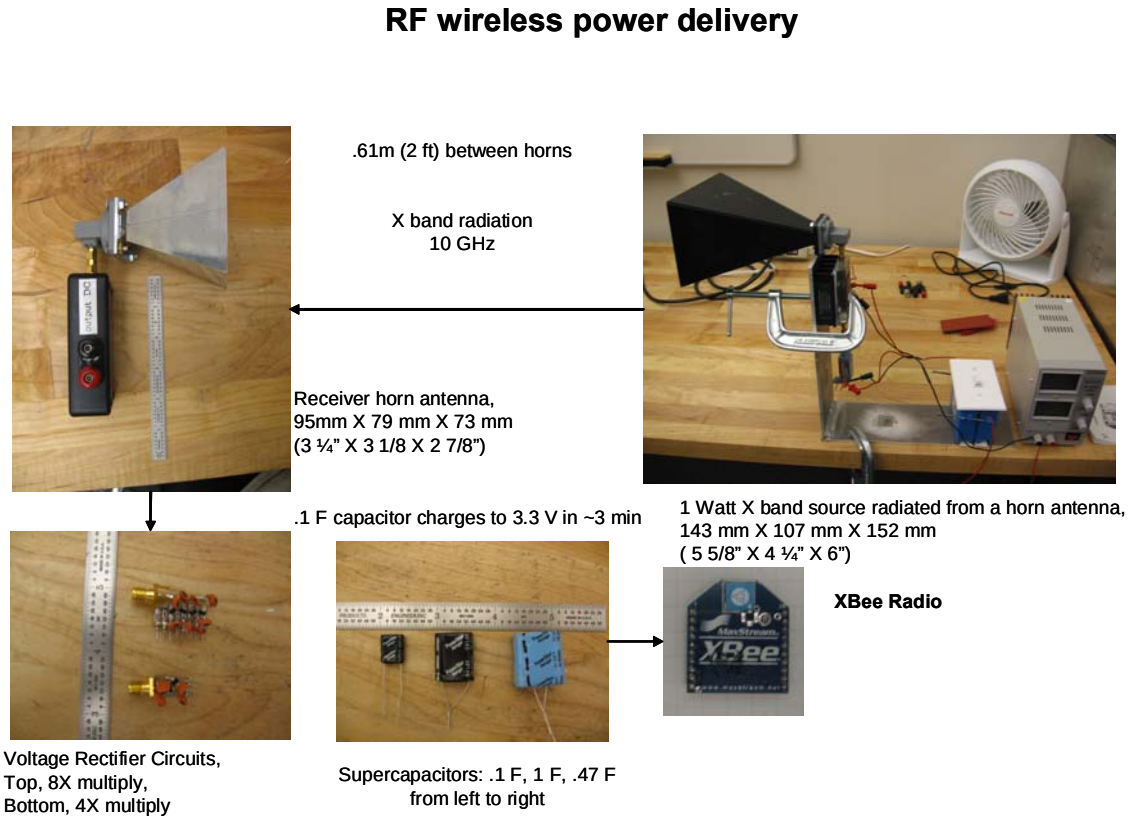

Figure 4-1: RF power delivery test setup

In this setup, 1 W of X-band radiation is transmitted from a horn antenna over a distance of .6 m. At the receiving end, a rectenna is constructed from a horn antenna and an eight stage voltage multiplication circuit. The DC voltage from the recetenna is used to charge up a .1 F supercapacitor. Once a sufficient amount of voltage has built up in the supercapacitor, the stored energy is used to power a MaxStream Xbee radio. The purpose of this experiment is to find out how many Receive/Transmit (Rx/Tx) operations are possible with the energy stored in the supercapacitor when charged to 3.3 V.

4.2 RF power delivery components

In order to ensure that the rectenna meets the voltage and current requirements of the sensor node, it is necessary to put careful thought into the design and construction of the various components that make up the rectenna. This chapter will discuss the rational behind the component choices and designs implemented in the investigation.

4.2.1 RF power source

The RF power source used in this investigation is a Narda X-band source which outputs 15 dBm of power at 10 GHz, Figure 4-2. Where power in dBm is given by:

$$Power(dBm) = 10 * \log_{10}\left(\frac{Power(mW)}{1mW}\right)$$ **Equation 4-1**

The transmitted power goal is 1W, which is the maximum power allowable to stay below the 10 mW/cm^2 energy density restriction imposed by Los Alamos National Labs (LANL), LIR (402-400-02.0) for personal safety reasons. A 25 dB gain amplifier was available for use, but directly connecting the 15 dBm X-band source to the amplifier would result in 40 dBm of power, which exceeds the LANL safety restrictions. Furthermore, 40 dBm of power would saturate the amplifier, and would have a high probability of damaging it. A 10 dB attenuator was placed directly after the X-band source in order to bring the output down to 5 dBm. When the 5 dBm signal is sent to the amplifier, the resulting signal is 30 dBm, or 1W, as desired. The 1W output from the amplifier is within the safe operating range of the amplifier, and meets the safety requirements for microwave transmission at LANL.

4.2.2 Horn Antennas

Vertically polarized horn antennas were used for both the transmitter antenna and the rectenna receiver. The 20 dB of gain provided by the horn antenna made it ideal for use as the transmitter. By using a high gain antenna the microwave energy could be better directed into the rectenna, as opposed to being scattered throughout the environment. At the rectenna end, the horn antenna was used primarily for reasons of convenience. Ideally, a rectenna would lack directivity in order that it might be able to

have as large an effective aperture as possible (Brown, 1984). Conventional rectennas are usually made of an array of half-wave dipole antennas in order to reduce directivity, but because of the time constraints it was not feasible to acquire such an array. A horn antenna was used because of its small size and availability. In order to ensure that the horn antennas successfully transmitted the largest amount of power possible, the horn antennas waveguides were lined up as closely as possible with a tape measure, and similar polarization of the two antennas was ensured.

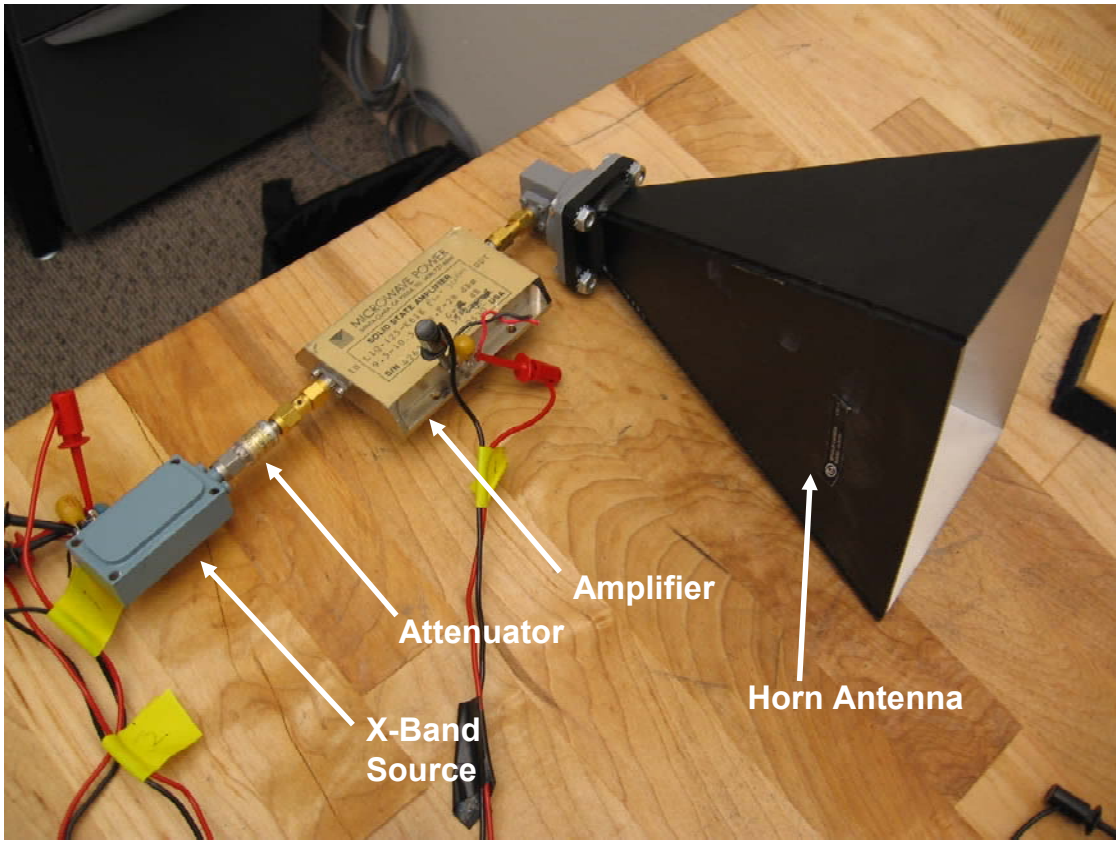

Figure 4-2: X-band source, 10 dB attenuator, 25 dB amplifier, and transmitter horn Antenna

4.2.3 Rectification Circuit

Conventional rectennas usually contain an array of diodes for every half-wave dipole element on the rectenna. There are a number of different rectification schemes that are used, but oftentimes a half-wave rectifier is used for reasons of simplicity, (Brown, 1984). The DC output of all the diodes in the array are combined in order to obtain the required voltage. However, the current investigation does not use an array of dipole antennas, so other means would be necessary for obtaining the required voltage. A voltage full-wave 8X multiplying circuit was selected as the rectifier. The design was based on the full wave quadrupler presented by Voltage Multipliers Inc. The schematic of the voltage rectifier is shown in Figure 4-3. All of the capacitors in the circuit were chosen to be 4.7 pF, and all of the diodes are MACOM X-Band Schottky Diodes, p/n MA4E2054B in the series pair configuration.

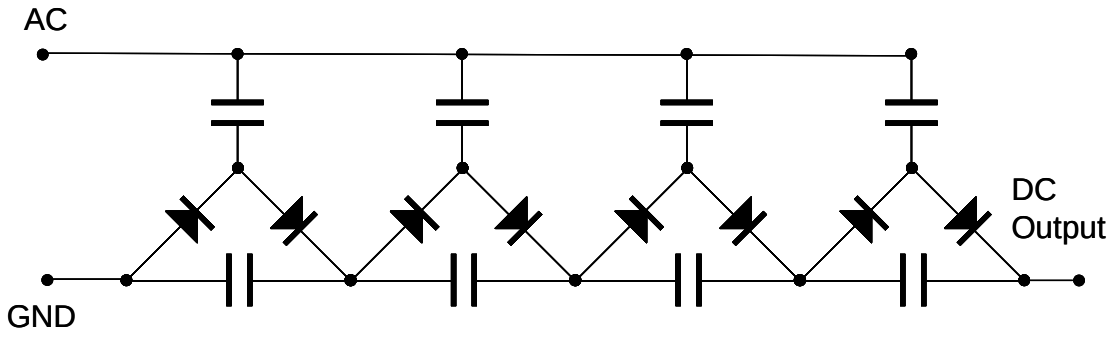

Figure 4-3: Voltage 8X multiplier Circuit Schematic

The final implementation of the rectifier is shown in Figure 4-4. The circuit was soldered on a SurfBoard, surface mount device prototype system. A male SMA connector was attached to the board to make the connection to the horn antenna

straightforward. The DIP pins on the SurfBoard facilitated the connection of the ground and DC output to the supercapacitor for long term energy storage.

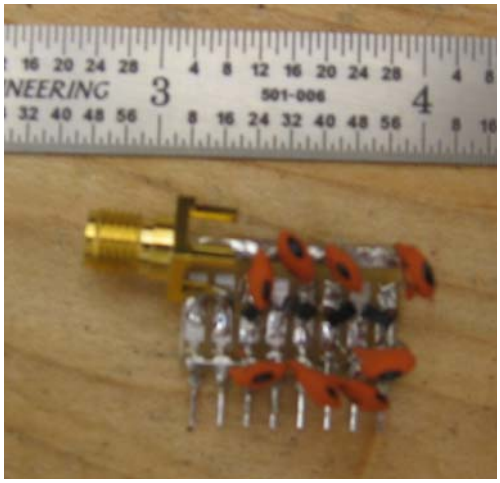

Figure 4-4: 8X Voltage Rectifier

4.2.4 Supercapacitors

A supercapacitor was chosen for storing the microwave energy received by the rectenna. Supercapacitors look similar in both shape and size to a conventional electrolytic capacitor, but the difference is that supercapacitors can have much higher capacitance values, Figure 4-5. A .1 F PowerStor Aerogel Supercapacitor from Cooper Bussmann was used in this experiment. This particular type of supercapacitor utilizes carbon Aerogel foam to obtain a very low equivalent series resistance (ESR), which helps minimize resistive losses. This form of supercapacitor is typically used for memory backup, and pulsed power applications.

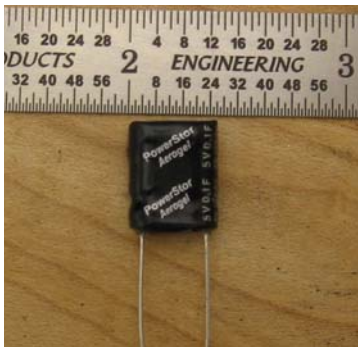

Figure 4-5: Aerogel .1 F supercapacitor rated for 5V

Supercapacitors have a number of advantages over batteries for wireless sensor networks. A battery typically operates between -20 to 60°C while a supercapacitor can operate from -40 to 70°C, Juzkow (2001). Furthermore, some sensor nodes might contain an actuator with high current requirements. A supercapacitor is much more tolerant of high current demands than a battery. Perhaps most importantly however, is that a supercapacitor can have more than 300,000 charge-discharge cycles, while a battery typically only has 300-1000 charge-discharge cycles (Juzkow, 2001). A long term sensor network will require energy storage components capable of surviving a large number of charge-discharge cycles. In this investigation, the ability of the supercapacitor to provide power to the Xbee radio will be evaluated.

4.3 Energy Transfer Performance

4.3.1 Analytical evaluation of energy transfer performance

The behavior of the X-band RF power delivery system can be described by the one-way radar equation for power incident on a target (Lee, 2004):

$$P_r = \frac{P_t G_t A_e}{4\pi R^2}$$ **Equation 4-2**

P_r is the peak power received at the input, P_t is the transmitted power, G_t is the gain of the transmitter, A_e is the effective area of the receiver antenna and R is the distance between the receiver and the antenna. In this experiment a horn antenna is being used for the receiver antenna, so the effective aperture area of the receiver antenna can be estimated by the largest cross sectional area of the horn.

$$A_{e\,\mathrm{Re}ciever} = .095m * .079m = .007505m^2$$ **Equation 4-3**

The gain of the transmitting antenna is given by the relationship:

$$G_T = \frac{4\pi * A_{eTransmitter}}{\lambda^2} = \frac{4\pi * (.143m * .107m)}{\left(\frac{3*10^8 m/s}{10*10^9 Hz}\right)^2} = 213$$ **Equation 4-4**

Where λ is the wavelength of the transmitted electromagnetic wave. Roger Bracht, the group radar engineer for Engineering Sciences Applications-Weapons Response, at Los Alamos National Labs, suggested the use of fifty percent antenna efficiency for initial calculations. The resulting G_t is then 106.5 which is approximately 20 dB. The power incident on the receiving antenna for 1W of transmitted power over a distance of .61m is given by:

$$P_r = \frac{P_t G_t A_e}{4\pi R^2} = \frac{1W * 106.5 * .007505m^2 * .5}{4\pi(.61m)^2} = 85mW$$ **Equation 4-5**

Assuming 50% efficiency for the receiving and transmitting antennas leads to a theoretical value of 85 mW delivered to the receiving antenna. The actual amount of energy can be lower depending on losses in the detector, antenna impedance

mismatches, polarization mismatches, and multi-path effects that might lead to destructive interference.

4.3.2 Experimental Evaluation of RF power delivery performance

Once the components for the X-band wireless power delivery system were designed and built, the ability of the rectenna to provide energy to a sensor node component could be evaluated. The Xbee radio was connected to the supercapacitor through a switch. The horn antennas were placed .61 m apart, and were lined up to ensure similar polarizations. A Tektronix oscilloscope was placed across the terminals of the .1F supercapacitor in order to monitor the charge/discharge voltage of the capacitor. The first test would be to monitor the supercapacitor's voltage vs time, as power was transmitted by the X-band source. Figure 4-6 shows the results of this test as the supercapacitor charges from 0 to 5 V.

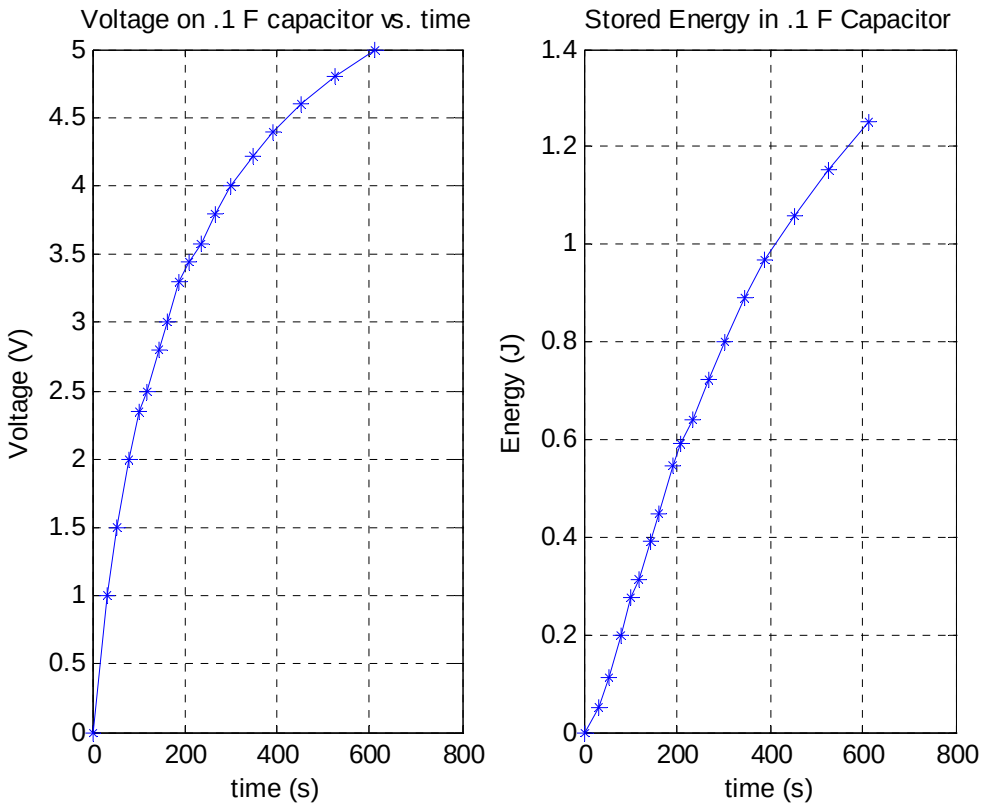

Figure 4-6: Voltage and energy storage across .1 F supercapacitor as X-band source transmits power.

The Xbee radio operates on 3.3V CMOS levels, so the voltage across the radio needs to be between 3.3 and 2.8 volts for proper operation. Clearly the X-band source is capable of delivering the required voltage levels. The supercapacitor is able to achieve 3.3 V in 200s, or a little more than three minutes. By considering the energy vs. time plot it is possible to estimate the average power that is being delivered to the supercapacitor. The energy stored in the supercapacitor is given by:

$$E = \frac{1}{2} * C * V^2$$ **Equation 4-6**

Where “E” is the energy stored in the capacitor, “C” is the capacitance of the capacitor, and “V” is the voltage across the capacitor. The energy vs. time plot is fairly linear over the first 400 seconds, so by measuring the slope of this line, the power can be estimated.

$$P = \frac{\Delta E}{\Delta t} \approx \frac{1J}{400s} = 2.5mW$$ **Equation 4-7**

Where “P” is the power “ΔE” is the change in energy, and “Δt” is the time interval under consideration. 2.5 mW is substantially less than the 85 mW estimated by the one way radar equation for power incident on a target. Possible reasons for the power discrepancy include errors in the efficiency estimate of the antennas, electromagnetic reflections off the walls causing destructive interference, and undoubtedly there is an impedance mismatch between the horns. Another possible loss mechanism is the SurfBoard used for constructing the rectifier. This board is made from an epoxy-fiberglass composite. Microwave circuits are generally constructed on Teflon circuit boards in order to reduce losses through the dielectric board material. In any event, even with the losses, the preliminary rectenna was able to supply the required voltage. The next version of the rectenna will feature an impedance matching network and a Teflon circuit board in order to take advantage of the power that may still be available from the transmitter.

Next it is necessary to see how many Rx/Tx operations are possible with the 0.54 J stored in the capacitor at 3.3 V. In order to test the Rx/Tx capabilites of the Xbee radio when powered by the supercapacitor, it was necessary to utilize the range test software that comes standard with the radio development kit. The range test

software basically transmits a continuous stream of data from a base station radio connected to a PC. The base station data is received by the Xbee radio connected to the supercapacitor. A jumper wire connected between the Rx and Tx lines on the Xbee radio, immediately re-transmits the data back to the base station. The base station then tells the PC that the data was successfully received. The range test software keeps track of the number of successful and unsuccessful transmissions. By letting this software run continuously, it is possible to measure the number of successful Rx/Tx operations that can be completed with the energy stored in the supercapacitor.

The first step in the Rx/Tx test was to initiate the range test software. Once the software was initialized, the X-band source was turned on and the supercapacitor was allowed to charge to 3.3 V. When the capacitor obtained 3.3 volts, the switch connecting the positive capacitor leg, and the Vcc pin on the radio was set to the open position. Energy could now reach the radio, thus allowing it to receive and transmit data. The voltage across the capacitor was measured during this process, and the resulting discharge characteristics are shown in Figure 4-7. This plot shows the capacitor is initially charged to 3.3 V. Once the Xbee radio is allowed to drain current from the capacitor, the voltage quickly drops down to a little less than 2V. While the capacitor is discharging, the radio is able to successfully receive and transmit 256 Bytes of data using the asynchronous RS-232 protocol, over a distance of 5.2 m. The data received by the range test software is displayed in Figure 4-8.

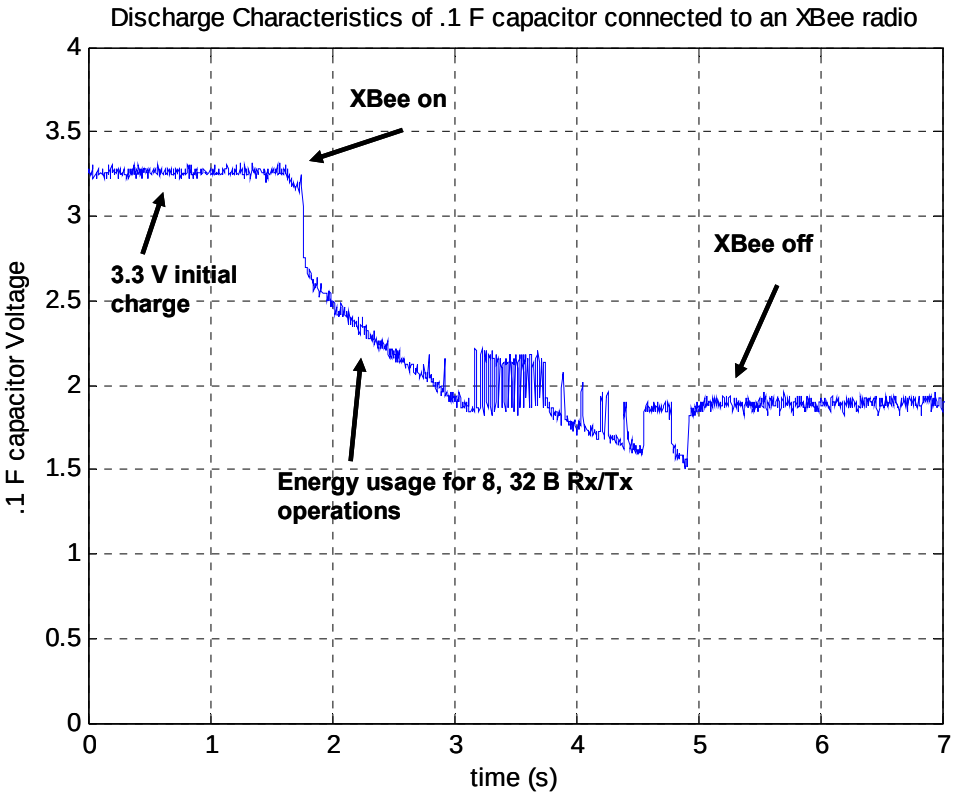

Figure 4-7: Discharge characteristics of the .1 F capacitor during the range test.

The results obtained from this test are very encouraging. The Xbee radio is by far the largest power consumer in the proposed sensor node, using between 45 to 50 mA for Rx/Tx operations at 3.3 V. The ATmega128L microcontroller actively running with an 8 MHz clock only uses 11 mA at 3.3 V, and the AD5933 typically uses 10 mA at 3.3 V. This experiment has shown that RF power delivery can be used to successfully operate the largest power consumer in the sensor node. Furthermore, the Xbee radio would generally have a very small duty cycle in comparison to the rest of the sensor node. A typical measurement would require transmitting only a couple of bytes of data in the case of the bolted joint preload sensor. Wireless power delivery

has promise as a suitable solution for providing power to long-term wireless sensor nodes.

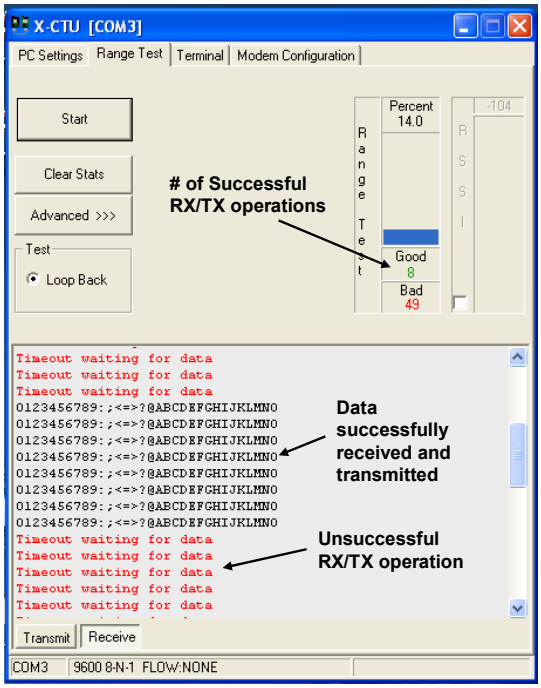

Figure 4-8: Range test software summary of Xbee radio performance

4.4 Summary of RF Wireless Power Delivery

The RF wireless power delivery system has been used to successfully power a .1 F supercapacitor to the 3.3 V needed for conventional CMOS logic circuits. The energy stored in the capacitor was sufficient to transmit 256 bytes of data from a 2.4 GHz Xbee radio over a distance of 5.2 m. Initial results using the RF wireless power delivery system show promise.

The power received by the capacitor, ~2.5 mW, was substantially lower than the 85 mW predicted by the one-way radar equation. The power discrepancy shows

there is much room for improvement in this system. Power losses can be mitigated by placing an impedance matching network before the rectification circuit, soldering the rectification circuit on Teflon circuit board, and attempting to find diodes with lower turn-on voltages. The performance of the RF power delivery system would be substantially improved by simply attaining 10 % of the calculated power received at the antenna.

Chapter 5 Conclusions and Future Work

5.1 Accomplishments

The main accomplishment of this thesis was the development of an impedance-based wireless sensor node for SHM applications. The sensor node is significantly lower in cost, size and power requirements than either a conventional 4294A or the recently developed (VT) impedance measurement solutions. In addition, a preliminary version of a generalized baseline sensor for bolted joint monitoring applications has been developed. The PZT enhanced nut displays very prominent and predictable changes in its resonant frequency as the preload on the bolt increases. In general, the magnitude of resonance is very pronounced at very low preload levels. As the preload is increased however, the peak quickly dies away. By employing algorithms capable of determining whether or not the resonant peak is present, it is possible to conclude whether or not the bolt has lost preload. Lastly, this thesis has proposed an alternative method for delivering power to a wireless sensor node by using RF wireless power delivery. RF delivered energy has been shown to be capable of supplying enough energy to power a 3.3 V, 2.4 GHz wireless telemetry system. When a .1 F supercapacitor was charged to 3.3 V using the RF wireless delivery system, it was possible to delivery 256 bytes of data using the wireless radio.

5.2 Contributions

This thesis has resulted in major contributions to the advancement of the impedance method as a SHM solution. The contributions of this thesis can be broken down into three main areas. The development of the PZT enhanced washer, the design and fabrication of a prototype impedance-based SHM sensor node, and the demonstration that RF wireless power delivery is a feasible solution to the low energy resource problem inherent in conventional wireless sensor nodes.

First, a generalized baseline sensor known as the PZT enhanced washer has been developed in order to ease data storage of baseline measurements in a sensor network array. Furthermore, the PZT enhanced washer possesses dynamics characteristics that exhibit a change with bolt preload level in a manner that is straightforward to quantify. A large amount of data storage is not necessary to quantify the changes in the dynamic characteristics of the PZT enhanced washer.

Secondly, a recently developed single chip solution for impedance measurements called the AD5933 has been integrated in a wireless sensor node for SHM applications. The impedance measurements obtained with the AD5933 are comparable with those obtained with an Agilent 4294A impedance analyzer and a NI PXI-1042Q data acquisition system.

Last of all, wireless RF power delivery has been explored as a possible alternative energy source for wireless sensor networks.

5.3 Future Work

5.3.1 PZT Enhanced Washer

A number of improvements can be made to the PZT enhanced washer in order to improve its appeal as a generalized baseline sensor. First off, the PZT enhanced washer is rather large at 19mm high by 25.4 mm in diameter. These dimensions are significantly larger than a conventional washer, and must be scaled down if the PZT enhanced washer is to have any future as a structural health monitoring sensor on weight critical aerospace structures. Secondly, the current incarnation of the PZT enhanced washer is only adequate for indicating whether or not a bolt has come loose. Future PZT enhanced washers need to be designed to include impedance measurement features that can quantitatively assess the bolt preload over a wider preload range.

In order to design the future PZT enhanced washers, more advanced analytical and numerical models will be needed to understand the dynamics of such washers in the tens of kHz frequency range.

The generalized baseline concept should also be extended to more far reaching SHM applications than the bolted joint problem. One of the important limitations of the impedance method in current practice is that even though the impedance measurements are sensitive to small changes in structural integrity, it is difficult to make sense of the measurements in order to make an estimation of what form the structural damage is or to what extent the structural damage occurred. In order to make the impedance method more suitable for general SHM applications, generalized features must be found in impedance measurements that change in a relatively

predictable manner as the structure is damaged. One example of such a feature might include characterizing the probability density function of the differences in a signal from a damaged system as opposed to an undamaged signal, or tracking changes in the resonant frequencies of a structure. Generalized baseline features must be sought out and exploited in order to expand the use of the impedance method to more generalized SHM problems.

5.3.2 Wireless Sensor node

The wireless sensing node outlined in this thesis is on the verge of being ready for field deployment trials. The clear first step is to get the sensing node off the development board and onto PCB. The initial goal is to be able to fit the entire sensor node on a PCB with area slightly less than that of a credit card. This goal should be relatively easy to accomplish given the sizes of all the components and the low number of pins, (~ 10) used on the microcontroller.

Another sensor node feature that might be applicable for some SHM applications is the addition of memory to the senor node. The 4096 bytes of SRAM currently available on the sensor node may not be sufficient for many SHM applications. Two memory storage options are currently being explored. The first is the addition of SRAM, and the second is the addition of a USB mass storage device. Either solution should be feasible, thus enhancing the spectrum of wireless sensor node capabilities.

The last addition to the wireless sensor node concerns the wireless telemetry. The radio on the node is by far the largest power consumer. Additional low-power wireless telemetry solutions should be pursued.

There is much room for improvement in the current wireless sensor node. Development in the near future should yield relatively high pay-off gains in active sensor node technology. Simply by creating a wireless sensor node on a PCB about the size of a credit card would result in the smallest active sensor node in the 10 - 100 kHz range for SHM applications that the author is aware of.

5.3.3 RF Wireless Power Delivery

There are a number of aspects in the wireless power delivery system that can be improved. First of all, a receiving antenna with a larger aperture should be employed in order to collect a larger percentage of the RF radiation. Secondly, an impedance matching network needs to be placed before the voltage rectification circuit in the rectenna. Third, the rectification circuit needs to be placed on low-loss Teflon board, which also has a more uniform dielectric constant.

Another area of microwave power delivery that is worth exploring is the use of high gain parabolic, and elliptical reflectors, as well as microwave lenses, in order to improve the distance over which microwave energy can be delivered.

The last aspect of the RF power delivery that should be investigated in the near term is the integration of conventional, passive RFID technology. By using a U3280

transponder-to-microcontroller interface chip, energy could be supplied to the microcontroller via inductive coupling at 125-135 kHz. Sending energy via inductive coupling would require loop antennas with lower weight and size than most forms of microwave rectennas. The tradeoff is that inductively coupled, passive RFID transponders are typically limited to distances on the order of a couple of meters. Passive RFID technology may have application in some sensor network applications and should be further explored.

5.4 Conclusions

This thesis has outlined the development of an impedance-based wireless sensor node for bolted joint preload applications. The sensor node made use of the recently developed PZT enhanced washer, as well as the new AD5933 impedance measurement chip. The PZT enhanced washer and the AD5933 were combined with a microcontroller and a 2.4 GHz radio in order to create a wireless sensor network. Wireless RF power delivery was also investigated as an alternative means to power the sensor node.

First, the PZT enhanced washer was demonstrated to be suitable as a generalized baseline sensor for the detection of the loss of preload in a bolted joint. The prototype of the wireless sensor node was successfully designed and implemented. The AD5933 proved to be a suitable replacement for conventional

impedance analyzers for SHM applications, and last of all, RF power delivery proved to be a viable energy delivery solution for wireless sensor nodes.

Future work on the PZT enhanced washer will be focused on building a washer with dynamic characteristics that change more smoothly as the preload in the bolt increases. By tuning the dynamics of the washer, it will be possible to build a washer that can not only give an indication of how much preload is experienced by the joint, but is also smaller in size. Advances in the sensor node itself will be concerned with getting the components onto a single PCB. In addition, sensor nodes will be developed with higher data storage capabilities. The energy delivered by the RF wireless power delivery system can be increased by placing an impedance matching network between the antenna and the rectifier circuit, using a larger aperture antenna, and placing the rectifier circuit on a Teflon board. There are many opportunities for improvement in the wireless sensor node that will be exploited.

Bibliography

1. Agilent, (2003), "Agilent 4294A Precision Impedance Analyzer," http://cp.literature.agilent.com/litweb/pdf/5968-3809E.pdf, January 2003.

2. Amirtharaja, R., Chandrakasan, A. P., (1998) " Self Powered Signal Processing Using Vibration Based Power Generation," IEEE journal of Solid State Circuits, Vol. 33, No. 5, May 1998.

3. Analog Devices, (2005), "AD5933 Data Sheet," http://www.analog.com/UploadedFiles/Data_Sheets/423236275AD5933_0.pdf

4. Analog Devices, (2005), "AD5934 Data Sheet," http://www.analog.com/UploadedFiles/Data_Sheets/85773579AD5934_0.pdf

5. APC International Ltd "Piezo Theory" www.americanpiezo.com/piezo_theory

6. Atmel Website, www.atmel.com

7. Atmel, (2005) "ATA5590 Summary, " Atmel Corporation, http://www.atmel.com/dyn/products/product_card.asp?PN=ATA5590

8. Atmel, (2004) "ATmega128L datasheet," http://www.atmel.com/dyn/resources/prod_documents/doc2467.pdf , Latest Revision, November, 2004.

9. Atmel, (2004), "RFID Application Kit TMEB8704," Atmel Corporation, March, 2001.

10. Atmel, (2004), "Transponder Interface for Microcontroller, U3280M," Atmel Corporation, December, 2004.

11. AVRfreaks Website, www.avrfreaks.net

12. Bois, C., Hochard, C., (2004) "Monitoring of Laminated Composites Delamination Based on Electro-mechanical Impedance Measurement", Journal of Intelligent Material Systems and Structures, Vol 15, 59-67

13. Bracht, R., Briles, S., Burris, A., Lewis, P., Kuckertz, T., Miller, E., (1993), "Modulated Reflectors and Their Applications," DOE Expo, Oak Ridge National Laboratory, May 3, 1993.

14. Bracht, R., and Kuckertz, T., (1994), "COVICS, a Covert Video Communications System," RF Expo West, San Jose, CA, March 22, 1994.

15. Brown, C., (2004), "Wireless Sensor Tracks Forces at Work in Human Joints," http://www.techweb.com/wire/26804212

16. Brown, W.C., (1984), "The History of Power Transmission by Radio Waves," IEEE Transactions on Microwave Theory and Techniques, Vol. MTT-32, No 9, September 1984.

17. Calhoun, B., Daly, D., Verma, N., Finchelstein, D., Wentzloff, D., Wang, A., Cho, S.H., Chandrakasan, A., (2005) "Design Considerations For Ultra Low Energy Wireless Microsensor Nodes," IEEE Transactions on Computers, Vol. 54, NO. 6, June 2005.

18. Campolo, D., Sitti, M., Fearing, R., (2003), "Efficient Charge Recovery Method for Driving Piezoelectric Actuators with Quasi-Square Waves," IEEE Transactions on Ultrasonics, Ferroelectrics, and frequency Control, Vol. 50, No. 1, January, 2003.

19. Capital Advanced Technologies, SurfBoard for surface mount prototyping, http://www.capitaladvanced.com/products.htm

20. Chaudhry, Z., Joseph, T., Sun, F., and Rogers, C.A., (1995), " Local-Area health monitoring of aircraft via Piezoelectric Actuator/Sensor Patches," SPIE Conference, San Diego, Ca, Proceedings of the SPIE, Vol 2443.

21. Cho, T., Cline, D., Conroy, C., Gray, P., (1994) "Design Considerations for High Speed Low-Power, Low-Voltage CMOS Analog to Digital Converters." IEEE Symposium on Low Power Electronics, San Diego, CA, 1994, pp 70-73.

22. Choi, S., Chu, S.H., Song, K., King, G., (2002) "Microwave-Driven Multifunctional Capability of Mambrane Structures," AIAA-2002-5751 "At the Edge of Revolution," Houston Texas, Sept 9-12, 2002.

23. Choi, S., Song, K., Golembiewskii, W., Chu, S.H., King, G., (2004), "Microwave Power for smart material actuators," Institute of Physics Publishing, Smart Materials and Structures, No 13, 38-48.

24. Choi, S., Golembiewski, W., Song, K., (2000), "Networked Rectenna Array for Smart Material Actuators," AIAA-2000-3066, Intersociety Energy Conversion Engineering Conference, 2000, CONF 35, Vol. 2, pp 1449-1457.

25. Chriswell, D., (2002), "Solar Power Via the Moon," American institute of Physics, April/May 2002, pp 12 – 15.

26. Cooper Industries, "PowerStor Aerogel Supercapacitors," http://www.cooperet.com/products/products.cfm?page=supercapacitors

27. Corbishley, P., Rodriguez-Villegas, E., Toumazou, C., (2004), "An Ultra-Low Power Analogue Directionality System for Digital Hearing Aids," IEEE International Symposium on Circuits and Systems, 2004.

28. Dancy, A., Amirtharajah, R., and Chandrakasan, (2000), "High Efficiency Multiple Output DC-DC conversion for Low Voltage Systems," IEEE Transactions on Very Large Scale Integration Systems, Vol. 8, No. 3, June 2000.

29. Dickenson, R., (~1999), "Bill Brown's Distinguished Career," January 27, 2006, http://www.mtt.org/awards/WCB's%20distinguished%20career.htm

30. Dove, J., Park, G., Farrar, C., (2006), "Hardware Design of hierarchal active sensing networks for structural health monitoring," Smart Materials and Structures, NO. 15, 139 - 146.

31. Energizer Battery, (2006), "Energizer 522, 9V Alkaline battery datasheet," http://data.energizer.com/PDFs/522.pdf

32. Energizer Battery, (2006), "Energizer E91, 1.5V, AA, Alkaline battery datasheet," http://data.energizer.com/PDFs/E91.pdf

33. Epp, L., Khan, A., Smith, H., Smith, R., (2000), "A Compact Dual Polarized 8.51 Ghz Rectenna for High-Voltage (50 V) Actuator Applications," IEEE Transactions on Microwave Theory and Techniques, VOL. 48, NO. 1, January 2000.

34. Finkenzeller, K., (2003) "RFID Handbook, Fundamentals and Applications in Contactless Smart Cards and Identificaiton - 2nd Edition," John Wiley and Sons LTD. 2003.

35. Forever Flashlight, http://www.foreverflashlights.com/

36. Fork, R., (2001), "High Energy Lasers May Put Power in Space," Laser Focus World, VOL. 37, NO. 9, September 2001, pp 113 - 117.

37. Gaul, L., (1997), "Active Control of Joints in members and structures," German Patent DE19702518A1

38. Goldfarb, M. and Jone, L.D., (1999) "On the Efficiency of Electric Power Generation with Piezoelectric Ceramic," ASME Journal of Dynamic Systems, Measurement and Control, Vol 121, 566-571.

39. Gonzalez,J.,Rubio, A., Moll, F., (2001), "A Prospect on the Use of Piezoelectric Effect to Supply Power to Wearable Electronic Devices," ICMR 2001, Akita Japan, October, 2001, Vol 1, pp 202-207.

40. Gordon, D., (2004), "Wireless Retrieval of a Mouse's Vital Signs via RFID," http://instruct1.cit.cornell.edu/courses/eceprojectsland/STUDENTPROJ/2004to2005/dig4/dig4rfid.htm

41. Grisso, B., (2004) "Considerations of the Impedance Method, Wave Propogation, and wireless systems for Structural Health Monitoring," Master's Thesis, Virginia Polytechnic Institute and State University.

42. Hagerty, J., Helmbrect, F., McCalpin, W., Zane, R.,and Popovic, Z., (2004), "Recycling Ambiant Microwave Energy With Broad-Band Rectenna Arrays," IEEE Transactions on Microwave Theory and Techniques, VOL. 52, NO. 3, March 2004.

43. Harris, C., and Crede, C., (1976), "Shock and Vibration Handbook," McGraw Hill Book Company

44. Heikkinen, J., Kivikoski, M., (2001), "Performance and Efficiency of Planar Rectennas for Short- Range wireless power transfer at 2.45 GHz," Microwave and Optical Technology Letters, Vol. 31., No. 2, October 20, 2001.

45. Juzkow, M., (2001), "Aerogel Capacitors: A Unique Low-ESR Supercapacitor," Wireless Portable Symposium and Exhibition, spring 2001.

46. Kansal, A., Srivastava, M., (2003), "An Environmental Energy Harvesting Framework for Sensor Networks," ISLPED 2003, August 25-27, 2003, South Korea.

47. Kaufman, H.R., Cuomo, J.J., Harper, J.M.E., (1982), "Technology and applications of broad-beam ion sources used in sputtering. Part I. Ion Source Technology," Journal of Vacuum Science and Technology , September 1982, Vol. 21, Issue 3, pp 725 – 736.

48. Keane, G., Woods, R.F., Power, K., (1996), "VLSI Achitectures for High Performance Low Power Signal Processing Applications," Irish Digital Signal Processing and Control Conference, pp 269-276, 1996.

49. Kim J., Horowitz, Mar., (2002), "Adaptive Supply Serial Links with Sub-1-V Operation and Per-Pin Clock Recovery," IEEE Journal of Solid State Circuits, Vol. 37, No. 11, November 2002.

50. Lalande, F., Childs, B., Chaudhry, Z., and Rogers, C.A., (1996), "High Frequency Impedance Analysis for NDE of complex Precision Parts." In Conference of Smart Structures and Materials, February 26-29, San Diego, CA, SPIE publishing, Bellingham, WA, Proceedings of the SPIE, Vol. 2717, 237-245

51. Lee, Thomas, (2004), "Planar Microwave Engineering: A Practical Guide to theory, Measurements, and Circuits." Cambridge University Press, August 2004

52. Liang, C., Sun, F.P., and Rogers, C.A., (1994), "Coupled Electromechanical Analysis of Adaptive Material Systems – Determination of the actuator Power Consumption and System energy Transfer," Journal of Intelligent Materials and Structures., Vol 5, 12-20.

53. Liu, L., and Yuan, G., (2005), "Design of Wireless Sensor for High Frequency Applications," Proceedings of the 5th international Workshop on Structural Health Monitoring, September 12 – 14, 2005, pp 1602 – 1609.

54. Lynch, J., Sundararajan, A., Law, K., Sohn, H., and Farrar, C., (2004), "Design of a Wireless Active Sensing Unit for Structural Health Monitoring," SPIE 11th Annual International Symposium on Smart Structures and Materials, San Deigo, Ca, March 14 – 18, 2004.

55. Mascarenas, D., Park., G., Farrar, C., (2005), "Monitoring of Bolted Joint Preload Using Piezoelectric Active Devices," Proceedings of SPIE, VOL. 5768, pp 129 – 136.

56. MaxStream, www.maxstream.net

57. Meindl, J., (1997) "A History of Low Power Electronics: How it Began and Where it is Headed," International Symposium on Low Power Electronics and Design, August, 1997, 149-151.

58. Menendez, C., "Other Causes of Fastener Failure," Fastener Technology International 2003

59. Meninger, S., Mur-Mirand, J.O., Amirtharajah, R., Chandrakasan, A., and Lang, J., (2001) "Vibration-to-Electric Energy Conversion," IEEE Transactions On Very Large Scale Integration Systems, Vol. 9, No. 1, February 2001.

60. Min, R., Bhardwaj, S.H.C., Sinha, A., Shih, E., Wang, A., Chandakasan, A, (2000) "An Architecture for a Power-Aware distributed Microsensor Node," IEEE Workshop on Signal Processing Systems, Oct, 2000, pp 581-590.

61. Naval Air Systems Command, (1999) "Electronic Warfare and Radar Systems Engineering Handbook," Avionics Department, AIR-4.5, EW Class Desk, Washington, D.C, 20361

62. Nichols, J., Nichols, C. Todd, M., Seaver, M., Trickey, S., (2004), "Use of data driven phase space models in assessing the strength of a bolted joint connection in a composite beam," Smart Materials and Structures, 12, pp 241-250.

63. Nichols, J., Todd, M., Wait, J., (2003), "Using state space predictive modeling with chaotic interrogation in detecting joint preload loss in a frame structure," Smart Materials and Structures, 12., pp 580-601.

64. Okugawa, M., (2004), "Bolt Loosening Detection Methods by using Smart Washer Adopted 4SID," Proceedings of 45th AIAA/ASME/ASCE/AHS/ASC Structures, Structural Dynamics & Materials Conference 19-22 April 2004, Palm Spring, CA, AIAA2004-1981

65. Paradiso, J., Starner, T., (2005), "Energy Scavenging for Mobile and Wireless Electronics," Pervasive Computing, January-March, 2005.

66. Park, G., Cudney, H., Inman, D.J., (2001), "Feasibility of Using Impedance-based Damage Assessment for Pipeline Systems," Earthquake Engineering & Structural Dynamics Journal, 30, pp. 1463-1474.

67. Park, G., Farrar, C., Rutherford, A., Robertson, A., (2006) "Piezoelectric Active Sensor Self-Diagnostics using Electrical Admittance Measurements," Submitted to the ASME Journal of Vibrations and Acoustics.

68. Park, G., Muntges, D.E., Inman D.J., (2003), "Self-Repairing Joints Employing Shape Memory Alloy Actuators," Journal of Minerals, Metals & Materials Society, 55, pp. 33-37

69. Park, G., Sohn H., Farrar C., Inman D.J. (2003), "Overview of Piezoelectric Impedance-Based Health Monitoring and Path Forward," Shock and Vibration Digest, 35, 451-463.

70. Peairs, D., Park, G., Inman, D., (2004) " Improving Accessibility of the Impedance-based Structural Health Monitoring Method " Journal of Intelligent Materials Systems and Structures, Vol. 15, 129-139.

71. PhysikInstrumente, "Fundamentals of Piezoelectricity, PZT Ceramics Manufacturing," http://www.physikinstrumente.com/en/products/prdetail.php?VID=&sortnr=400600.05

72. Pohl, J., Herlod, S., Mook, G., and Michel. F., (2001), "Damage Detection in Smart CFRP Composites using Impedance Spectroscopy," Smart Materials and Structures.

73. Pozar, D., (2005), " Microwave Engineering, 3rd edition," John Wiley and Sons, Inc

74. Rahimi, M., Shah, H., Sukhatme, G., Heideman, J., and Estrin, D., (2003), "Studying the Feasibility of Energy Harvesting in a Mobile Sensor Network," IEEE International Conference on robotics and Automation, 2003, VOL. 1, pp 19 – 24.

75. Raju, V., (1998), "Implementing Impedance-Based health monitoring Technique," Master's Thesis, Virginia Polytechnic Institute and State University, Blacksburg, VA.

76. Ritdumrongkul, S., Masato, S., Fujino, Y., Miyashita, T., "Quantitative health monitoring of bolted joints using a piezoceramic actuator-sensor," Smart Materials and Structures, Vol. 13, 2004, pp 20 - 29.

77. Roundy, S., Wright, P., Rabaey, J., (2003), "A study of low level vibrations as a power source for wireless sensor nodes," Computer Communications, No 26 (2003), 1131-1144.

78. Schactman, N., (2003), "What's Next, Soaring into the Air with a Boost from a Laser Beam," New York Times Technology Review, November 6, 2003.

79. Seemann, K., Weigel, R., (2005), "Ultra-Low-Power Rectification in Passive RFID Tags at UHF Frequencies," Institute of Electronics Engineering, University of Erlangen-Nuremberg, seemann@lfte.de.

80. Sharpe, C., (1994), "Data Communication by Means of Reflective Transmission," RF Expo West, San Jose, CA, March 22-24, 1994.

81. Shull, P., (2002), "Nondestructive Evaluation, Theory, Techniques and Applications," Marcel Dekker INC.

82. Simmons, W.C. (1986), "Bolt failure studies at Aberdeen Proving Ground, problems and solutions." Proc., Int Conf on Cracks and Fatigue, Fracture Mech and Failure Anal., Salt Lake City, Utah.

83. Sodano, H., Inman, J., Park, G., (2004), " A Review of Power Harvesting from Vibrations using Piezoelectric Materials" The Shock and Vibration Digest, Vol 36., No 3, May 2004 197-205.

84. Sodano, H.A., Magliula, E.A., Park, G., and Inman, D.J., (2002), "Electric Power Generation from Piezoelectric Materials," in Proceedings of the 13th International Conference on Adaptive Structures and Technologies, October 7-9, Potsdam/Berlin, Germany

85. Song, K., Yi, W., Chu, S, H., (2003), "Microwave-Driven THUNDER materials," Microwave and Optical Technology Letters, Vol. 36, No. 5, March 5, 2003.

86. Stokes, J.P. and Cloud, G.L.,1993, "The Application of Interferometric Techniques to the Nondestructive Inspection of Fiber-Reinforced Materials," Experimental Mechanics, Vol 33, 314-319

87. Sun, F., Chaudhry, Z., Liang, C., and Rogers, C.A. (1995), "Truss Structure Integrity Identification Using PZT Sensor-Actuator," *Journal of Intelligent Material Systems and Structure,* 6, pp. 134-139

88. Sun, F., Roger, C.A., and Liag, C., (1995), "Structural Frequency Response Function Acquisition via Electric Impedance Measurements of Surface Bonded PiezoElectric Sensor/Actuator," Proceedings of the 36th AIAA/ASME/ASCE/AHS/ASC Structures, Structural Dynamics, and Materials Conference, 3450-3461.

89. Todd, M., (2005), "Different Approaches Towards Deploying SHM Sensor Arrays: Wireless Communications with Autonomous Vehicle Interrogation," Proceedings of the 5th International Workshop on Structural Health Monitoring, September 12 – 14, 2005, pp 1594 – 1601.

90. Townsend, C., Arms, S., Hamel, M., (1999) "Remotely Powered, multichannel, microprocessor based telemetry systems for a smart implantable total knee implant." www.microstrain.com

91. Umeda, M., Nakamura, K., and Ueha, S., (1997), "Energy Stroage Characteristics of a Piezo-Generator using Impact Induced Vibration," Japanese Journal of applied Physics, Vol 36, Part 1, No 5B, 3146-3151

92. Van Dijk, L. P. L., Van Der Woerd, A.C., Mulder, J., and Van Roermund, A.H.M., (1998) "An Ultra-Low Power, Low-Voltage Electronic Audio Delay Line for Use in Hearing Aids," IEEE Journal of Solid State Circuits, Vol 33, NO. 2, February, 1998.

93. Voltage Multipliers Inc., "Multiplier Design Guide" http://www.voltagemultipliers.com/html/multdesign.html

94. Walker, J., Montgomery IV, E., (1994), "Laser Power Beaming," Procedings of SPIE, VOL. 2121.

95. Wang, X., Ehlers, C., Kissinger, C., Neitzel, M., Ye, L., M, Y., "Experimental investigation of piezoelectric wafers in monitoring the resin transfer moulding process," Smart Materials and Structures, No 7, 121-127.

96. Wei, G.Y., (2001), "Energy Efficient I/O Interface Design with Adaptive Power-Supply Regulation," PhD Thesis, Stanford University, June, 2001.

97. Wei, G.Y., Horowitz, M., (1999), "A Fully Digital Energy-Efficient Adaptive Power-Supply Regulator," IEEE Journal of Solid State Circuits, Vol. 34, No. 4., April 1999.

98. Wikipedia, "Piezoelectricity" http://en.wikipedia.org/wiki/Piezoelectric_effect

99. Williams, C. B., Shearwood, C., Harradine, M. A., Mellor, P. H., Birch, T.S., Yates, R. B., (2001), "Development of an electromagnetic micro-generator" IEEE Proceedings on Circuits, Devices, Systems, Vol. 148, No. 6, December 2001.

100. Xu, Y.G., and Liu, G.R., (2002), "A modified Electromechanical Impedance Model of Piezoelectric Actuator-Sensors for Debonding Detection of Composite Repair Patches," Journal of Intelligent Materials Systems and Structures, Vol. 13, No. 6, 389-405.

101. Yang, J., Change, F.K., Derriso, M.M., (2003), "Design of Hierarchical Health Monitoring System for Detection of Multilevel Damage in Bolted Thermal Protection Panels: A Preliminary Study," International Journal of Structural Health Monitoring, 2, pp. 115-122.

102. Young, R., Williams, M.D., Walker, G.H., Schuster, G.L., and Lee, J.H., (1991), "A Lunar Rover Powered by an Orbiting Laser Diode Array," Space Power, VOL. 10, pp. 103 – 127.

103. Yugami, H., Kanamori, Y., Arachi, H., (1997), "Field Experiment of Laser Energy Transmission and Laser to Electric Conversion," Intersociety Energy Conversion Engineering, Conf 32, VOL. 1, pp 625 – 630.